POLITECNICO DI TORINO

Master Degree Course in Biomedical Engineering

Department of Mechanical and Aerospatial Engineering

MASTER DEGREE THESIS

Volumetric blood flow imaging with ultrafast ultrasound: a new approach based on the speckle decorrelation method

Supervisors:
Prof. Filippo MOLINARI
Prof. Mengxing TANG

Assistant supervisor:
Dr. Xiaowei ZHOU

Candidate:
Raffaele SANTARPIA
Matr. 252398

ACADEMIC YEAR 2019-2020

"Il mondo invisibile non è costituito solo da ciò che non si lascia vedere, ma anche da ciò che non è messo in rilievo nel dominio del visibile. Quando la cosa nascosta dalla luce della coscenza acquisisce forma e si arrende all'evidenza, la reazione è quella dello stupore."

Salomon Resnik

Ai miei genitori

Abstract

The estimation of 3-D blood flow through vessels represents one of the most challenging aspects both in clinics and in research. Through the measurement of the volume flow it is possible to prevent many cardiovascular diseases, which are among the main causes of deaths all over the world. Currently, because of the limitations existing in the modern ultrasound systems, there is no efficient solution to estimate the volume flow. In recent years an interesting approach, capable to evaluate the volumetric blood flow from the cross-sectional imaging plane was conceived. This approach is based on detecting the out-of-plane velocity component by using the speckle decorrelation (SDC) and the in-plane velocity components by using the ultrasound imaging velocimetry (UIV). By making use of micro-bubbles contrast agents and a standard 1-D array transducer working at high frame-rate, the recent research has found compelling results. Despite the good results, the new technique performs well only in presence of micro-bubbles contrast agents, which are necessary to enhance the blood flow signal. Therefore, this master thesis project aims to test the goodness of the speckle decorrelation method in absence of micro-bubbles. Since blood is anechoic, meaning that it produces weak echoes when hit by ultrasound, it is necessary to find a way to increase its signal. Singular value decomposition (SVD) filtering has been performed to achieve this result. The proposed method has been evaluated on wall-less flow phantom, with the help of a pulsatile pump, which emulates the heartbeat. The phantom size is close to the one of big human vessels. In vitro experiments have been conducted with the use of the blood mimicking fluid (BMF), which is able to mimic the characteristics of human blood. The influence of different combinations of voltage and pulse length on the estimation of the velocity has been studied, as well. The conducted experiments show interesting results. In particular, it has been proved that at a flow rate of 80 mL/min and with low values of pulse length, i.e. PL=1 and PL=2, the estimated volume flow matches well with the ground-truth, providing an averaged error of $3.90\% \pm 2.43\%$. On the other side, the results obtained with high value of pulse length, i.e. PL=4 and PL=6, provided an averaged error of $16.01\% \pm 7.91\%$. The in vitro trials suggest that the technique studied in this master thesis project could give an important contribution in the next future clinical applications.

Index

Abstract iii

Conspectus descriptionum vii

Conspectus tabularum xi

1 Introduction 1
- 1.1 Clinical Relevance . . . 1
- 1.2 Long Term Goal . . . 4
- 1.3 Contribution of This Dissertation . . . 5

2 Background 7
- 2.1 Ultrasonic Imaging . . . 7
  - 2.1.1 Ultrasound Waves . . . 7
  - 2.1.2 Ultrasound Propagation . . . 8
  - 2.1.3 Transducers . . . 11
  - 2.1.4 Image Quality . . . 13
- 2.2 Flow Physics . . . 14
  - 2.2.1 Human Circularity System . . . 14
  - 2.2.2 Blood Pressure and Flow . . . 16
  - 2.2.3 Flow Phantom . . . 16
  - 2.2.4 Pathological Conditions . . . 19
- 2.3 Medical Ultrasound Systems . . . 20
  - 2.3.1 Grey Scale Ultrasound Systems . . . 20
  - 2.3.2 Continuous Wave Systems . . . 21
  - 2.3.3 Pulse Wave Systems . . . 22
  - 2.3.4 Color Doppler . . . 24

3 Blood Flow Velocity Estimation 27
- 3.1 Clutter Filtering - Singular Value Decomposition . . . 27
  - 3.1.1 Principle Aspects . . . 27
  - 3.1.2 Mathematica Aspects . . . 28
  - 3.1.3 Critical Aspects . . . 31
- 3.2 Velocity Estimator . . . 33
  - 3.2.1 Speckle Decorrelation Method . . . 33
  - 3.2.2 Calibration . . . 35
  - 3.2.3 Velocity Limitations . . . 41
- 3.3 Velocity Estimator in Presence of Reverse Flow . . . 41

3.3.1 Materials and Methods 41

4 Analysis of the Performances **43**
4.1 SVD - Thresholds Dependence 43
4.2 Voltage Dependence 45
4.3 Pulse Length Dependence 46
4.4 Results 49
4.4.1 Singular Value Decomposition Filtering 49
4.4.2 Speckle Decorrelation Method 62
4.4.3 Statistics 75

5 Conclusions and Future Prospects **79**

Conspectus librorum **81**

Conspectus descriptionum

1.1 Bar diagram representing the global number of died people in relation to the main causes of death. 1
1.2 The difference between Ischemic Stroke a) and Hemorragic Stroke b) is represented. 2
1.3 Typical portrayal of Unstable Angina, STEMI and NSTEMI attack. It allows to clearly see the differences between the structure of a vessel in presence of these three Acute Coronary Syndromes 3
1.4 Depiction of how to apply a ultrasound transducer on the neck of a patient to achieve the B-mode image of the carotid. 4

2.1 Reprinted from [22]. Particles displacement for a propagating ultrasound wave 8
2.2 Reprinted from [24]. Comparison between two types of reflection. On the left side of the figure, specular reflection is shown; on the right side diffuse reflection occurs. 9
2.3 The ultrasound wave hits the interface of the different media, generating a refracted wave. The speed of the incident and refracted are different, with respect to the properties of the two media. 10
2.4 Reprinted from [24]. Representation of diffuse scattering. 10
2.5 Reprinted from [24]. Different values of attenuation coefficients in relation to body tissues. 11
2.6 Verasonics probe L11-4v. On the right the spectrum and waveform are shown 11
2.7 Reprinted from [27]. "A conceptual diagram of phased array beam-forming. (Top) Appropriately delayed pulses are transmitted from an array of piezoelectric elements to achieve steering and focusing at the point of interest. (For simplicity, only focusing delays are shown here.) (Bottom) The echoes returning are likewise delayed before they are summed together to form a strong echo signal from the region of interest". 12
2.8 "The procedure of envelope detection. RF signals are demodulated by two local oscillators with transmitting frequency f_0. Demodulated signals are filtered by low-pass filters to generate I (in phase) and Q (quadrature) signals. The envelope of the complex IQ signal is then detected." 12
2.9 Representation of the anatomy of a normal heart. 15
2.10 Representation of the anatomy of a normal heart. 15
2.11 Pulsatile blood pump by Harvard Apparatus. 17
2.12 Blood mimicking fluid. 19
2.13 Representation of a carotid artery stenosis. 20

2.14 Representation of an A-mode image. 21
2.15 Representation of the B-mode image of a normal carotid artery. 21
2.16 A continuous-wave Doppler transducer contains two separate elements to transmit and receive ultrasound waves. 22
2.17 Reprinted from [16]. "RF sampling of single pulse moving away from the transducer. The left graph shows the different received RF lines, and the right graph is the sampled signal. The dotted line indicates the time when samples are acquire". 23
2.18 "A screen shot of spectral Doppler showing both B-mode image and spectrogram of the carotid artery. The Doppler signal is collected from the gate along the beam direction". 24
2.19 "A diagram of color Doppler. Samples at specific locations in successive B-mode images are collected to form the Doppler signal $x_{ij}(t)$, where i and j represents the location of the samples and t represents the sampling time." 25
2.20 "A screen shot of color flow image of carotid artery bifurcation. The velocity information is superimposed on the B-mode image. The color represents the direction of the blood flow." 26

3.1 "Typical example of an Ultrafast Acquisition. The top image depicts $s(x, z, t) = 0$ of an Ultrafast acquisition acquired during 0.5 s at a Frame Rate of 500 Hz, on the brain of a thinned skull rat (scale bar = 1 mm). To have an insight into the temporal dimension of this Ultrafast acquisition, two neighbourhoods of nine pixels have been chosen in the image (green and cyan squares). Inside each pixel, the simplified signal $\bar{s}(x, z, t)$ is calculated to get rid of phase difference and amplitude difference from one pixel to another. $\bar{s}$ is then plotted with color respective to the position in the nine pixel neighbourhood (black, blue or red). This illustrates that signal in close pixels is very similar in shape." 29
3.2 "The same data than in the green nine pixel neighborhood of figure 3.1 are filtered using a 50 Hz cut off 4^{th} order Butterworth filter typically used to discriminate between tissue and blood flow signals, and on the graphs it can be observed that the low frequency (LF) part of the nine pixel temporal signal are really similar in shape and seem highly correlated, whereas the blood signal (HF)seem highly decorrelated. On the right are displayed the 9×9 covariance matrix (magnitude) of the normalized zero-mean complex signals, for the low frequency and high frequency part respectively. HF Blood signal is indeed highly decorrelated compared to LF tissue signal." . 30
3.3 "Singular values of the matrix Δ (solid blue) expressed in dB and cumulative sum of those singular values from n° 50 (dashed red)." 32
3.4 "Spatial criteria for threshold selection. (a) Incoherent correlation matrix of spatial singular vectors, for a plane wave ultrafast Doppler acquisition on a flux phantom. Three highly correlated areas appear. (b) Spatial vectors are incoherently averaged in the 3 areas, giving intensity maps. From 1 to 20 (red dotted squares), vectors describe the tissue and the canal walls. From 20 to 78 (purple dotted squares), spatial vectors represent the blood flow. From 78 to 150, spatial vectors account for mostly noise, yet with remaining blood signal." 33

3.5 "Intensity values between a series of patches (marked with white boxes) from B-mode frames in the elevational direction (frame 1 to frame n) decorrelate and the decorrelation rate follows a Gaussian curve." 34
3.6 The transducer L11-4v is place on a speckle phantom for calibrating the probe. Beneath the phantom an absorber is deposited, in order to avoid the reflection from the bottom of the case. 36
3.7 The transducer is moving along the elevational direction over a speckle phantom. 37
3.8 V=5V PL=1 calibration. 38
3.9 V=5V PL=2 calibration. 38
3.10 V=5V PL=4 calibration. 38
3.11 V=5V PL=6 calibration. 38
3.12 V=10V PL=1 calibration. 39
3.13 V=10V PL=2 calibration. 39
3.14 V=10V PL=4 calibration. 39
3.15 V=10V PL=6 calibration. 39
3.16 V=15V PL=1 calibration. 40
3.17 V=15V PL=2 calibration. 40
3.18 V=15V PL=4 calibration. 40
3.19 V=15V PL=6 calibration. 40
3.20 Illustration of the ultrasound scanning strategy in the Speckle Decorrelation Method with the presence of reverse flow. 42

4.1 Correlation coefficient matrix of the first test performed with V=5V and PL=1. 44
4.2 Plot of the singular values λ of the first test performed with V=5V and PL=1. 44
4.3 The difference between SVD filtering with three different couples of thresholds. 45
4.4 The difference between SVD filtering with three different values of voltage. 46
4.5 Real pulse transmitted by Verasonics probe L11-4v. 47
4.6 The difference between SVD filtering with four different values of pulse length. 48
4.7 SVD filtering results for V=5V and PL=1. 50
4.8 SVD filtering results for V=5V and PL=2. 51
4.9 SVD filtering results for V=5V and PL=4. 52
4.10 SVD filtering results for V=5V and PL=6. 53
4.11 SVD filtering results for V=10V and PL=1. 54
4.12 SVD filtering results for V=10V and PL=2. 55
4.13 SVD filtering results for V=10V and PL=4. 56
4.14 SVD filtering results for V=10V and PL=6. 57
4.15 SVD filtering results for V=15V and PL=1. 58
4.16 SVD filtering results for V=15V and PL=12. 59
4.17 SVD filtering results for V=15V and PL=4. 60
4.18 SVD filtering results for V=15V and PL=6. 61
4.19 SDC results for V=5V and PL=1. 63
4.20 SDC results for V=5V and PL=2. 64

4.21 SDC results for V=5V and PL=4. 65
4.22 SDC results for V=5V and PL=6. 66
4.23 SDC results for V=10V and PL=1. 67
4.24 SDC results for V=10V and PL=2. 68
4.25 SDC results for V=10V and PL=4. 69
4.26 SDC results for V=10V and PL=6. 70
4.27 SDC results for V=15V and PL=1. 71
4.28 SDC results for V=15V and PL=12. 72
4.29 SDC results for V=15V and PL=4. 73
4.30 SDC results for V=15V and PL=6. 74
4.31 Mean and std of the estimated velocities with respect to the ground-truth. 77
4.32 Mean and std of the errors committed in the estimation of the out-of-plane velocities. 77

Conspectus tabularum

2.1 Range of arterial blood pressure for healthy people [32]. 16
2.2 Differences between Blood Mimicking Fluid and Blood characteristics [35]. 17
2.3 Receipt for making Blood Mimicking Fluid [36]. 18

4.1 Estimated out-of-plane velocities components and errors for each couple of parameters and each trials. 75
4.2 Means and standard deviations of the out-of-plane velocities components and errors. 76

Caput 1

Introduction

In this introductory chapter some aspects related to the ultrasound method will be presented. It will start with an overview on the clinical implications and benefits of adopting ultrasounds as prevention. Therefore, a general description of the aim of this project and the structure of the thesis will be given.

1.1 Clinical Relevance

Volumetric flow rate is one of the main factors indicating whether a specific organ or tissue gets the right amount of oxygen and nutrients for its metabolism. The decrease of the blood volume trough the vessels may be caused by some cardiovascular diseases. They lead to severe pathologies, such as arrhythmia, heart attack and stroke. According to the Global Heart Observatory (GHO), heart attack and stroke are the main causes of death in the World, leading to 15.2 million deaths in 2016, as shown in figure 1.1.

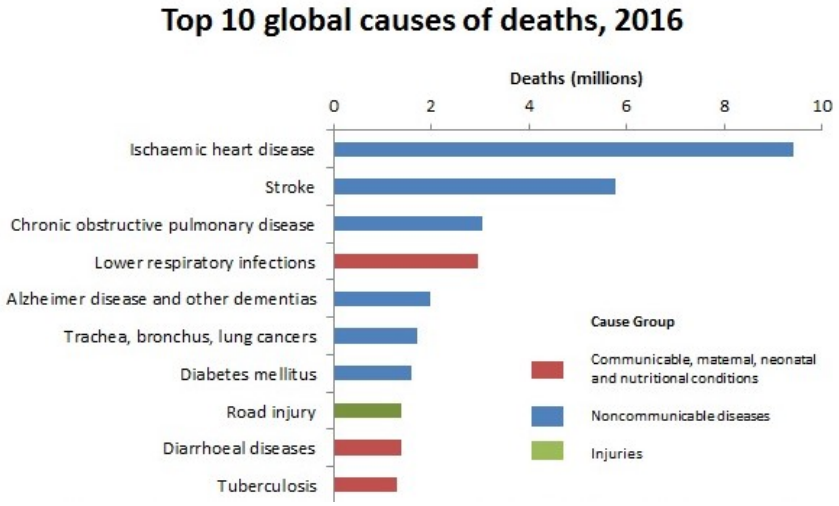

Descriptio 1.1: Bar diagram representing the global number of died people in relation to the main causes of death.

These pathologies remained the primary killers in the last 15 years. Strokes can be classified into two classes: Ischemic Stroke and Haemorrhagic Stroke. The first one happens

when the blood flow to the brain is discouraged by a lump in the vessel (figure 1.2a), while the second one occurs when there is a damage of a blood vessel in the brain (figure 1.2b). Heart attacks can be classified into three classes: STEMI, NSTEMI and Coronary spasm. ST segment elevation myocardial infarction (STEMI) occurs when the coronary artery is completely obstructed, which prevents blood from going to the heart. Non-ST segment elevation myocardial infarction (NSTEMI) occurs when the coronary artery is partially obstructed; in this case the blood flow is gravely limited and can cause a permanent injury. Corona artery spam is also known as silent heart attack or unstable angina and occurs when there is a contraction of the vessel linked to the heart.

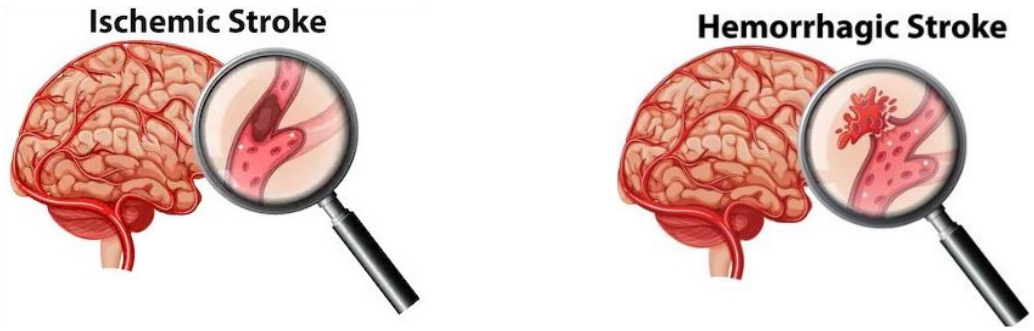

(a) (b)

Descriptio 1.2: The difference between Ischemic Stroke a) and Hemorragic Stroke b) is represented.

The differences between these three types of heart attack are shown in figure 1.3. After stroke, the brain does not receive the right amount of nutrients and oxygen and its tissue starts to die. This could lead to some impairments, such as memory loss, visual problems and paralysis. To avoid these impairments, the aim of medical treatments is to dissolve the clot in the vessel, for the ischemic stroke, and to reduce blood pressure, for the haemorrhagic stroke. Nevertheless, stroke may induce permanent damage to brain tissue, which is very hard to rehabilitate [1].

After heart attack, the area of the heart that does not receive the right amount of blood flow begins to die. This could lead both to immediate consequences, such as cardiogenic shock, hypoxaemia, DVT and myocardial rupture, and to delayed complications, such as aneurysm, oedema and congestive heart failure [2]. Medical treatments after a heart attack are based on assuming medicines for all life, such as aspirin, beta blockers and angiotensin converting enzyme inhibitors (ACE), or based on surgery, such as angioplasty and coronary artery bypass graft (CABG). According to the Stroke Alliance for Europe (SAFE), in 2017 the estimated medical cost of stroke treatments was over €60 billion [3], while according to the Centre of Economic and Business Research (CEBR) the estimated cost of heart attack treatments was up to €102.1 billion in 2014 [4]. Thus, the best way to lower both the amount of deaths and the cost of cardiovascular diseases treatments will be to adopt efficient prevention [1]. It is recognized that the distribution of the blood velocity in a vessel can be used to get diagnostic information [5]. An abnormal blood flow velocity could be index of a cardiovascular problem. Currently, magnetic resonance imaging is the best way to detect cardiovascular anomalies [6], but it has limited temporal resolution and poor accessibility. A better way to estimate blood flow rate, therefore to detect the health of cardiovascular system, is ultrasound imaging. Because of its affordability, high

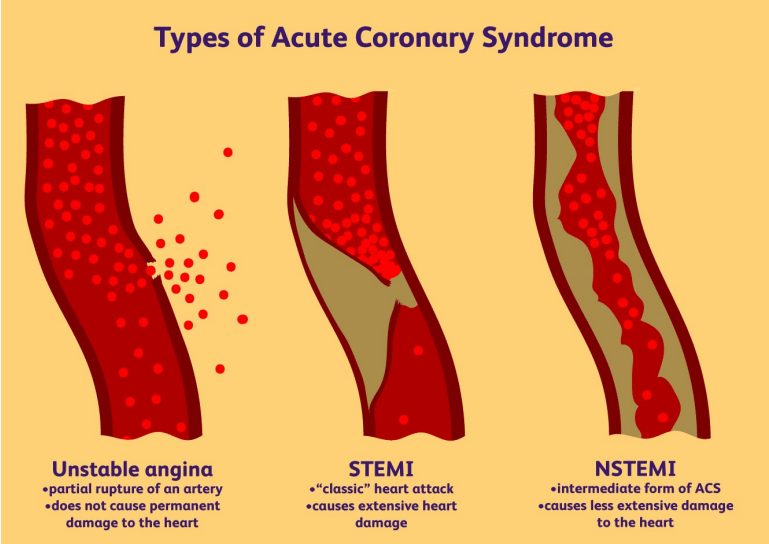

Descriptio 1.3: Typical portrayal of Unstable Angina, STEMI and NSTEMI attack. It allows to clearly see the differences between the structure of a vessel in presence of these three Acute Coronary Syndromes

temporal resolution, real time imaging and good spatial resolution, ultrasound imaging is the most common mean used in clinical applications for detecting blood flow. In addition, it is the only non-invasive diagnostic technique.

As shown in figure 1.4, to reveal the vessel, in this case carotid, the use of an ultrasound probe is necessary. The operating principle of the transducer is based on piezoelectric elements, that first send out ultrasound waves into human tissues and then get the reflected ultrasound waves. These reflected waves are produced by interference, both constructive and de-constructive, of scattered reflections from tissues. Different tissues correspond to different echogenicity, i.e. the ability to return the signal in ultrasound examinations. For example, blood is anechoic, that means it has low echogenicity; for this reason, in ultrasound images blood looks like a dark area. On the other hand, human tissues are echoic, thus they are seen as brighter areas. Due to this effect, it is possible to see the anatomy structure of human tissues.

In clinical practice the "Doppler effect" is fully applied to estimate blood flow. It is based on the scattering of blood cells that provide information on the velocity of blood flow. Despite this approach is angle dependent and prone to errors from many sources, it gives a good and easy way to measure the volume flow by measuring the mean velocity of blood and integrating it within the luminal area of the vessel [7], [8]. Furthermore, this conventional method is only able to measure the flow within one slice of the vessel from the longitudinal view, meaning that the flow profile is assumed to be symmetric along the vessel radius to detect the volume flow. Speckle decorrelation represents a new method which images the vessel from the cross-sectional view and solve the problems of Doppler.

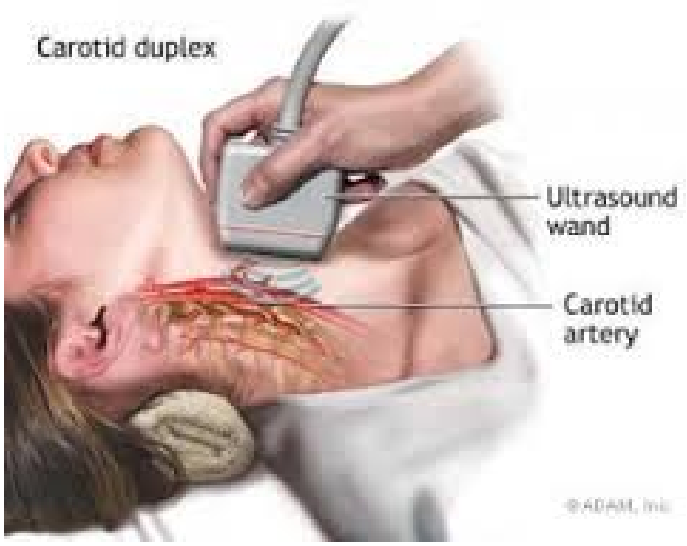

Descriptio 1.4: Depiction of how to apply a ultrasound transducer on the neck of a patient to achieve the B-mode image of the carotid.

1.2 Long Term Goal

The long-term goal of this project is to measure the velocity of blood flow by using speckle decorrelation (SDC). It is a new approach that tries to overcome the limits imposed by the conventional and old Doppler methods. As a matter of fact, these methods assumed that blood flow moves parallel to the vessel's long axis and are able to measure the flow velocity only along the ultrasound beam [9]. Over the years some new techniques have been proposed, such as transverse oscillation [10], vector Doppler [11] and 2-D particle-tracking [12]. Nonetheless, all these approaches are only able to detect the flow velocity within the 2-D scanning plane which involves to assume the axial symmetry in the velocity profile of the vessel to measure the volume flow. Another technique was developed by Picot et al. and consisted in using the 2-D trough-plane velocity profile achieved from the vessel's oblique transverse view, to detect the volumetric flow with the conventional color Doppler [13]. The problem of this approach is in estimating the oblique angle during the measuring of the flow volume. This issue makes Picot's technique very difficult to implement in practice, especially under the transverse view. Zhou et al. [14] proposed a new method to reconstruct a full-field view of 3-D blood flow by using divergence free interpolation. This approach gives a good estimation of flow velocity in each dimension, but since a 2-D matrix ultrasound probe is adopted, it provides a huge amount of data and it is costly and difficult to achieve [15], [16]. SDC has the capability to measure the trough plane blood flow velocity with the use of a 1-D array probe [17], [18], [19]. The key point is to detect the volume flow by integrating the through plane velocity over the luminal area, scanned when the vessel and the probe are in the transverse view. The characteristic of ultrasound speckle decorrelation is that the SDC follows a Gaussian shape over time [20], [21]. Nonetheless the main limits of the ultrasound SDC was the low frame rate of the conventional Doppler [17], [18] and the too weak signal of the blood cells. To overcome these problems, the use of plane-wave ultrasound techniques and of the micro-bubbles contrast agents were proposed. The first solution can boost up to two orders of magnitude

the imaging frame rate. In addition to that, micro-bubbles contrast agents can increase the blood ultrasound signal. The combination of these two solutions has demonstrated, both in vitro and in vivo, the feasibility of ultrasound speckle decorrelation. The best results are obtained when the trough-plane velocity is 1 ms^{-1}, that is physiologically matched to most flow in cardiovascular system [19]. One more important advantage of using SDC is the possibility to detect the direction when the flow is bidirectional. To obtain this, the key idea is to rotate the transducer during the acquisition, in order to have a tilted angle between the vessel radius and the scanning plane [19].

1.3 Contribution of This Dissertation

The aim of this project is to adopt ultrasound SDC method in order to estimate blood flow velocity. To enhance the signal of blood cells, it was tested singular value decomposition filtering, in order to avoid the use of the micro-bubbles contrast agent. Feasibility of this approach was examined in laboratory, using experimental flow phantoms and computer simulations. The contribution of this thesis can be defined as follows:

i. Make in laboratory the blood mimicking fluid (BMF). This fluid replays some characteristics of blood, such as ultrasound reflection and scattering (Chapter 2).

ii. Develop a filter to enhance the blood signal. This particular kind of filtering is called SVD and has the capability to remove the signal of the tissue by keeping unchanged the characteristic of blood (Chapter 3).

iii. Estimate the blood flow velocity by adopting ultrasound speckle decorrelation. This approach is particularly useful in detecting the velocity when reverse flow is present, i.e. in most of the cardiovascular flow (Chapter 3).

iv. Compare the results obtained through ultrasound SDC with the real value of blood velocity in order to test the effectiveness and accuracy of the experiments (Chapter 4).

Caput 2

Background

In this chapter some basic knowledge necessary to well understand the contents of this project will be given. Firstly, a description of the field of Ultrasonic Imaging will be provided. In the second part of the chapter some concepts about fluid physics will be given. Finally, the rudiments of conventional imaging will be expounded.

2.1 Ultrasonic Imaging

The field of ultrasonic imaging is finding great success in clinics and its application is increasing more and more. In this section the physical aspects of ultrasonic propagation will be discussed. In addition, a description of ultrasound probes and of the characteristics of ultrasound images will be given.

2.1.1 Ultrasound Waves

Ultrasound waves are very useful in clinics, since it is the only non-invasive way to detect human tissues. They are mechanical waves with frequency above 20 kHz. In diagnostic imaging the range of frequency goes from 1 MHz to approximately 20 MHz, while for intra-vascular imaging the typical frequencies used are up to 50 kHz. Since ultrasounds are mechanical vibrations, no mass is moved when the medium is crossed by the waves. The only phenomenon that occurs is the oscillation of the particles of the medium around their mean positions. The propagation of a plane wave is shown in figure 2.1.

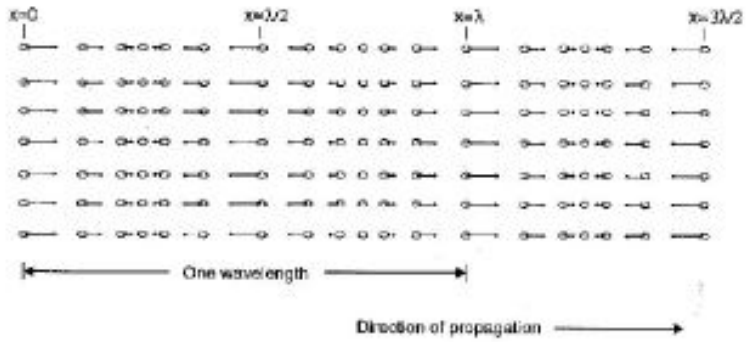

Descriptio 2.1: Reprinted from [22]. Particles displacement for a propagating ultrasound wave

The main direction trough which ultrasound waves flow is the longitudinal one and the speed of sound, also known as acoustic speed c , is dependent of the medium and is calculated as follows:

$$c = \sqrt{\frac{1}{\rho_0 k}} \tag{2.1}$$

where k is the adiabatic compressibility and ρ_0 is the mean density. Ultrasound waves are able to propagate in human body and the way they go through human tissue depends on a physical characteristic which is called acoustic impedance Z (Rayls, $kgs^{-1}m^{-2}$). Different tissues have different acoustic impedances, giving practically different ultrasound reflections. Z is related to the speed of sound c as follows:

$$c = \frac{Z}{\rho} = \sqrt{\frac{B}{\rho}} \tag{2.2}$$

where ρ is the density (kgm^{-3}) and B is the bulk modulus (Pa). Typically, the acoustic speed of human soft tissue is roughly 1540 ms^{-1} [23]. On the other side, blood has an acoustic speed of roughly 1570 ms^{-1} [23].

2.1.2 Ultrasound Propagation

Several phenomena can occur when ultrasound waves go through a medium or different media, i.e. two media with different acoustic impedance. Depending on the characteristics and the surface of the medium, the main effects that can occur, when ultrasounds are generated, are reflection, refraction, attenuation and scattering. Reflection is the characteristic by which a fraction of ultrasounds comes back to the transducer after bumping into a medium with different Z. According to the incident surface, reflection can be divided into specular and diffuse. When the ultrasound wave is reflected back in a singular direction, specular reflection occurs, as shown in the left part of figure 2.2. In this case the medium surface is large and smooth, such as bones.

Otherwise when the ultrasound wave returns to the transducer in various directions, diffuse reflection occurs, as shown in the right part of figure 2.2. All soft tissues, such

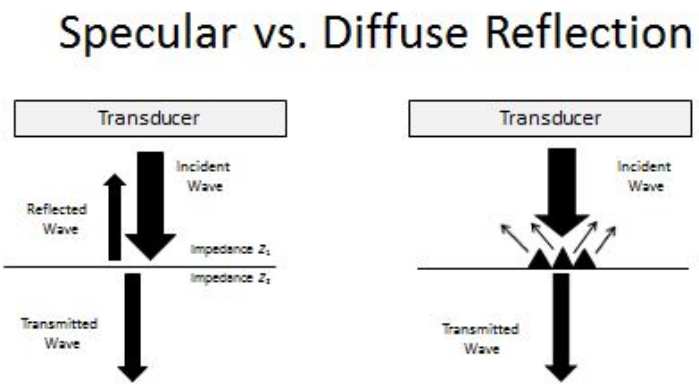

Descriptio 2.2: Reprinted from [24]. Comparison between two types of reflection. On the left side of the figure, specular reflection is shown; on the right side diffuse reflection occurs.

as muscles and fat, are responsible of this kind of reflection [24]. Refraction is defined as the change in direction of ultrasound waves crossing two different media. It is generated when ultrasounds strike with an oblique angle the boundary of two different tissues. The angle of refraction depends on the incident angle, i.e. the angle between the ultrasound wave and the boundary surface of the two media, and the propagation velocity in the two media. The greater is the velocity in the second medium the closer to the perpendicular is the angle. Refraction is regulated by *Snell's Law*:

$$\frac{\sin\theta_1}{\sin\theta_2} = \frac{v_1}{v_2} = \frac{n_1}{n_2} \tag{2.3}$$

Where θ_1 is the incident angle, θ_2 is the refracted angle, v_1 and v_2 are the velocities in the two respective media and n_1 and n_2 are the refractive index of the respective medium, as shown in figure 2.3.

Rayleigh scattering results when ultrasounds hit structures of small dimensions, compared to the wavelength. It is the typical phenomenon that occurs when there is the presence of red blood cells, whose average diameter is $7\mu m$.

Scattering consists in spreading the ultrasound wave in all directions and with uniform amplitude, after the contact of the wave with the surface of a particle, as shown in figure 2.4. Scattering depends on four main factors:

1. Dimension of the stricken particles (scatterers)
2. Number of scatterers
3. Ultrasound frequency
4. Dimension of the area where scattering particles are located.

The cumulative effect of absorption in the tissue, and scattering and reflection between the boundaries of different tissues is called attenuation. It is defined as the decreasing

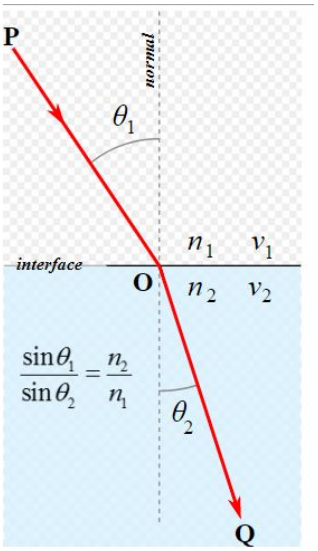

Descriptio 2.3: The ultrasound wave hits the interface of the different media, generating a refracted wave. The speed of the incident and refracted are different, with respect to the properties of the two media.

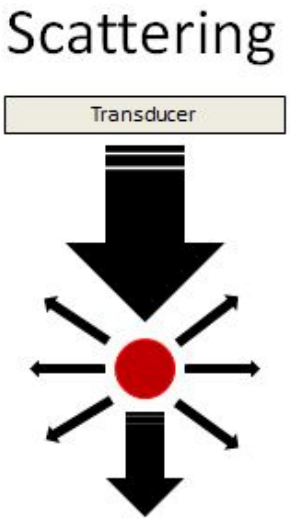

Descriptio 2.4: Reprinted from [24]. Representation of diffuse scattering.

intensity of ultrasounds energy as it goes through tissues. Generally, attenuation is low in fluid-filled structures and high in skin and muscles. In addition to that, the higher is the frequency of the wave the higher is the attenuation in the tissues. Figure 2.5 show the value of attenuation coefficient for different body tissues at 1 MHz of ultrasound frequency.

The relationship between attenuation and distance is defined through the attenuation coefficient μ and depends both on the frequency of ultrasounds and on the type of crossed tissues. The intensity of ultrasound wave is related to the attenuation coefficient with

Body Tissue	Attenuation Coefficient (dB/cm at 1MHz)
Water	0.002
Blood	0.18
Fat	0.63
Liver	0.5-0.94
Kidney	1.0
Muscle	1.3-3.3
Bone	5

Descriptio 2.5: Reprinted from [24]. Different values of attenuation coefficients in relation to body tissues.

respect to Lambert-Beer law:

$$I = I_0 e^{-\mu x} \tag{2.4}$$

Where I is the intensity of mechanical waves across some distance x, I_0 is the initial intensity of mechanical waves and x is the travelled distance. Normally an attenuation of 3 dB corresponds to a reduction in intensity by half. To avoid this obstacle, the returning signal should be amplified by ultrasound system.

2.1.3 Transducers

To generate an ultrasound image, a transducer needs to receive and process the scattering of acoustic waves in the medium [25]. It should be known that ultrasound beam into media is attenuated by reflection, scattering and absorption while only a part of this energy comes back to the transducer. Mostly transducers have two working mode: transmitting and receiving mode. The emitting mode is automatically selected when the probe generates ultrasound wave, while the receiving mode starts when the probe needs to get the reflected and scattered ultrasound wave. Generally, a transducer is made up of individual piezoelectric elements, whose property is to mechanically deform when a voltage potential is applied to its surface [26]. In blood flow imaging an array transducer is typically used. The probe used in this research project is Verasonics L11-4v (figure 2.6), which is a linear array transducer of 128 individual elements. The pitch of this probe goes from 0.298 mm to 0.302 mm and the elevation focus goes from 15 mm to 25 mm. Finally, the range of the sensitivity is form -64.5 dB to -59.5 dB.

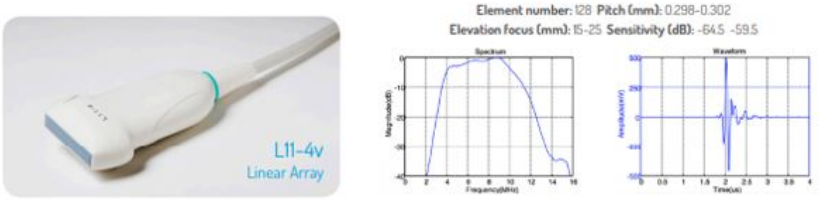

Descriptio 2.6: Verasonics probe L11-4v. On the right the spectrum and waveform are shown

In transmission mode, each individual element can be excited with a different time delay and the sum of the energy released by each element produces ultrasound beams. Each beam has specific focal position and emitting direction. The reception mode is based on beam-forming method, which is shown in figure 2.7. This process consists in delaying and summing the reflected ultrasound waves in order to form the ultrasound beams.

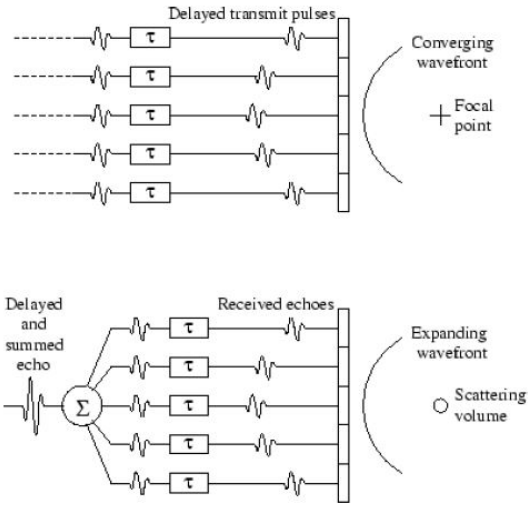

Descriptio 2.7: Reprinted from [27]. "A conceptual diagram of phased array beam-forming. (Top) Appropriately delayed pulses are transmitted from an array of piezoelectric elements to achieve steering and focusing at the point of interest. (For simplicity, only focusing delays are shown here.) (Bottom) The echoes returning are likewise delayed before they are summed together to form a strong echo signal from the region of interest".

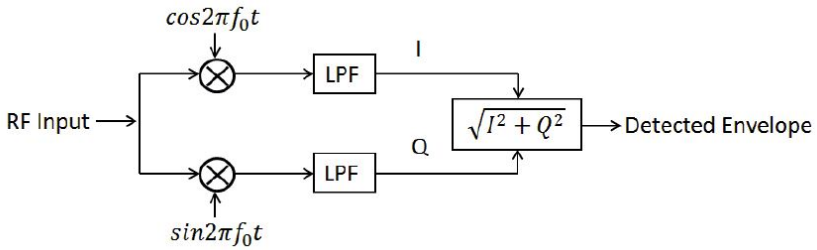

Descriptio 2.8: "The procedure of envelope detection. RF signals are demodulated by two local oscillators with transmitting frequency f_0. Demodulated signals are filtered by low-pass filters to generate I (in phase) and Q (quadrature) signals. The envelope of the complex IQ signal is then detected."

After having received the ultrasound signal, it is demodulated and filtered to generate the in phase I and quadrature Q components, whose envelope is detected to achieve more information about human body. This process is shown in figure 2.8.

2.1.4 Image Quality

The image quality is governed by two main factors, which are *Signal to Noise Ratio* (SNR) and the *Image Resolution*.

Signal to Noise Ratio

SNR is a dimensionless number which is index of how much the power of the wanted signal is greater than the power of the noise that affects the image. Noise is a casual variable that can come from the transducer itself, from the system and also from the medium. Signal to Noise Ratio is measured as follows:

$$SNR(z) = \frac{i_{avg}}{\sigma_i} \tag{2.5}$$

where i_{avg} is the average intensity of the signal, σ_i is the standard deviation of the signal, which represents the noise in the image and z is the travelled distance [28]. If σ_i is equal to zero, *SNR* tends to infinity which means that the image has no noise. As one can notice, *SNR* is directly proportional to signal power, which implies that an increasing signal power corresponds to a better *SNR*. On the other side, the *SNR* worsens with z because of the attenuation that is related to the depth. To avoid this problem, it is possible to increase the emitted signal energy, with respect to safe limits, or to increase the pulse transmitting length in order to provide more energy. Nevertheless, increasing the transmit pulse length implies decreasing bandwidth, i.e. worsening image resolution [22]. The 2.5 is correct from a mathematical point of view, but is meaningless from a perceptual point of view. A more common index of the quality of image is the Differential Signal to Noise Ratio (SNRd), which is directly related to the contrast of the image. SNRd is measured as follows:

$$SNRd(z) = \frac{i_a - i_s}{\sigma_i} = c\frac{i_s}{\sigma_i} \tag{2.6}$$

where i_a is the mean value of intensity in the *ROI*, i_s is the mean value of intensity in the background and c is the contrast.

Image Resolution

The image resolution is an important parameter necessary for establishing the quality of an image. It can be divided in three types of resolutions, which are *spatial resolution*, *temporal resolution* and *amplitude resolution*.

The spatial resolution is defined as the capability to distinguish two different near objects in an image. In other words, it is the minimum distance necessary for two objects to be independently discernible. In 2-D imaging it is classified in axial and lateral resolution. Axial resolution is the minimum gap between two scatters in the axial direction and it is normally expressed in couple of line per mm. Axial resolution is strictly dependent on the pulse length, that is the shorter is the pulse length the better is the axial resolution. On the other side, lateral resolution is the ability to distinguish between two scatterers at equal depth. This type of resolution varies with depth and depends on the beam-width [29]. It is maximum in the focal zone, which is the zone where the beam-width is minimum. For this reason, to increase lateral resolution, multi-focal imaging has been introduced [30].

Even if this approach provides a better lateral resolution, it comes to lower the temporal resolution since it reduces the frame-rate.

The temporal resolution is index of how many images can be produced by the device per unit of time. It is also known as frame-rate and is expressed in number of images per second. In this project the frame-rate has been set to 10000. The amplitude resolution is the capability to represent different colours in the image. In gray-scale images, it can be calculated though Weber's law, as follows:

$$c_{th} = \frac{\Delta i}{i} \tag{2.7}$$

where Δi is the difference of intensity between the ROI and the background, and c_{th} is the contrast threshold.

2.2 Flow Physics

Most of the characteristic of human blood can be described through physical and chemical properties. These characteristics may change in presence of pathological conditions. Furthermore, to study blood behaviour it is necessary to replicate a similar medium, i.e. a medium that has the same properties of blood. In this section all these elements will be debated.

2.2.1 Human Circularity System

Human circularity system is the main factor prone to supply tissues and organs with oxygen and nutrients. In addition, it has the aim to transport hormones and remove waste products resulting from metabolism. It is a network of three elements, which are heart, blood and blood vessels that undergo all human body. The heart is the core of human circulatory system. It is made up of a special cardiac muscle tissue that is able to contract and pump the blood within the circulatory system. It is divided into four parts, two atria and two ventricles and each side of the heart has one atrium and one ventriculus, as shown in figure 2.9.

The right atrium receives blood from inferior and superior venae cavae; the right ventriculus pumps blood into pulmonary artery. On the other side, the left atrium gets blood from pulmonary vessels and the left ventriculus draws blood into aorta [31].

Blood is a connective tissue made up of a water-based solution (*plasma*), where several elements, such as electrolytes, metabolites, vitamins and minerals are present and several cellular populations (*corpuscular portion*). This last portion is constituted for 99% by erythrocytes, also called red blood cells, and for 1% by leukocytes, also called white blood cells, and platelets. Blood main functions are to carry nourishments and to regulate homoeostasis. Blood vessels are all the canals through which blood flows. They are classified into three main classes, which are arteries, veins and capillaries. Arteries are blood vessels apt to transport blood from the heart to tissues and organs. Except for pulmonary arteries, which carry blood with carbon dioxide and waste products, all the arteries transport oxygenated blood. Veins are blood vessels that bring blood from peripheral body districts to the heart. With exception of pulmonary veins, which carry blood rich in oxygen and nourishments, all the veins are apt to transport waste products and blood rich in carbon

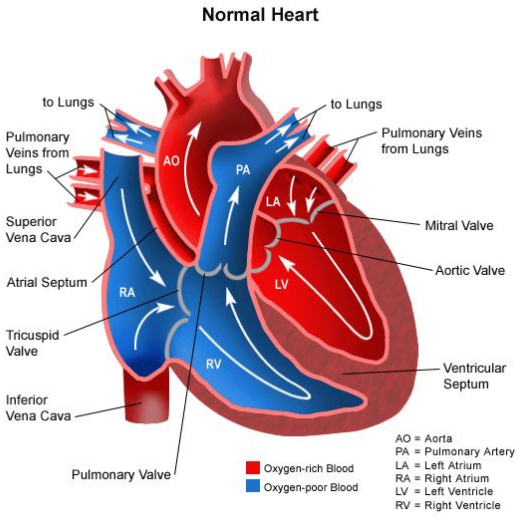

Descriptio 2.9: Representation of the anatomy of a normal heart.

dioxide. Both veins and arteries branch out in capillaries. These are very thin vessels that allows blood to exchange water and chemical materials.

In this thesis the big vessels are studied. Carotid artery (figure 2.10) is one of the biggest arteries in circulatory system and one of the most important as well, since it is responsible of the vascularization in head and neck. Carotid anatomy consists in one big branch (*common carotid artery*), which divided into two branches (*internal and external carotid artery*) at the level of thyroid cartilage. Internal carotid artery is responsible to carry blood into encephalon, eyes, forehead and nose. External carotid artery deals with the haematic supply of neck and face.

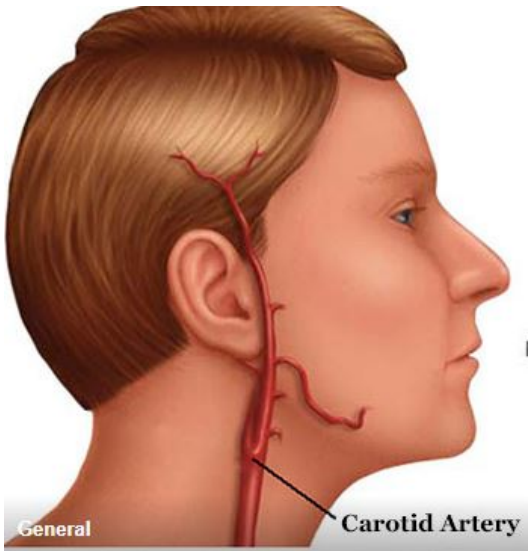

Descriptio 2.10: Representation of the anatomy of a normal heart.

2.2.2 Blood Pressure and Flow

Blood pressure is defined as the pressure that blood applies on the inner walls of the arteries. It is the result of two main factors which are systolic output, i.e. the performance of cardiac pump, and resistance provided by peripheral arterioles. Since the heart is a pulsatile pump, blood pressure is not constant in time. *Systolic blood pressure* (SBP) is the maximum value of pressure in arteries and occurs during the systole. *Diastolic blood pressure* (DBP) is the minimum amount of pressure, which occurs during the diastole. The difference between these two amounts of pressure is the so-called differential blood pressure or pulse pressure. The ranges of blood pressure for a healthy person is shown in table 2.1.

Tabula 2.1: Range of arterial blood pressure for healthy people [32].

Systolic, mmHg	**Diastolic**, mmHg
90-140	60-90

As a rule, in normal condition the maximum value of systolic blood pressure should be 140 $mmHg$, while the maximum value of diastolic blood pressure should be 90 $mmHg$ [32]. In capillaries blood pressure goes from a minimum of 10 $mmHg$ to a maximum of 35 $mmHg$, in normal condition for healthy people. Mean blood pressure is the integral mean of the infinite values that blood pressure assumes between systolic and diastolic blood pressure and can be calculated as follows:

$$p_m = \int \frac{p_a}{t} dt \tag{2.8}$$

Where p_m is the mean blood pressure, p_a is the blood pressure and t is the period of a cardiac cycle. Blood flow is defined as the amount of blood that in a unit of time passes a given point in the vessel. It is given by two factors, which are pressure difference between two points in the vessel and vascular resistance. Blood flow acts in accordance with *Ohm's law*, as follows:

$$F = \frac{\Delta p}{R} \tag{2.9}$$

where F is the flow, Δp is the difference of pressure between two points of the vessel and R is the resistance. As one can notice, flow is strictly dependent on the pressure difference. A bigger difference of pressure not only increases the amount of force that bumps the flow through the vessel, but also decreases the vessel resistance since it expands vessel walls. For example, a pressure of 100 $mmHg$ will raise the blood flow up to six times the value of blood flow at 50 $mmHg$ instead of two times [33]. The devices used to measure blood flow are called flow-meters and can work both inside and outside the vessel. Ultrasound devices are one of the most secure and non-invasive flow-meters that are able to measure the flow from the outside of the vessel.

2.2.3 Flow Phantom

The development of a fluid that is able to replicate blood properties is essential to study and test the results of this project. In vitro simulation represents a good investigative

way in vascular ultrasound studies. It requires the use of two fundamental tools that are flow phantom and *blood mimicking fluid* (BMF). Flow phantoms are experimental test beds capable to mimic blood flow characteristic within the vessels. It is fundamental that physical properties of human tissues match perfectly the physical characteristics of flow phantom in order to ensure good quality ultrasound images during the simulation [34]. To make the structure of a flow phantom Tissue Mimicking Material (TMM) and Vessel Mimicking Material (VMM) are required; the tissue mimicking material is essential to replay the acoustic properties of soft tissues, while the vessel mimicking material is necessary to reproduce the acoustic properties of vessel wall. In addition, a pump is required to pump the blood mimicking fluid through the phantom. In this project a pulsatile blood pump has been used and a pulse rate of 80 $stroke/min$ has been set in order to emulate an average heartbeat in normal condition 2.11.

Descriptio 2.11: Pulsatile blood pump by Harvard Apparatus.

Furthermore, blood mimicking fluid is needed to replay viscous and acoustic properties of blood, such as volume concentration of acoustic backscatter, viscosity, fluid density and scatter size. BMF has been prepared in the *ULIS* laboratory by following the receipt and procedure described by Zhou et al. [19]. This receipt has allowed to make a good fluid with 5 μm diameter particles, which is roughly the same size of real red blood cells. Even though it is a Newtonian fluid, its characteristics are very close to blood ones as one can see in the table 2.2 [35].

Tabula 2.2: Differences between Blood Mimicking Fluid and Blood characteristics [35].

	Blood Mimicking Fluid	**Blood**
Density kgm^{-3}	1037 ± 2	1060 ± 50
Viscosity $mPas$	4.01 ± 0.1	3.5 ± 0.5
Sound Speed ms^{-1}	1548	1570
Attenuation $dBcm^{-1}MHz^{-1}$	0.05 ± 0.01	0.21

To prepare the BMF all the elements shown in table 2.3 with the respective percentage by weight were used.

Tabula 2.3: Receipt for making Blood Mimicking Fluid [36].

Component	**Manufacturer**	**Weight (%)**
DI water	—	83.7
Glycerol (99 %)	Thermo Fisher Scientific, Waltham, MA, USA	10.0
5 μm Orgasol particles (2001 UD Nat 2)	Arkema, Paris, France	1.8
Dextran	Sigma-Aldrich	3.3
Tergitol surfactants	Sigma-Aldrich	0.9
Potassium sorbate	Sigma-Aldrich	0.3

Figure 2.12 shows how the BMF appears.

Descriptio 2.12: Blood mimicking fluid.

2.2.4 Pathological Conditions

Many pathological conditions can modify the structure of the vessels leading to different values of pressure and blood flow, with respect to normal conditions. In clinics ultrasound imaging is a common way to detect blood flow and therefore to monitor a pathological condition. The most common disease that affects blood vessel is arteriosclerosis. In normal condition vessels are flexible and their inner walls are smooth, while when arteriosclerosis occurs vessels walls progressively stiffen and the inner lumen reduces. This phenomenon is caused by an accumulation of sediments, also known as atheromatous plaques. Over time these plaques can increase their thickness, which reduces the inner diameter of the vessel and limits the blood flow. When this takes place in the carotid, we talk about carotid stenosis, as show in figure 2.13.

In most cases carotid stenosis results in carotid sinus, i.e. at the level of the fork which divides the carotid into internal and external carotid. Other important pathologies related to a not physiological blood flow are high blood pressure, also known as arterial hypertension, and low blood pressure, also known as arterial hypotension. These diseases consist respectively into a sudden raising and fall of blood pressure and can be determined by several factors such as ambiental factors, genetic factors or genetic heredity.

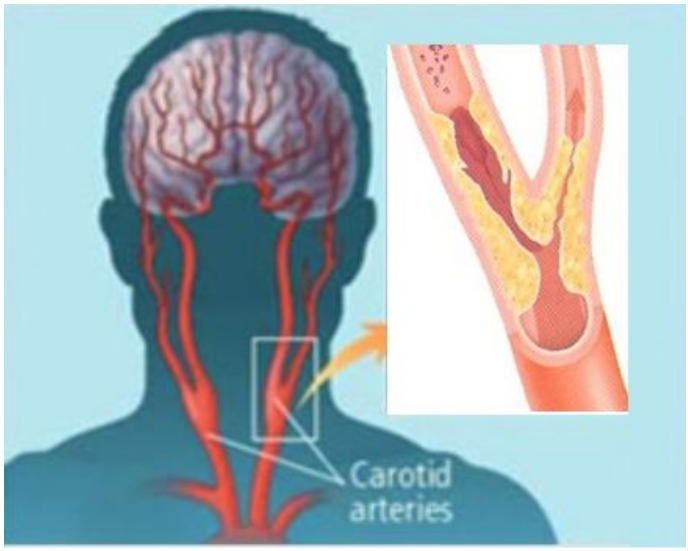

Descriptio 2.13: Representation of a carotid artery stenosis.

2.3 Medical Ultrasound Systems

The field of medical ultrasound has been constantly growing since its first application and this leaded to the evolution of the medical ultrasound systems. Currently the improvement of these systems allows to display anatomic grey scale images as well as blood flow in real time [22]. In this section a description of most important ultrasound systems is given.

2.3.1 Grey Scale Ultrasound Systems

Medical ultrasound systems give the operator the possibility to set different modes, i.e. different operational states. In ultrasound imaging the use of different modes is fundamental to examine different tissues. Currently, three modes are used in clinics: A-Mode, B-Mode and M-Mode.

A-Mode, also known as Amplitude Modulation, consists in displaying the amplitude spikes at different heights. The figure 2.14 provides an example of an A-Mode image, where horizontal axis represents the depth and vertical axis the amplitude. This mode is very common in ophthalmology studies for detecting the optic nerve.

B-Mode, also known as Brightness Modulation, is the most common mode in ultrasound imaging. It consists into displaying a 2-D map of B-Mode data. It depends on the brightness, therefore on the intensity of the echo. The figure 2.15 shows an example of B-Mode image, where vertical axis represents the echo intensity and horizontal axis represents the depth.

M-Mode, also called Motion Mode or Time Motion Mode, is used for evaluating moving body parts. It consists into displaying a one-dimensional image and is commonly used in cardiac imaging. The principle of M-Mode is to record the amplitude and rate of motion in real time.

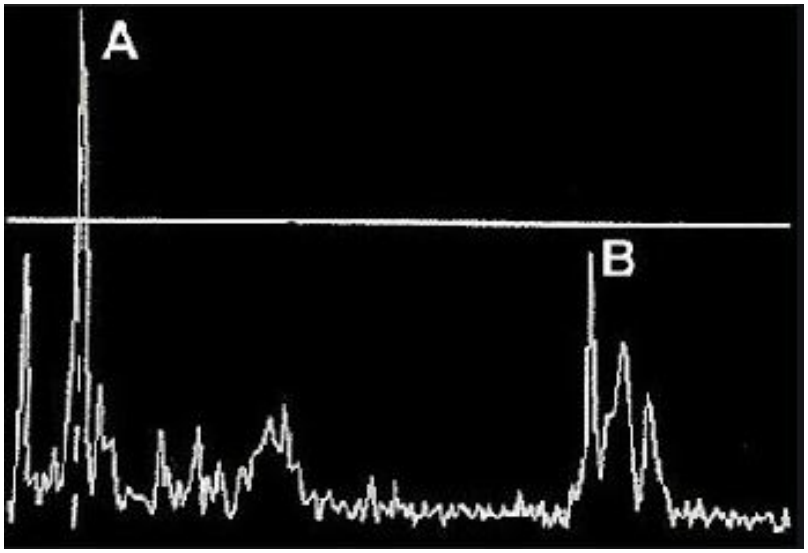

Descriptio 2.14: Representation of an A-mode image.

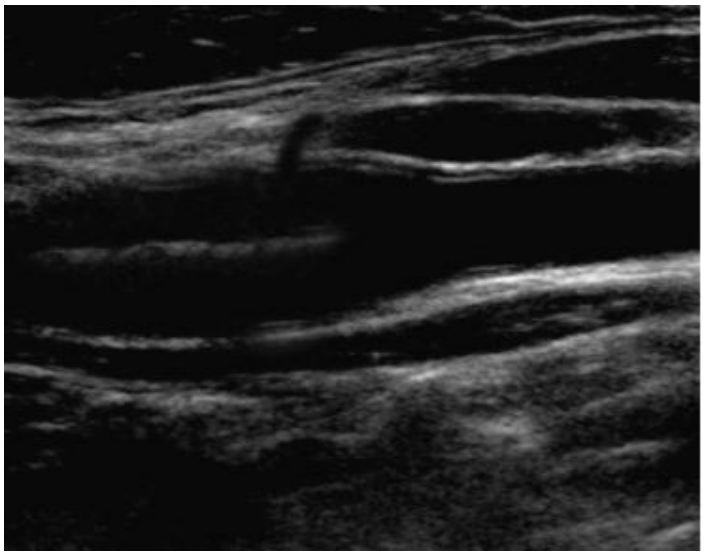

Descriptio 2.15: Representation of the B-mode image of a normal carotid artery.

2.3.2 Continuous Wave Systems

Continuous wave system is the earliest and simplest method used in blood flow detection. It is based on Doppler effect, which was discovered by Christian Andreas Doppler, an Austrian physicist. This effect describes the change in frequency that results when source and target are in movement. The frequency received by an observer can be calculated as follows:

$$f_r = f_0 \frac{c + v_0}{c + v_x} \tag{2.10}$$

where f_r is the frequency for the observer, f_0 is the transmitted frequency, c is the speed of the sound in the medium, v_x is the speed of the source and v_0 is the speed of the observer. If the observer and the source move closer, the detected frequency is higher than

the emitted frequency. On the contrary, if the source move away from the observer, the detected frequency is lower than the emitted one. In blood detecting the transducer acts like the fixed source while blood acts like the moving observer. Generally, a continuous wave Doppler probe has two independent elements: one to transmit and the other to receive ultrasound waves. The frequency received by the transducer, i.e. the f_r, contains both the transmitted frequency and the Doppler frequency. The Doppler frequency is defined as the shifted frequency between the transmitted and received signal, and can be calculated as follows:

$$f_d = f_r - f_0 = 2f_0 \frac{V cos\theta}{c} \tag{2.11}$$

where f_d is the Doppler frequency and V is the blood velocity measured at angle θ to the axis of transmission. One can notice that if f_r is higher than f_0, i.e. observer is moving close to the transducer, the Doppler frequency is positive. Contrary, if f_r is lower than f_0, i.e. observer is moving away from the transducer, the Doppler frequency is negative. The term $Vcos\theta$ represents the axial velocity and is the only projection of the velocity which can be fully determined, since it is parallel to the beam direction [37] [30].

From the 2.11 blood velocity can be calculated, as follows:

$$V = f_d \frac{c}{2f_0 cos\theta} \tag{2.12}$$

Figure 2.16 provides a common configuration of the continuous wave Doppler. As one can notice, the transducer simultaneously transmits and receives the ultrasound beam. The resulting signal has the Doppler shift of the emitted signal. The continuous wave Doppler is the only way to measure the Doppler shift, that is the shifted frequency caused by a moving medium. On the other side, continuous wave system lacks the possibility to detect the depth in tissue, which may result in detecting a wrong Doppler frequency if two vessels are close to each other.

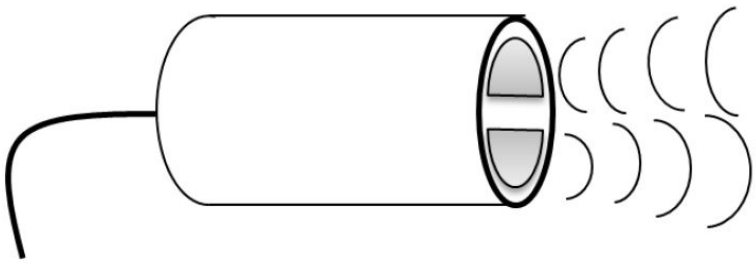

Descriptio 2.16: A continuous-wave Doppler transducer contains two separate elements to transmit and receive ultrasound waves.

2.3.3 Pulse Wave Systems

To solve the problem of continuous wave system, Baker (1970) and others [38] proposed the Pulsed Wave System. This method allows the transducer to work alternatively as

emitter and receiver. The transducer emits a number of pulses into the medium with a fixed *pulse repetition frequency* (PRF) and receives the back-scattered signal. The back-scattered signal will be sampled at the same time period of the pulse emission. The received signal will be multiplied by the centre frequency of the pulse and then low pass filtered. Pulse wave systems allows to detect the displacement of the backscattered signal, which is a consequence of the flowing of the blood. It is important to notice that, despite this method is also called Doppler system, it is not based on Doppler effect. As a matter of fact, the aim of pulse wave system is to detect the shift in the position of scatterers and not to detect the difference between transmitted and receipt frequencies. The received signal, after demodulation and filtering, is shown in figure 2.17. The lines shown in the left part of figure 2.17 are generated by the pulses emitted at PRF and are able to provide the signal at a fixed depth. They keep both the amplitude and phase of the signal. One should know that is a signal is originated by a moving target, as in the case of blood flow, its phase will change with respect to subsequent pulse beats. The resulting sampled signal is shown on the right side of figure 2.17. It is achieved by taking into account the amplitude of each pulse at fixed time [22]).

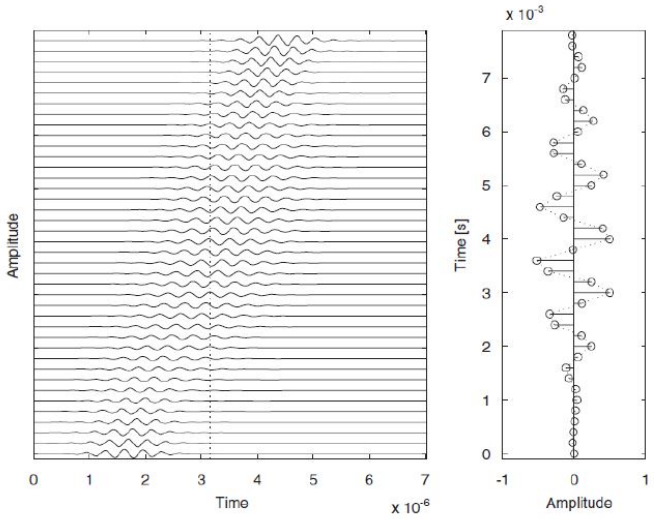

Descriptio 2.17: Reprinted from [16]. "RF sampling of single pulse moving away from the transducer. The left graph shows the different received RF lines, and the right graph is the sampled signal. The dotted line indicates the time when samples are acquire".

The time shift t_s of the signal from pulse to pulse is defined as follows:

$$t_s = \frac{2Vcos\theta}{c} T_{prf} \tag{2.13}$$

where T_{prf} is the time between two consecutive pulse emissions. The scatter distance between two emissions can be evaluated by recording the signal at a fixed depth and it is proportional to the axial velocity. For this reason, if the probe emits a sinusoidal signal, the acquired signal for a single scatter at $i_t h$ pulse is:

$$r(i) = a(i) \sin 2\pi f_{pi} T_{prf} + \alpha \tag{2.14}$$

where $a(i)$ is the amplitude of the i_{th} pulse, α is a phase factor related to the depth, f_0 is the emitted frequency and f_p is calculated as follows:

$$f_p = \frac{2Vcos\theta}{c} f_0 \tag{2.15}$$

Pulse wave systems give the possibility to develop the velocity profile and, in addition, make the investigation of the vessel more accurate. Furthermore, this method can generate duplex mode images, i.e. images providing both B-Mode image and velocity spectrum. Figure 2.18 is a typical example. The top side of the figure displays an anatomic image (in B-Mode) of the carotid artery, while in the bottom side the velocity spectrum of the blood flow is displayed.

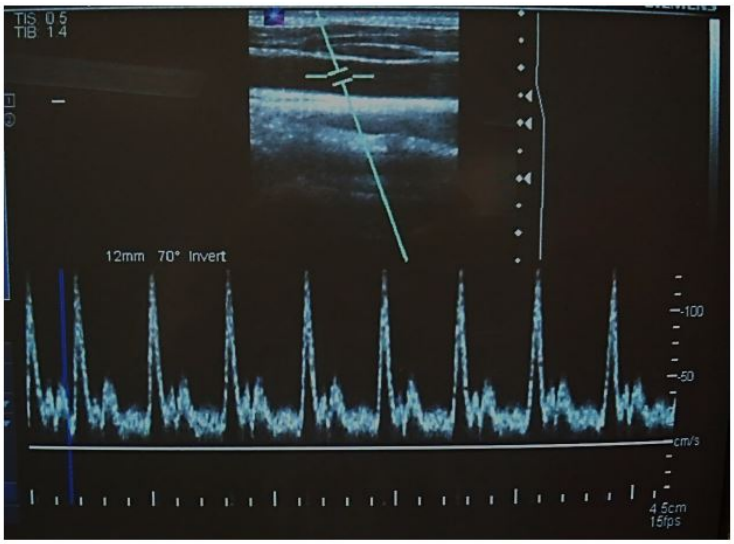

Descriptio 2.18: "A screen shot of spectral Doppler showing both B-mode image and spectrogram of the carotid artery. The Doppler signal is collected from the gate along the beam direction".

2.3.4 Color Doppler

Kasai et al. discovered a new method to quick estimate the mean velocity of a moving target by using the autocorrelation technique [39]. It is based on the pulse wave system, but unlike this system which detects the volume flow only for a fixed sample volume and for short time period, Color Doppler system is able to evaluate volume flow of different samples. Typically, $8-16$ lines of data are acquired and divided into a number of segments with respect to the resolution-cell [40]. Successively, volume flow velocity will be detected from the complex sample acquired, as shown in figure 2.19.

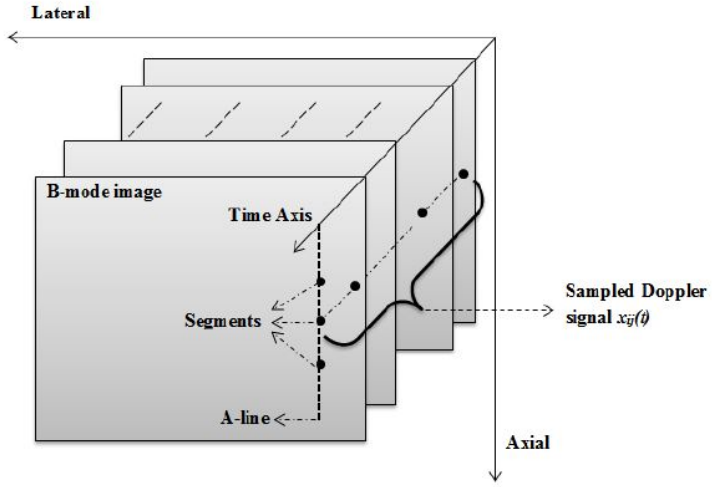

Descriptio 2.19: "A diagram of color Doppler. Samples at specific locations in successive B-mode images are collected to form the Doppler signal $x_{ij}(t)$, where i and j represents the location of the samples and t represents the sampling time."

Theoretically, it is possible to measure the mean blood flow velocity at a fixed depth from the complex samples acquired, as Kasai et al. (1985) [39] demonstrated. The mean flow velocity can be evaluated as follows:

$$\bar{\omega} = \frac{\int_{-\infty}^{\infty} \omega P(\omega) d\omega}{\int_{-\infty}^{\infty} P(\omega) d\omega} \quad and \quad \bar{v} = \frac{\bar{\omega}}{2\pi f_0} \frac{c}{2} \tag{2.16}$$

where ω is the angular frequency of the sampled signal, $P(\omega)$ is the power spectral density, $\bar{v}$ is the mean velocity of flow and $\bar{\omega}$ is the mean angular frequency. Due to the complexity of this approach in practice, an alternative method to measure the mean frequency has been proposed. This method is based on the autocorrelation function, as follows:

$$R_{ij}(\tau) = \int_{-\infty}^{\infty} x_{ij}(t) x_{ij}^{*}(t-\tau) dt \tag{2.17}$$

where $x_{ij}(t)$ is the sampled signal at a specific location (i,j) and time (t). $R_{ij}(t)$ is the autocorrelation function of $x_{ij}(t)$ within time interval τ and $*$ stands for complex conjugate. From the autocorrelation function it is possible to calculate the mean value of flow velocity, as follows:

$$\bar{v} = -\frac{c}{4\pi f_0 T_{prf}} \arctan\left(\frac{Im(R_{ij}(T_{prf}))}{Re(R_{ij}(T_{prf}))} \right) \tag{2.18}$$

where T_{prf} is the pulse repetition frequency and $Re(R_{ij}(T_{prf}))$ and $Im(R_{ij}(T_{prf}))$ are respectively the real and imaginary part of the autocorrelation function.

Figure 2.20 provides a typical color Doppler image of a carotid artery and jugular vein. The colours are overlapped on a B-Mode image and are indexes of the direction and value of the blood flow velocity. In the carotid the colour is red, which indicates that the blood

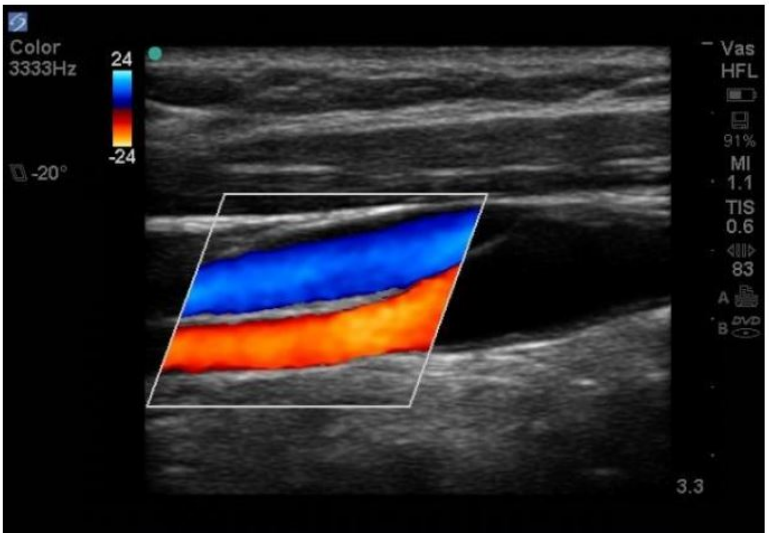

Descriptio 2.20: "A screen shot of color flow image of carotid artery bifurcation. The velocity information is superimposed on the B-mode image. The color represents the direction of the blood flow."

moves towards the probe, while in the jugular the colour is blue, which means that the blood moves away from the probe.

Caput 3

Blood Flow Velocity Estimation

Measuring blood flow is one of the most useful and challenging functions in ultrasound imaging systems. As analysed in chapter 2, the estimation of blood flow velocity is based on the capability of the transducer to emit ultrasound wave and receive the reflected wave. One of the first and most common method used is *Color Doppler*, but it is well known that this method is only able to detect the axial velocity. In this chapter *Ultrasound Speckle Decorrelation* (*SDC*), that is a new approach capable to overcome the limits of *Color Doppler*, will be presented.

3.1 Clutter Filtering - Singular Value Decomposition

To have a good estimation of blood flow, it is necessary that the back-scattering of blood is quite strong compared to the back-scattering of tissues. Generally, the blood signal is on the order of 10 to 100 times smaller than the signal coming from tissues and vessel boundaries. As a consequence, the signal of blood can be corrupted or loomed by the stationary echoes' signal. To overcome these problems, the main solutions are to enhance blood signal by using some external agents like micro-bubbles contrast agents [41], or to remove the too strong signal from tissues by applying some filtering [42]. In this project a new spatio-temporal clutter filtering, that is *Singular Value Decomposition* (*SVD*), has been used.

3.1.1 Principle Aspects

The Singular Value Decomposition is a particular kind of clutter filtering that allows up to a four-dimensional approach, 3-D in space and 1-D in time. Thanks to this multidimensional system, *SVD* is able to overcome all the limits imposed by conventional filters which are based on high pass temporal filtering and operate only on the temporal dimension (1-D). In particular, *SVD* filtering takes benefits from the different spatio-temporal coherence of blood motion with respect to the tissue.*SVD* filtering is based on two main principles. The first one is that tissue motion is supposed to be very slow compared to red blood cells, which means that demodulated blood and tissue signal have no overlapping spectra centred on Doppler and zero frequency respectively. This give the possibility to adopt infinite pulse response filters (IIR) or finite pulse response filters (FIR) to temporal filter the raw signal [43] [44]. Nevertheless, these filters are not useful in enhancing blood signal since they are difficult to optimize. The second principle on which *SVD* relies is

that tissue is less deformable than red blood cell arrangement in plasma, meaning that tissue signal has a higher spatial coherence than blood one in ultrasound imaging. Based on the spatial coherence, many authors such as Ledoux et al. [45], Yu and Lovstakken [46] and Kruse and Ferrara [47], proposed several clutter filters to intensify blood signal. Unfortunately, in all the proposed methods differentiation between blood flow and tissues is affected by a poor ensemble length, that is a poor number of ultrasound pulses per line of colour. As a consequence, the number of spatial samples is limited. *SVD* filtering represents a good solution to overcome all the limits all the traditional methods are affected by. It has been demonstrated that the application of Singular Value Decomposition filtering on ultrasound imaging works well but can lead to a worse spatial resolution in filtered image [48] if the frame-rate is too high. On the contrary, it is important to highlight that the higher is the frame-rate the better is the *Signal to Noise Ratio*, which is a characteristic to pursue. In addition, it has been proved that it is possible to improve the resolution using a set of tilted planes combined after the beam-forming [49] [50]. Because of massive computational costs it is impossible to have high frame-rate and high number of tilted angles, so it has been necessary to reach a trade-off between these two characteristics. Since the aim of this project is to measure the mean velocity of blood flow and the experimental conditions were ideal[1], it has been chosen to set a high frame-rate (Frame-rate = 1000) and no tilted angle (number of tilted angles = 1). These two assumptions will lead to filtered images with high *SNR*, which implies high contrast, but with a slightly worse spatial resolution.

3.1.2 Mathematica Aspects

An ultrasound image can be represented under a complex variable *s(x,z,t)*, where x is the lateral dimension along the transducer array, z is the depth in the medium and t is the time. It has been assumed that the signal is represented by the summation of three terms, as follows:

$$s(x,z,t) = c(x,z,t) + b(x,z,t) + n(x,z,t) \tag{3.1}$$

where c stands for clutter signal, b stands for blood signal and n stands for noise. All these terms have different spatio-temporal characteristics. $n(x,z,t)$ is a thermal/electronic noise and is considered as zero mean Gaussian white noise. $b(x,z,t)$ is assumed to be a high temporal frequency signal and $c(x,z,t)$ is assumed to be a low temporal frequency signal. The spatio-temporal characteristics of blood and tissue signals can be analysed both qualitatively and quantitatively. In order to qualitatively compare spatial and temporal signals it is necessary to introduce a new simplified signal $\bar{s}(x,z,t)$, that can be calculated as follows:

$$\bar{s}(x,z,t) = \frac{s(x,z,t).s^*(x,z,t)}{|s(x,z,t)|^2} \tag{3.2}$$

where $\bar{s}(x,z,t)$ is the time average value of s and $*$ is the complex conjugate. Thanks to this simplified new variable it is possible to remove any phase shift and amplitude difference between two pixels signals, meaning that the two signals are compared only

[1]Blood mimicking fluid flows with a fixed pulsating period and no muscular artefact is present

with relation to their shape. Figure 3.1 provides a good example of a qualitatively spatio-temporal comparison between two pixels signals.

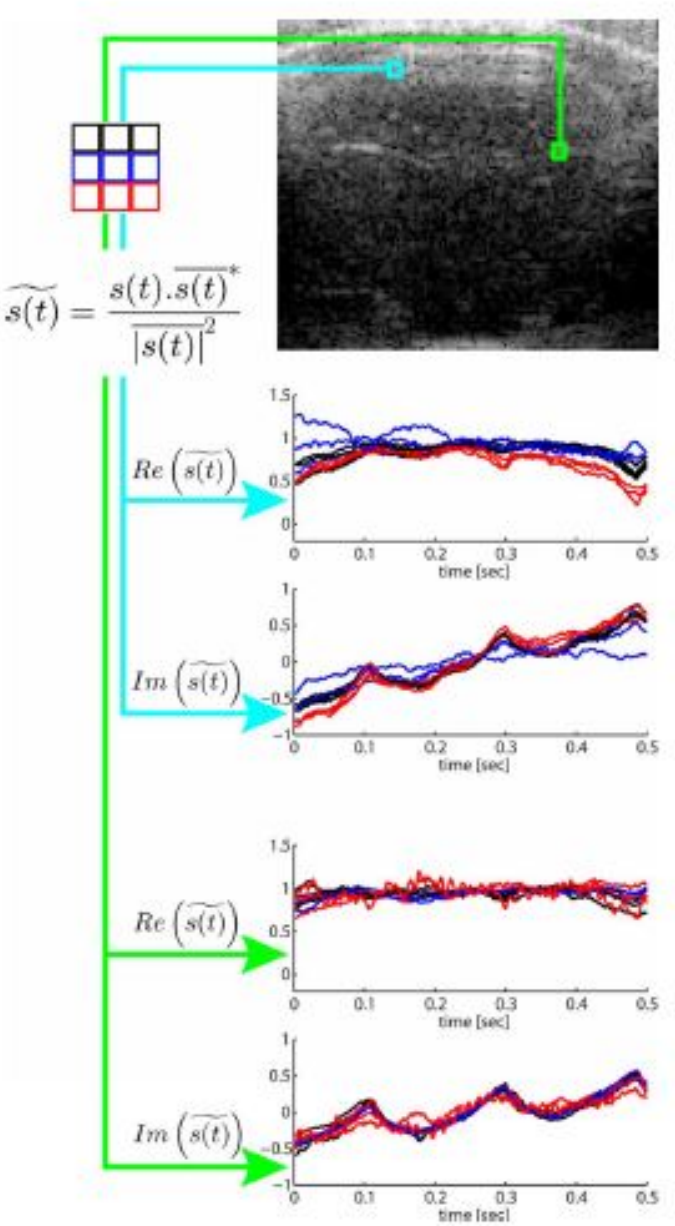

Descriptio 3.1: "Typical example of an Ultrafast Acquisition. The top image depicts $s(x, z, t) = 0$ of an Ultrafast acquisition acquired during 0.5 s at a Frame Rate of 500 Hz, on the brain of a thinned skull rat (scale bar = 1 mm). To have an insight into the temporal dimension of this Ultrafast acquisition, two neighbourhoods of nine pixels have been chosen in the image (green and cyan squares). Inside each pixel, the simplified signal $\bar{s}(x, z, t)$ is calculated to get rid of phase difference and amplitude difference from one pixel to another. $\bar{s}$ is then plotted with color respective to the position in the nine pixel neighbourhood (black, blue or red). This illustrates that signal in close pixels is very similar in shape."

The quantitatively comparison between the two signals can be done through the Covariance Matrix of Neighbouring Pixels. Figure 3.2 provides the Covariance Matrices both for blood (HF) and tissue (LF) signals.

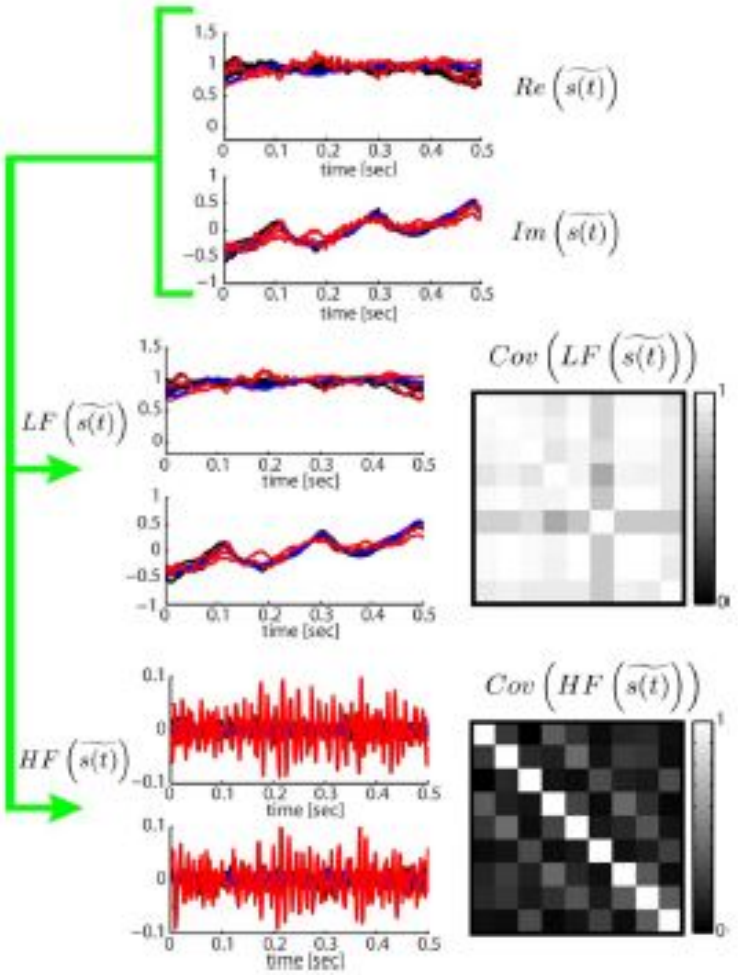

Descriptio 3.2: "The same data than in the green nine pixel neighborhood of figure 3.1 are filtered using a 50 Hz cut off 4^{th} order Butterworth filter typically used to discriminate between tissue and blood flow signals, and on the graphs it can be observed that the low frequency (LF) part of the nine pixel temporal signal are really similar in shape and seem highly correlated, whereas the blood signal (HF)seem highly decorrelated. On the right are displayed the 9×9 covariance matrix (magnitude) of the normalized zero-mean complex signals, for the low frequency and high frequency part respectively. HF Blood signal is indeed highly decorrelated compared to LF tissue signal."

One should know that tissue signal is highly correlated and, consequently, its covariance matrix has a high degree of correlation. On the contrary, blood signal has a poor spatial coherence, meaning that its covariance matrix is almost diagonal. On the base of covariance estimation and through the singular value decomposition of raw data it is possible to distinguish the blood signal from the tissue one. The spatio-temporal matrix *s(x,z,t)*

corresponds to the raw data cine loop achieved during the ultrasounds acquisition. It is a set of $n_x \times n_z \times n_t$ samples, where n_x is the number of samples along x-direction, n_z is the number of samples along z-direction and n_t is the number of time samples. This matrix is then reshaped under a *Casorati matrix* **S**. *Casorati's* approach consists into reshaping the 3-D raw data matrix into a new 2-D space-time matrix form, whose dimensions are $(n_x \times n_z \times n_t)$ [42].

The employment of *SVD* filtering consists into redrafting the *Casorati matrix* as the product of three matrices, as follows:

$$\mathbf{S} = \mathbf{U}\Delta\mathbf{V}^* \tag{3.3}$$

where **U** is an orthonormal matrix with dimensions ($n_x \times n_z$, $n_x \times n_z$), **V** is an orthonormal matrix with dimensions (n_t, n_t) and Δ is a non-square diagonal matrix with dimensions ($n_x \times n_z$, n_t). In addition, it is important to point out that columns of **U** matrix are spatial singular vectors of **S**, columns of **V** matrix are temporal singular vectors of **S** and the main diagonal of Δ are the ordered singular values. Under this theory, the matrix **S** can be written as the sum of weigh, ordered, separable matrices A_i, where A_i are the outer product of the i-columns of the matrices **U** and **V**.

$$\mathbf{S} = \sum_i \lambda_i \mathbf{A}_i = \sum_i \lambda_i U_i x V_i \tag{3.4}$$

In this way, *SVD* is used to rewrite **S** matrix into the sum of vectors that can be spatial and temporal filtered. The filtering of the data, i.e. the removing of clutter signal, is performed by assuming that tissue echo is concentrated in the first singular vectors. Based on this assumption, to remove the tissue signal it is necessary to chose a threshold n, which defines the number of singular vectors that should be removed from the raw signal. Thus, the blood signal that is obtained after applying the **SVD** filtering to the raw signal can be evaluated, as follows:

$$s_{blood}(x, z, t) = s(x, z, t) - \sum_i \lambda_i \mathbf{I}_i(x, z) V_i(t) \tag{3.5}$$

3.1.3 Critical Aspects

Since *SVD* filters the data removing clutter and noise signals, it is inevitable that the new filtered data will be partially distorted. In order to limit the image distortion, it is important to choose the threshold n in the proper way. Demené et al. [42] suggested a very simple method to choose the value of n. It consists in analysing the main diagonal of the Δ matrix, containing the ordered singular values λ_i. Figure 3.3 provides an example of the plot of singular values.

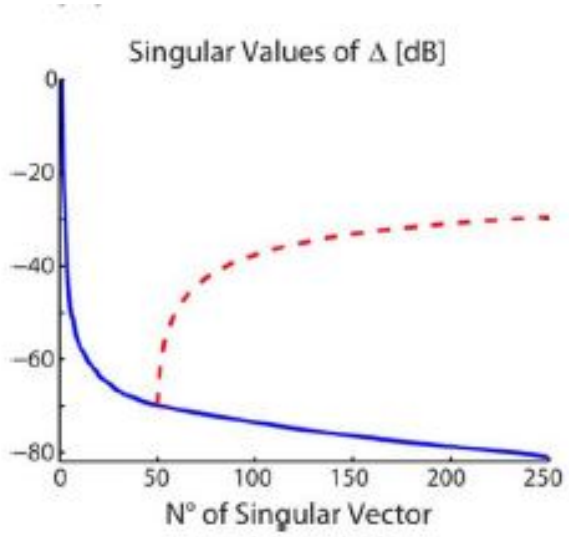

Descriptio 3.3: "Singular values of the matrix Δ (solid blue) expressed in dB and cumulative sum of those singular values from n° 50 (dashed red)."

The x-axis represents the number of singular vectors, while the y-axis represents the singular values in dB scale. The left side of the value n represents the tissue, i.e. the clutter signal, and it is the part that needs to be remove, while the right side represents the blood. The threshold n is chosen intuitively by selecting the point where the curve starts to be flat. Thereafter, the threshold is manually tuned until the resulting filtered data is acceptable. This basic approach has a huge temporal cost since several trials have to be done to find a reasonable threshold and, in addition, it is strictly operator dependent. To overcome these limitations a new adaptive method has been used in this project. Demené et al. [42] proposed a threshold estimator method based on the spatial singular vectors U_i. Since it is verified that blood and tissue signal have different spatial distributions, it should be known that U_i vectors are correlated between blood subspace and tissue subspace, but they are not correlated between them. As a consequence, from the correlation matrix $\mathbf{C}$ of size (n_t,n_t) it is possible to discriminate three regions, which are blood subspace, clutter subspace and noise subspace. Figure 3.4 provides an example of the correlation coefficients matrix.

In the almost ideal scenario, as in vitro experiments are, tissue, blood and noise areas do not overlap, therefore are clearly identifiable. Detecting the boundary between tissue and blood areas represents a new adaptive estimator for the optimal SVD threshold. Moreover, it is possible to select a second threshold, by finding the boundary between blood and noise areas, that allows image de-noising. The double threshold adaptive estimator represents the best available method to detect the thresholds for SVD filtering, since it is operator independent and gives the possibility to enhance the blood signal and remove the noise. The results of applying SVD filtering with the double threshold adaptive estimator will be presented in chapter 4.

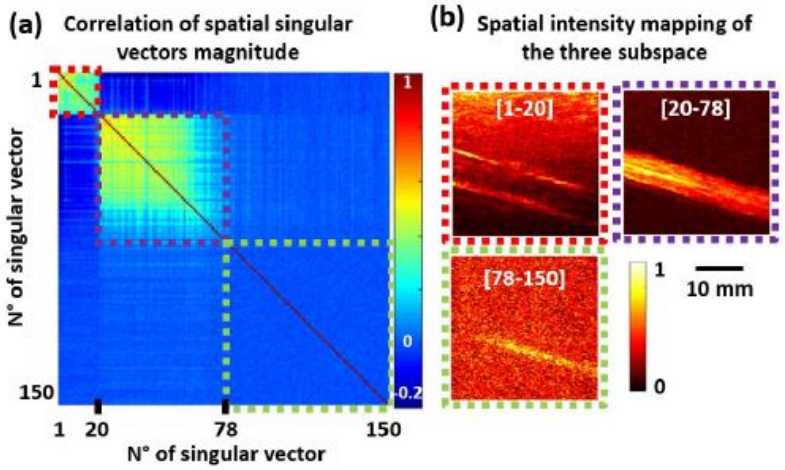

Descriptio 3.4: "Spatial criteria for threshold selection. (a) Incoherent correlation matrix of spatial singular vectors, for a plane wave ultrafast Doppler acquisition on a flux phantom. Three highly correlated areas appear. (b) Spatial vectors are incoherently averaged in the 3 areas, giving intensity maps. From 1 to 20 (red dotted squares), vectors describe the tissue and the canal walls. From 20 to 78 (purple dotted squares), spatial vectors represent the blood flow. From 78 to 150, spatial vectors account for mostly noise, yet with remaining blood signal."

3.2 Velocity Estimator

Conventional approaches are only able to measure the in-plane components flow velocity, which represents a very strict limitation for flow measurement. Furthermore, no current practical and effective solution exists for the 3-D volume flow measurement due to high system cost and challenges in actual 3-D imaging techniques. In this section a new method capable of measuring the volume flow will be introduced.

3.2.1 Speckle Decorrelation Method

SDC represents the most innovative solution to calculate the volume flow. Through this method it is possible to detect the out-of-plane velocity component, while the in-plane velocity components are tracked through the Ultrasound Imaging Velocimetry method (*UIV*). The volume flow is then calculated by integrating the overall velocity in the luminal area of the vessel. The fundamental principle *SDC* consists in assuming that the decorrelation rate can be extract independently for each direction [51] [40]. To assume that, it is necessary that the type of speckle is fully developed, i.e. the amplitude and phase of each scattering echo are not dependent of each other. If the speckle is fully developed, the decorrelation rate follows a Gaussian shape in each direction. Rubin et al. [52] demonstrated that the relation between the autocorrelation function of the echo signal in the elevational direction can be described, as follows:

$$R_I(\Delta r) =< I_d >^2 (1 + ||\rho(\Delta r)||^2) \tag{3.6}$$

where $< Id >$ is the mean diffuse intensity and is constant with position, $||\rho(\Delta r)||^2$ is the normalized coherence factor and $R_I(\Delta r)$ is the autocorrelation function of the echo signal intensity. The relation between $R_I(\Delta r))$ and $||\rho(\Delta r)||^2$ can be approximated as proportional since $< Id >$ is constant with position. Thus, dividing all the terms of the equation 3.6 for $< Id >^2$, normalized autocorrelation function can be found, as follows:

$$C_I(\Delta r) \simeq ||\rho(\Delta r)||^2 \tag{3.7}$$

where $C_I(\Delta r)$ is the normalized autocorrelation function. It has been demonstrated that the normalized coherence factor $||\rho(\Delta r)||^2$ follows a Gaussian shape in the Fraunhofer region[2] [52] [53], as in:

$$||\rho(\Delta r)||^2 \simeq e^{\left(\frac{-\Delta r^2}{2\sigma_y^2}\right)} \tag{3.8}$$

The Gaussian curve is dependent of the position and the transducer settings. Figure 3.5 provides an example of the shape of the correlation coefficient between B-mode image frames from a speckle phantom.

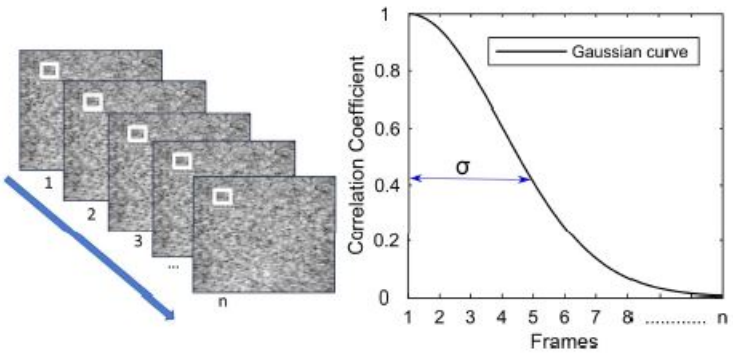

Fig. 1. Intensity values between a series of patches (marked with white boxes) from B-mode frames in the elevational direction (frame 1 to frame n) decorrelate and the decorrelation rate follows a Gaussian curve.

Descriptio 3.5: "Intensity values between a series of patches (marked with white boxes) from B-mode frames in the elevational direction (frame 1 to frame n) decorrelate and the decorrelation rate follows a Gaussian curve."

It is important to underline that to obtain this Gaussian shape both settings and position of the transducer need to be fixed. The equation for obtaining the correlation coefficient $C_{Icali}(n)$ is specified as follows:

$$C_{Icali}(n) = e^{\left(\frac{-(n\Delta d)^2}{2\sigma_y^2}\right)} \tag{3.9}$$

where Δd is the displacement between two consecutive frames and n is the number of frames. σ_y is the beam correlation width (BCW) in the y-direction, that is the elevational

[2]it is the far field region, that is the region where ultrasound beam becomes more uniform.

one. It is possible to obtain σ_y through the process of curve fitting after the calibration [54] [40] [55]. The same process can be extended to x and z directions, which are respectively the axial and lateral direction, to obtain σ_x and σ_z. All the three directions scatterers moving contributes to image signal decorrelation in blood flow imaging. Under the assumption of Gaussian shape of the point spread function, the correlation coefficient between B-mode $C_{Iflow}(n)$ frame can be written as:

$$C_{Iflow}(n) = e^{\left(\frac{-(vn\Delta t)^2}{2\sigma^2}\right)} = e^{\left(\frac{-(nD\Delta t)^2}{2}\right)} \tag{3.10}$$

where v is the overall velocity, Δt is the frame rate reciprocal, n is the frame rate number and D is the overall decorrelation value. The term D is related to the velocity v and the beam correlation width, as follows:

$$D = v/\sigma \tag{3.11}$$

As *BCW*, the decorrelation value D can be obtained by the curve fitting after calibration. By projecting 3.11 in the three dimension it is possible to measure the out-of-plane velocity as in the following equation [17] [18]:

$$D^2 = \frac{V_x^2}{\sigma_x^2} + \frac{V_y^2}{\sigma_y^2} + \frac{V_z^2}{\sigma_z^2} \tag{3.12}$$

Once measured the in-plane components and calculated the out-of-plane component, it is easy to find the overall velocity, as follows:

$$V^2 = V_x^2 + V_y^2 + V_z^2 \tag{3.13}$$

During the experiments the transducer has been positioned perpendicularly and in parallel to the axis of the vessel in order to obtain both the cross sectional and the longitudinal view respectively. It is good to remind that in the cross sectional, also known as transverse view, the majority of flow is in the out-of-plane direction, which means that the main component of the velocity is the out-of-plane one V_y. On the contrary, in the longitudinal view the majority blood flows in the axial direction, meaning that the main component is the one parallel to the axis of the vessel. The blood volume flow is finally calculated by integrating the overall velocity V in the luminal area of the vessel, as follows:

$$V' = \int v(r)dr \tag{3.14}$$

Since during the in vitro experiments a PVC tube with a constant inner diameter of 5 mm has been used, the equation 3.14 can be simplified, as follows:

$$V' = vA = v\pi\frac{d_{in}^2}{4} \tag{3.15}$$

3.2.2 Calibration

One of the key points for *SVD* method to be applied is the calibration of the beam correlation width σ in all directions. Figure 3.6 shows how calibration has been operated in this project.

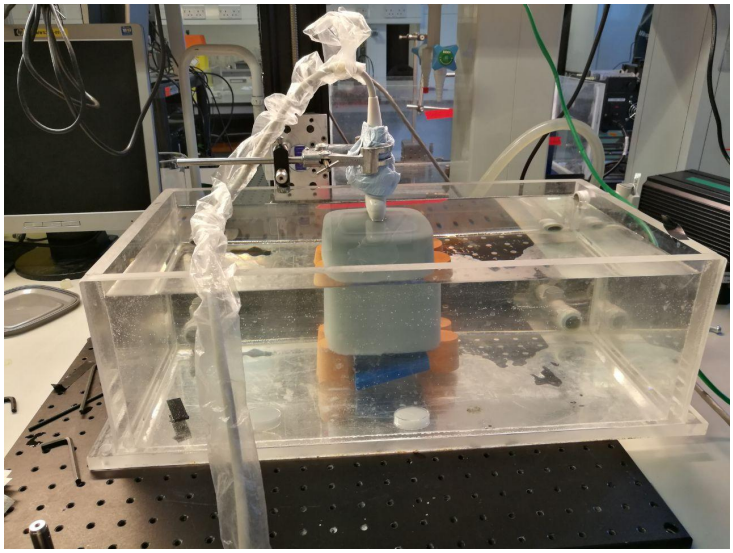

Descriptio 3.6: The transducer L11-4v is place on a speckle phantom for calibrating the probe. Beneath the phantom an absorber is deposited, in order to avoid the reflection from the bottom of the case.

The process consisted in placing the ultrasound transducer L11-4V on a speckle phantom and let the transducer move through the use of a moving clamp. In fig. 3.7 the position of the transducer has been set to allow the calibration on the elevational direction, i.e. the y-direction. Changing the position of the transducer allows the calibration in axial and lateral directions, which are respectively z-direction and x-direction. Hereafter, only the calibration of σ_y will be explained, since the calibration of σ_x and σ_z follows the same procedure. To calibrate the beam correlation width σ_y the ultrasound transducer is clamped to a 3-D motorized system and fixed perpendicular to the speckle phantom. The motorized system allows the transducer to move with a distance of 50 μm between two consecutive frames along the phantom. It has been chosen to obtain fifty B-mode image frames to calibrate the probe, which means that the covered distance in the elevational direction is 2.5 mm. To calibrate the transducer along the imaging depth it has been assumed that the plane-wave beam profile is constant in lateral directions. For the calibration of the decorrelation curve square patches of size 10×10 wavelengths were delineated for each depth. Thus, fifty patches come from fifty frames for each depth in the elevational direction. Figure 3.7 shows the patches for the i-frame.

All the patches contain the same number of pixels and for the calibration it is necessary to calculate the correlation coefficients between two consecutive patches at the same position, as follows:

$$C_I(i,j) = \frac{\sum_{k=1}^{N}(I_{i,k} - I_{i,mean})(I_{j,k} - (I_{j,mean})}{\sqrt{\sum_{k=1}^{N}(I_{i,k} - I_{i,mean})^2}\sqrt{\sum_{k=1}^{N}(I_{j,k} - I_{j,mean})^2}} \tag{3.16}$$

where i and j are the frame number, N is the number of pixels, $I_{j,k}$ and $I_{i,k}$ are the signal intensities of the pixel values and $I_{j,mean}$ and $I_{i,mean}$ are the mean intensity pixel values within the patch. In this project, to avoid the presence of noise in measuring the decorrelation a threshold of 0.6 has been used in the fitting of Gaussian curve [56]. To

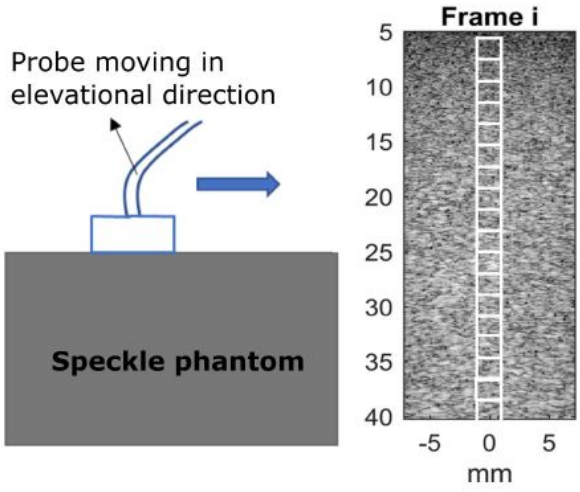

Descriptio 3.7: The transducer is moving along the elevational direction over a speckle phantom.

have a better calibration, the process was repeated three times and the average value was adopted. The σ_y values has then been fitted to a second-order polynomial. As already mentioned, σ_x and σ_z curves were obtained by following the same procedure for the in-plane directions, i.e. axial and lateral directions. One should know that calibration is a procedure specific to the sensor and imaging setting, meaning that if the parameters would change a new recalibration will be needed. Finally, a disk of known thickness made of the same composition of the speckle phantom has been used to measure the true speed of sound. In this project it has been assumed that the speed of sound through tissues is 1540 ms^{-1}, but the real value has been found to be 1472 ms^{-1}. For that reason, a correction factor of 1.046 has been used in the estimation of the overall velocity. Furthermore, it has been chosen the following values of voltage and pulse length:

- Voltage = 5 V, 10 V, 15 V
- Pulse Length = 1, 2, 4, 6

The calibration has been done by iteratively setting a combination of the values of Voltage and Pulse length. In particular, the Voltage values have been fixed and the Pulse lengths have been changed. In this way, all the possible combinations were obtained. The following figures provide the results of the calibration.

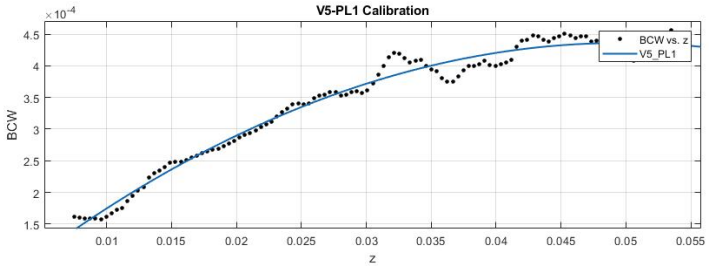

Descriptio 3.8: V=5V PL=1 calibration.

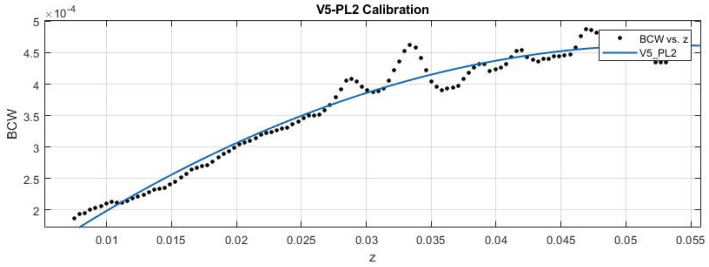

Descriptio 3.9: V=5V PL=2 calibration.

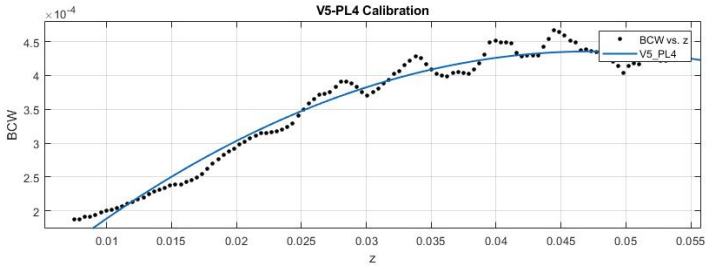

Descriptio 3.10: V=5V PL=4 calibration.

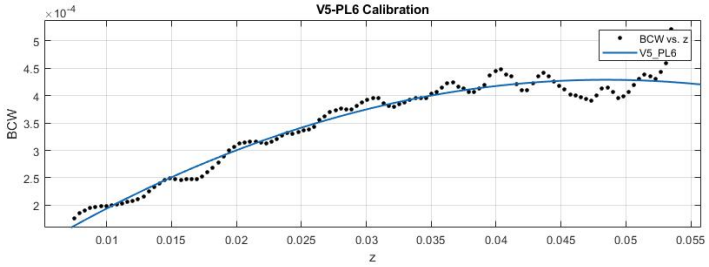

Descriptio 3.11: V=5V PL=6 calibration.

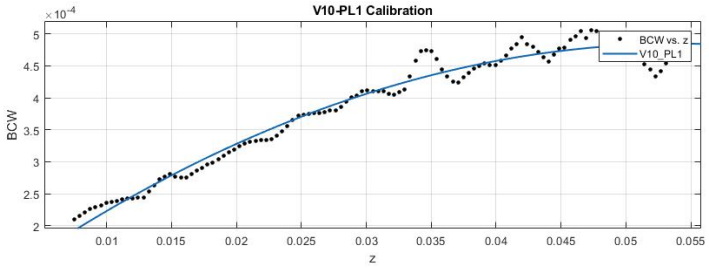

Descriptio 3.12: V=10V PL=1 calibration.

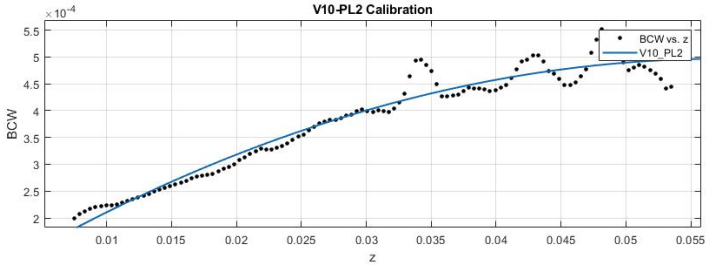

Descriptio 3.13: V=10V PL=2 calibration.

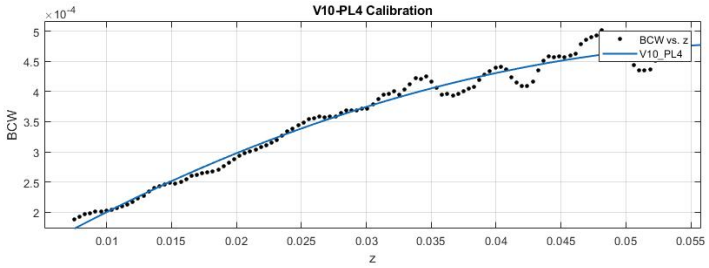

Descriptio 3.14: V=10V PL=4 calibration.

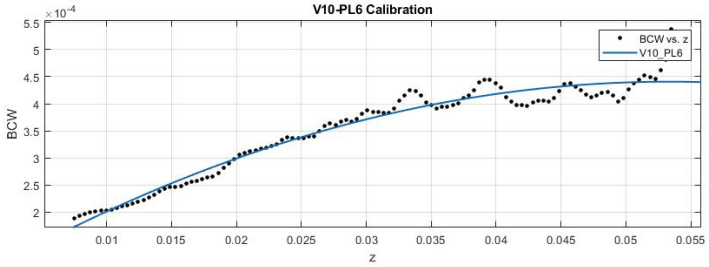

Descriptio 3.15: V=10V PL=6 calibration.

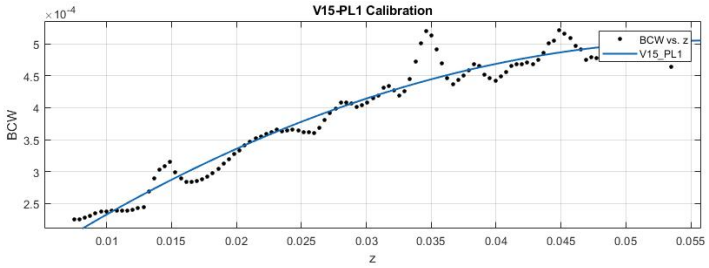

Descriptio 3.16: V=15V PL=1 calibration.

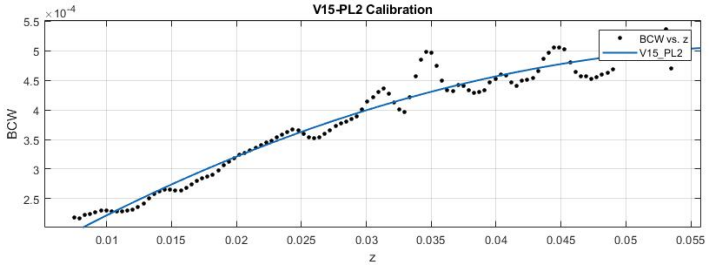

Descriptio 3.17: V=15V PL=2 calibration.

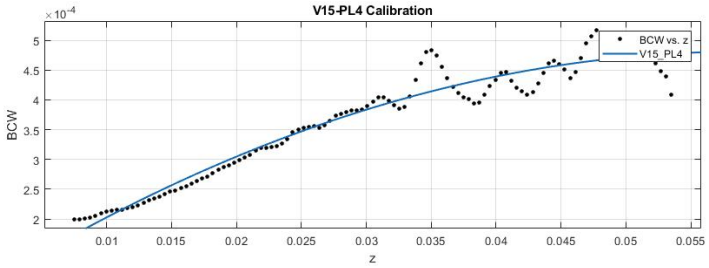

Descriptio 3.18: V=15V PL=4 calibration.

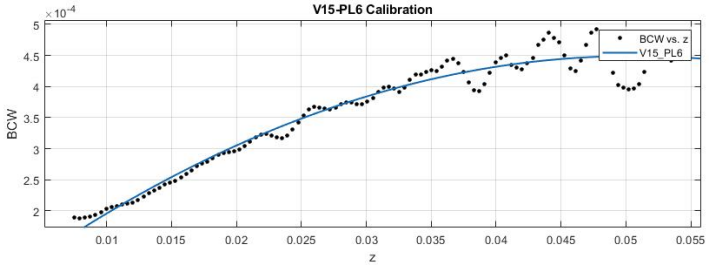

Descriptio 3.19: V=15V PL=6 calibration.

3.2.3 Velocity Limitations

Two main limitations of Speckle Decorrelation need to be considered. By taking care of these limitations it is possible to find the best set of parameters to obtain reasonable results.

The first restriction to point out is the value of the frame rate. Zhou et al. [57] demonstrated that the higher is the frame rate the better is the estimation of the out-of-plane velocity. On the other side, it is not possible to set a too high value of frame rate due to hardware limitations. The frame rate is indeed related to the number of acquired data, meaning that a high frame rate corresponds to a huge amount of acquired data, which requires more hardware memory. Thus, in this project the frame rate has been set equal to 10000. Another important factor to analyse is the impact of coherent compounding. It has been demonstrated that coherent compounding in plane-wave imaging is able to remarkably improve the spatial resolution of a B-mode image [58]. Nevertheless, it is not clear if it would affect the *SDC* method. In addition, a higher number of compounding planes would penalise the computational performances. This means that for a higher number of compounding planes a lower number of frame rate is necessary to guarantee the hardware stability. For this reasons, it has been fixed the number of compounding planes equal to one. In this way the quality of resulting acquired images is slightly worse, but on the other side it is possible to chose a frame-rate sufficient to ensure good *SDC* performances. In addition to these two issues, it is good to mention that red blood cells generate weak signals when they are hit by ultrasounds. This could be a problem for *SDC* method to work, but as analysed in paragraph 3.1, it has been used the Singular Value Decomposition Filtering to enhance blood signal.

3.3 Velocity Estimator in Presence of Reverse Flow

In cardiovascular system, blood could flow in both the two directions, generating the so-called reverse flow. This behaviour comes from many factors, such as pulsing heart action and geometry features. In some cases, the presence of a huge reverse flow is consequence of pathological conditions [59] [60] [12]. The traditional *SDC* method is not able to give a good estimation of blood flow velocity when reverse flow occurs. In this chapter a modified *SDC* method, capable to overcome this problem, will be discussed.

3.3.1 Materials and Methods

Traditional Speckle Decorrelation Method is not able to discern blood flow directions in vessels. Thus, it can only measure velocity value through vessels but not the direction. This can lead to the overestimation of blood flow speed, especially when the flow is bidirectional. Zhou et al. [61] proposed a new approach, through which *SVD* method is able to detect out-of-plane velocity taking into consideration the direction of flow. The basic concept to implement this method is to rotate the transducer in order to obtain a tilted angle between the vessel radius and the scanning plane. As a consequence, it is possible to differentiate the through-plane flow by assuming that the primary blood flow, which is the blood flowing in the main direction, moves along the longitudinal direction. Figure 3.20 illustrates well how the relative position between the transducer and the vessel radius influences the detection of reverse flow.

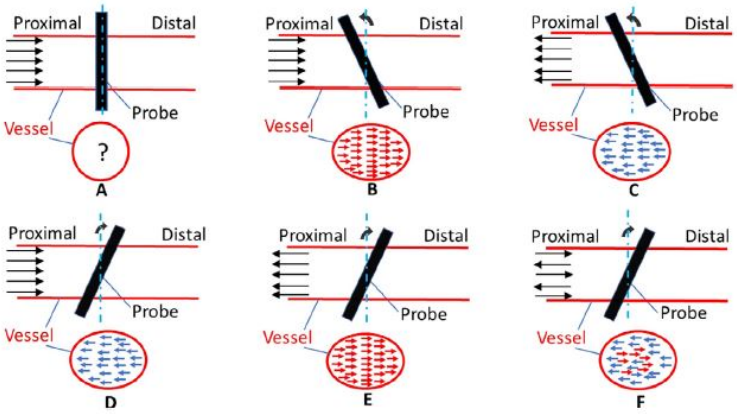

Descriptio 3.20: Illustration of the ultrasound scanning strategy in the Speckle Decorrelation Method with the presence of reverse flow.

In Fig. 2a the transducer is placed perpendicular to the vessel axis and generates a transversal view of the vessel, as one can notice in the lower part. In this configuration the *SDC* method can only detect the speed of flow in the scanning plane but not the direction. This could potentially lead to errors in the detection of volumetric flow. In figures 2b-2f the transducer is rotated by a tilted angle and, therefore, the cross section of the vessel is an ellipse and not a circle. In this way, the through-plane flow direction can be distinguished from its corresponding in-plane flow direction. To further improve this approach, for each angle the resulting value is the average of clockwise and anticlockwise tilted angles. Another advantage of this method is that the value of the results, whether it is positive or negative, is independent of which direction the probe is tilted. The through-plane velocity is seen as negative when the corresponding in-plane flow moves to the left, vice versa it is positive when it flows to the right. Nevertheless, if the resulting blood flow velocity turns out to be negative, its absolute value will be used to measure the volume flow.

Caput 4

Analysis of the Performances

In this chapter the results of all the steps necessary to achieve the aim of this master thesis project will be presented. In the first section some results about the application of different thresholds in SVD filtering will be displayed and discussed. In the second and third sections the dependence of the values of voltage and pulse length will be discussed. In the last part all the statistical results will be examined.

4.1 SVD - Thresholds Dependence

As described in section 3.1 the goodness of Singular Value Decomposition filtering depends on the values of the threshold. In this project an adaptive double threshold method has been adopted. Using two thresholds allows to remove both tissue and noise from blood, which increases blood signal. In order to choose the right values of the two thresholds the boundaries between the three regions of the correlation matrix were analysed. Since the boundaries of the correlation matrix were not well defined, several trials to find the good thresholds were performed. Furthermore, to reduce the number of trials the plotted singular values λ have been analysed. Thus, firstly a possible couple of thresholds were selected form the correlation matrix, then a double check on the plot of the singular values was carried out. Fig 4.1 provides an example of the correlation matrix obtained from the data acquired with the set of parameters having the lower values, i.e. V=5V and PL=1.

As one can notice, it is not easy to find a clear boundary between the tissue region and blood region and between the blood region and the noise. As a matter of fact, fig. 4.2 which shows the singular values of matrix Δ supports the operator in the choice of the thresholds.

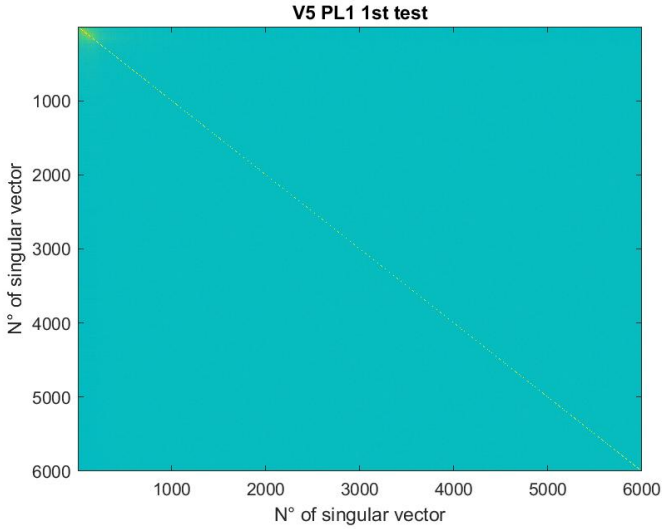

Descriptio 4.1: Correlation coefficient matrix of the first test performed with V=5V and PL=1.

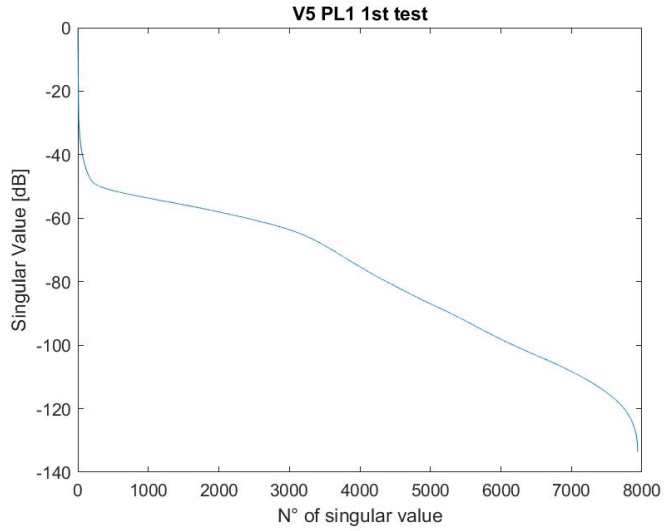

Descriptio 4.2: Plot of the singular values λ of the first test performed with V=5V and PL=1.

One of the key points of this master thesis project consists in applying in a proper way the singular value decomposition filtering. A not suitable determination of the thresholds can lead to bad images, both in terms of signal-to-noise ratio and in removing the tissue echo from the blood signal. In addition, if the images were not filtered well, the speckle decorrelation method would give an inaccurate estimation of the out-of-plane velocity components. Fig 4.3 illustrates how different thresholds provide different filtered images.

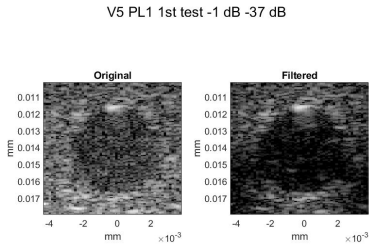

(a) thr1 = -1dB and thr2 = -37dB

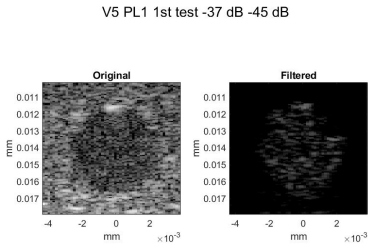

(b) thr1=-37dB and thr2=-45dB

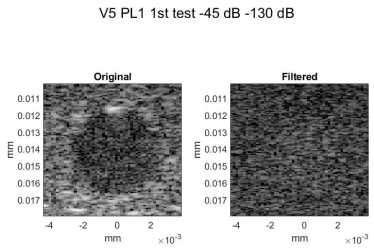

(c) thr1=-45dB and thr2=-130dB

Descriptio 4.3: The difference between SVD filtering with three different couples of thresholds.

As one can clearly notice, the best results are obtained in figure 4.3b. Thus, in this project the thresholds selected are -37 dB for the tissue removal and -45 dB for denoising. These values were defined in relation to the energy of the correlation coefficient. The energy has been evaluated as follows:

$$Energy = 20 \log_{10} \left(\frac{diag(\Delta)}{max(diag(\Delta))} \right) \tag{4.1}$$

where Δ is the non-square diagonal matrix obtained through the SVD method. The indexes of columns, where the values of energy corresponded to the values of the two thresholds, are then used to remove the tissue from the blood signal, as explained in section 3.1.

4.2 Voltage Dependence

It has been proved that the influence of different values of voltage affects the quality of image. The transducer used, i.e. $L11-4v$, can work within the range of 1V - 20V. In this project three values of voltage, which are V=5V, V=10V and V=15V, have been analysed. As described in section 2.1.3, the ultrasound waves are generated by the piezoelectric elements of the transducer. They convert the electrical energy absorbed into the mechanical energy to generate the ultrasound waves. As a consequence, the higher is the voltage the higher is the mechanical energy generated by the transducer. In terms of image quality, a higher voltage reflects into a better signal-to-noise ratio. Fig 4.4 shows the comparison

between three images at a fixed pulse length (PL=1) and at different voltage (V=5V - 10V - 15V).

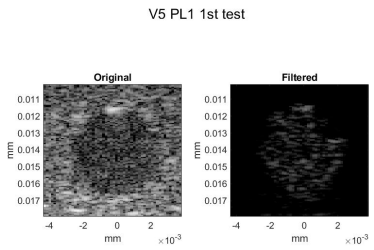

(a) V=5V PL=1

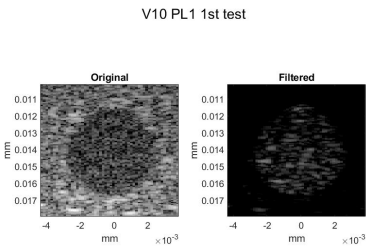

(b) V=10V PL=1

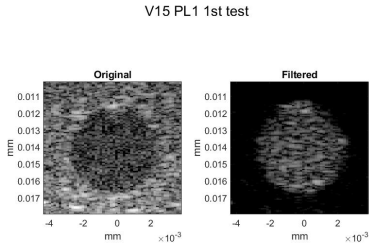

(c) V=15V PL=1

Descriptio 4.4: The difference between SVD filtering with three different values of voltage.

It is important to point out that Verasonics system is not linear in voltage, meaning that the correlation between the value of voltage and the signal-to-noise ratio is not linear. Despite this little issue, the difference in terms of SNR between the three images in fig. 4.4 is easily visible. Even though voltage influences the quality of images, in this project it has been demonstrated that it slightly impacts on the speckle decorrelation method. This outcome will be further investigated in section 4.4.

4.3 Pulse Length Dependence

Pulse length is the other parameter that affects the results in this project. It is defined as the distance that the pulse occupies in space, from the beginning of one pulse till the end of that same pulse. In other words, it represents the length of the cycles in the pulse. Fig. 4.5 shows the pulse transmitted by the L11-4v probe.

To have a good pulse, meaning that is has a Gaussian sinusoidal shape, the transmitting frequency of the transducer has been set at 7.2 MHz. Having a nice pulse is fundamental for the transducer to receive the correct value of pulse length. Differently from the voltage, the pulse length gives a relevant contribution both to the image quality and to the speckle decorrelation. In terms of image quality, it has been proved that a higher pulse length corresponds to a higher signal-to-noise ratio. On the other side, high values of pulse length worsen the spatial resolution of the images. In this master thesis project, the effect of four different values of pulse length, which are PL=1, PL=2, PL=4

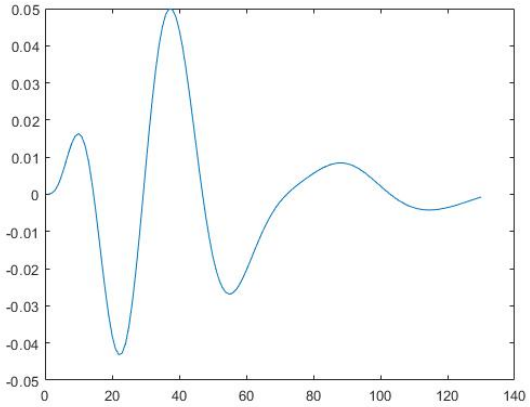

Descriptio 4.5: Real pulse transmitted by Verasonics probe L11-4v.

and PL=6, have been analysed. Fig. 4.6 provides a visual example of how the pulse length affects the image quality.

As for the results obtained with several values of voltage, one can notice that the theoretical aspects of the pulse length dependence are slightly different from the practical results. Indeed, since the pulse is not ideal, meaning that it could have some edges, the Verasonics system does an equalization to compensate the edge of the signal.

In terms of speckle decorrelation, the results achieved show that for higher values of pulse length the estimated velocity is slightly far from the ground-truth. Vice versa, speckle decorrelation performs very well in presence of low values of pulse length. These results will be discussed in the following section.

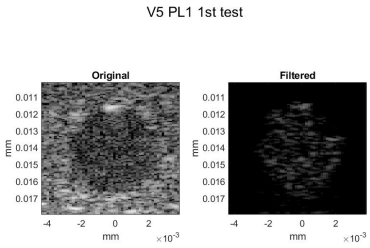

(a) V=5V PL=1

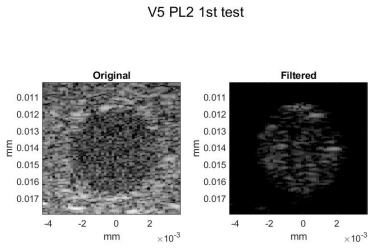

(b) V=5V PL=2

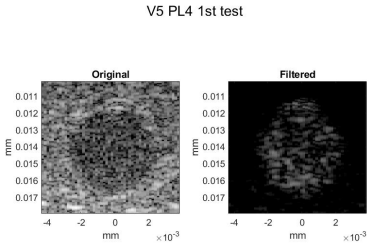

(c) V=5V PL=4

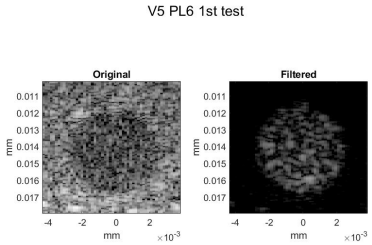

(d) V=5V PL=6

Descriptio 4.6: The difference between SVD filtering with four different values of pulse length.

4.4 Results

All the acquisitions were performed three times for each couple of parameters in order both to have statistical relevance and to ensure the accuracy of data. As described in previous paragraphs, speckle decorrelation and image quality depend both on the values of voltage and pulse length. Therefore, in this section the impact of different combinations of voltage and pulse lengths will be presented and discussed.

In this master thesis project, the values of voltage have been chosen, as follows:

- V = 5V - 10V - 15V

and the values of pulse length have been set, as follows:

- PL = 1 - 2 - 4 - 6

4.4.1 Singular Value Decomposition Filtering

All the results obtained by applying the Singular Value Decomposition filtering to the acquired data for each combination of voltage and pulse length and for each trial will be shown below.

From a theoretical point of view the increasing voltage and pulse lengths correspond to a higher signal-to-noise ratio. The obtained results generally follow this tendency, though some images are slightly different form the expected outcomes. This can find a possible answer by analysing the Verasoincs system. In particular, the system used in this master thesis project is not linear in voltage. In addition to this, the values of pulse length set in Verasonics system do not correspond to the number of cycles of the pulse, but they correspond to the number of half-cycles. In other words, a pulse length equal to 4 is seen by the system as only 2 cycles. Thus, compensate the edge of the signal, the Verasonics system does an equalization. Despite the non-linearity in voltage and the equalization of the system, the achieved results provide a good trend, similar to what theoretical aspects expected.

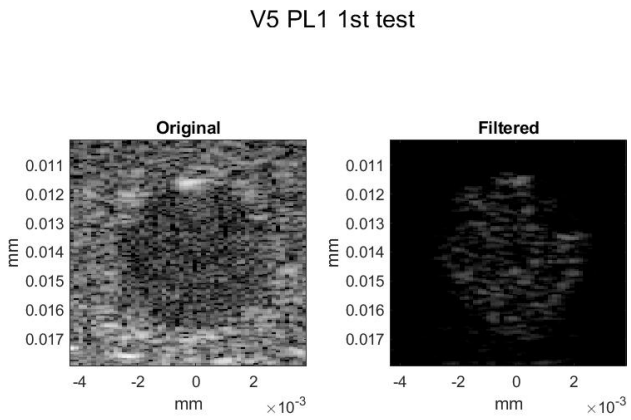

(a) V=5V PL=1 SVD 1st test

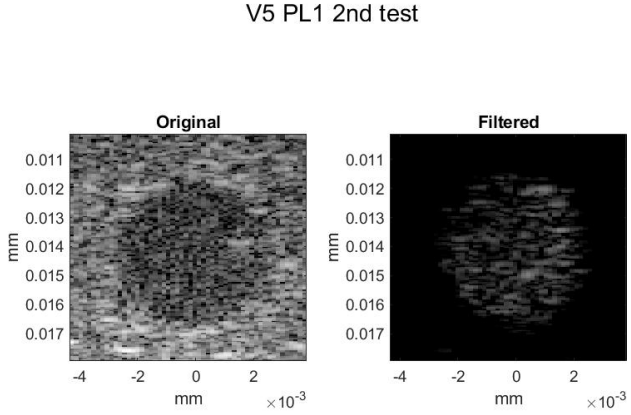

(b) V=5V PL=1 SVD 2nd test

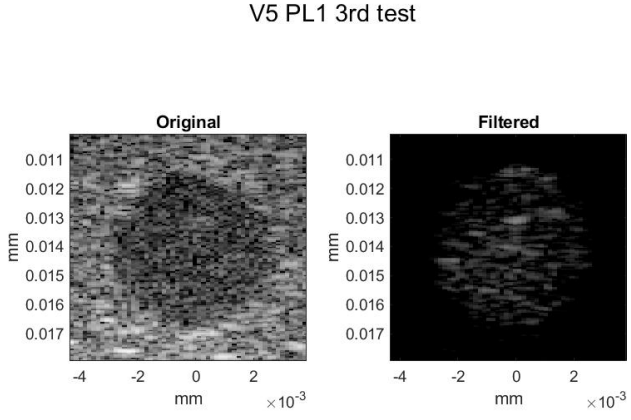

(c) V=5V PL=1 SVD 3rd test

Descriptio 4.7: SVD filtering results for V=5V and PL=1.

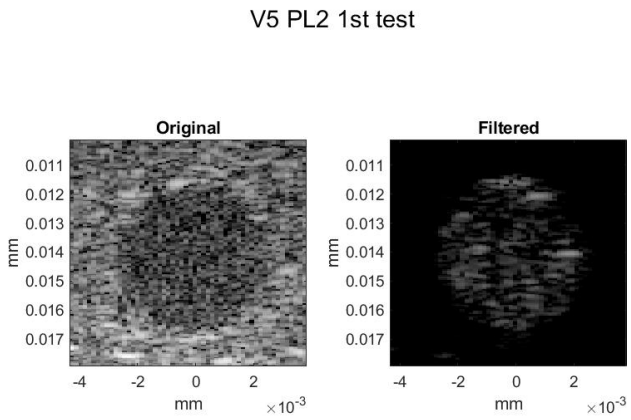

(a) V=5V PL=2 SVD 1st test

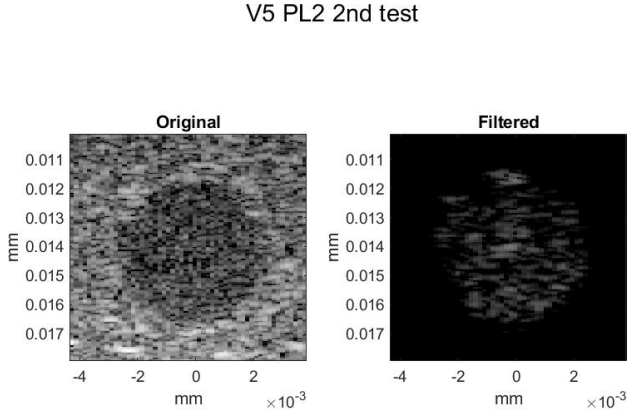

(b) V=5V PL=2 SVD 2nd test

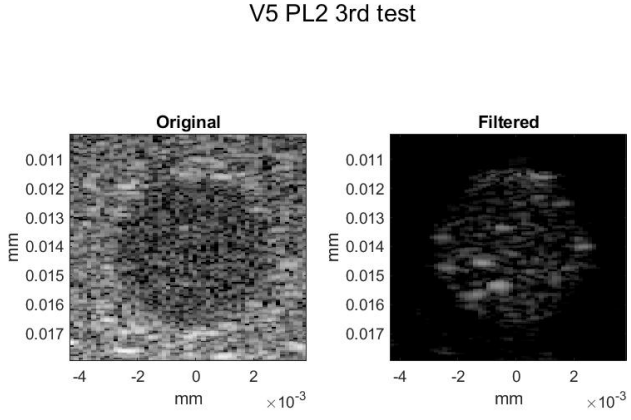

(c) V=5V PL=2 SVD 3rd test

Descriptio 4.8: SVD filtering results for V=5V and PL=2.

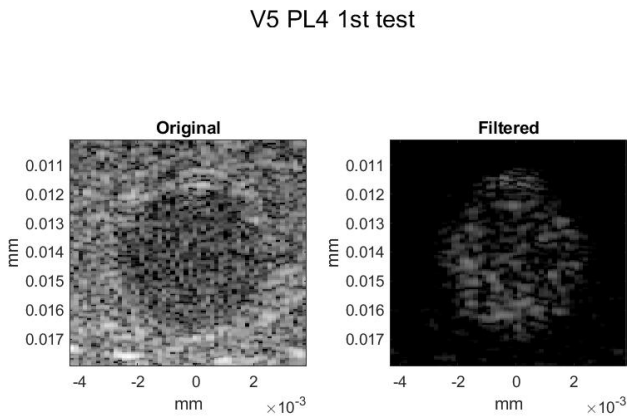

(a) V=5V PL=4 SVD 1st test

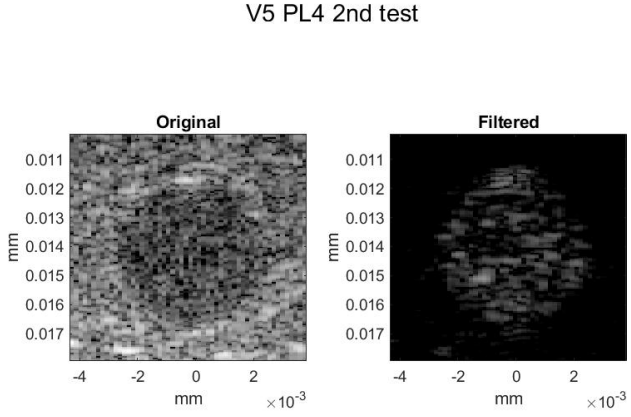

(b) V=5V PL=4 SVD 2nd test

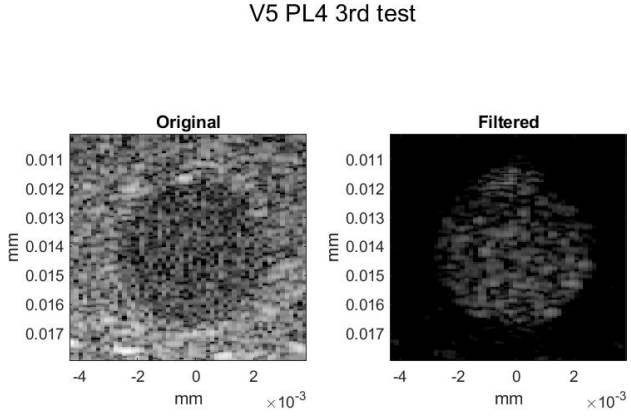

(c) V=5V PL=4 SVD 3rd test

Descriptio 4.9: SVD filtering results for V=5V and PL=4.

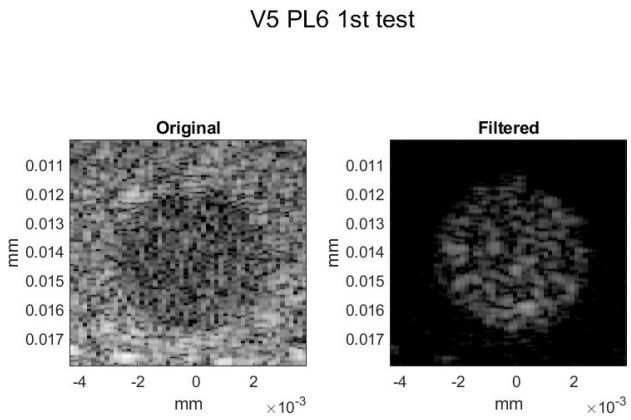

(a) V=5V PL=6 SVD 1st test

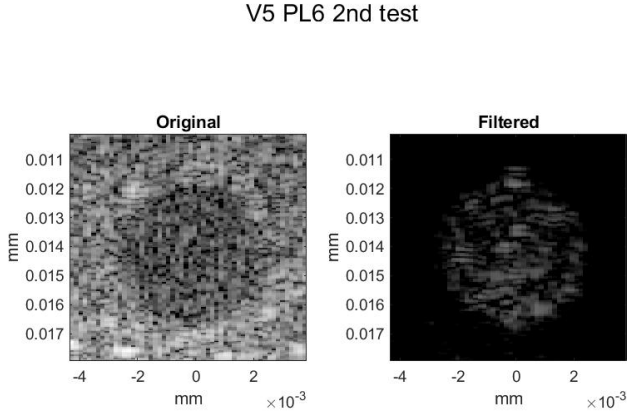

(b) V=5V PL=6 SVD 2nd test

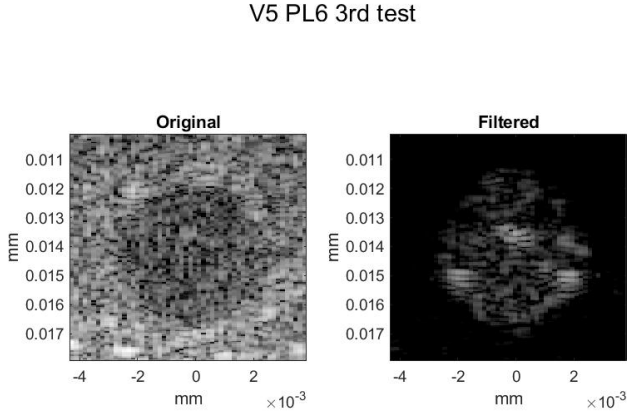

(c) V=5V PL=6 SVD 3rd test

Descriptio 4.10: SVD filtering results for V=5V and PL=6.

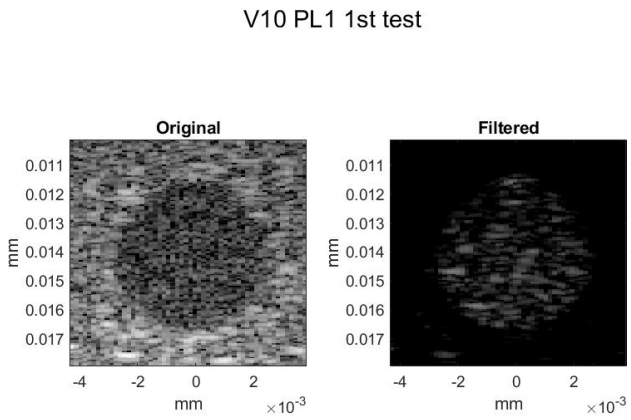

(a) V=10V PL=1 SVD 1st test

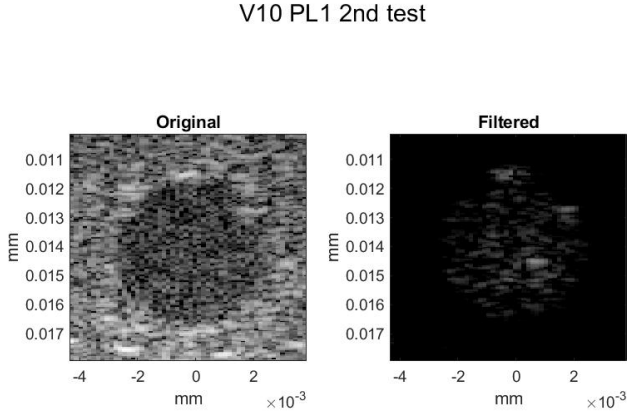

(b) V=10V PL=1 SVD 2nd test

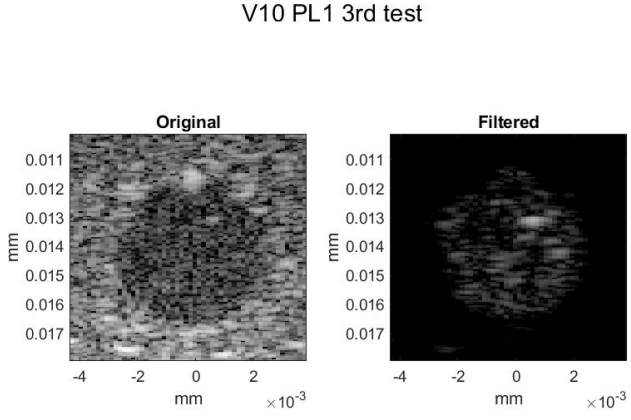

(c) V=10V PL=1 SVD 3rd test

Descriptio 4.11: SVD filtering results for V=10V and PL=1.

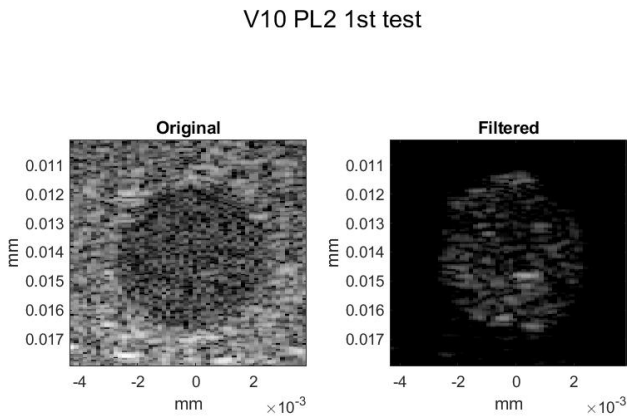

(a) V=10V PL=2 SVD 1st test

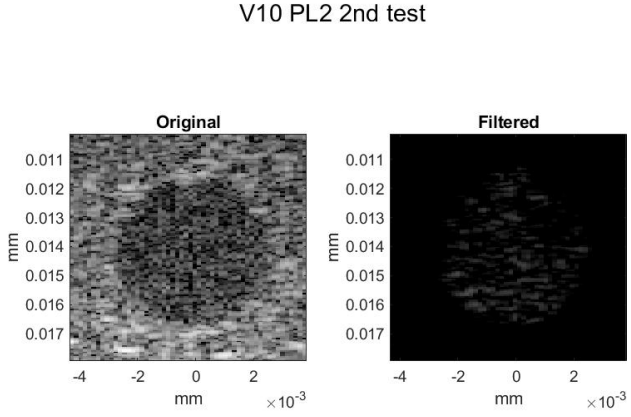

(b) V=10V PL=2 SVD 2nd test

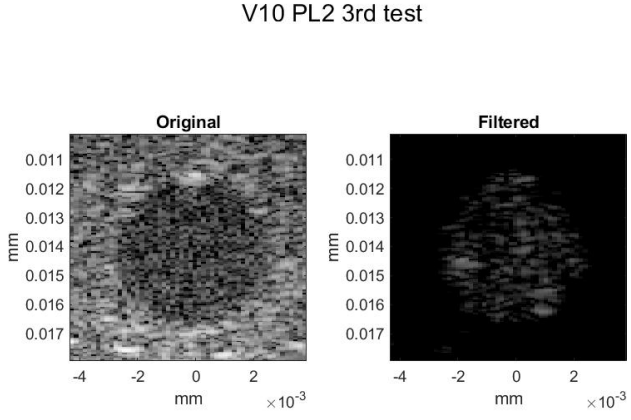

(c) V=10V PL=2 SVD 3rd test

Descriptio 4.12: SVD filtering results for V=10V and PL=2.

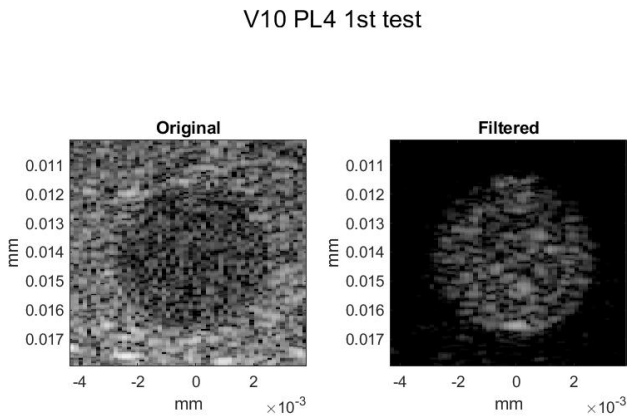

(a) V=10V PL=4 SVD 1st test

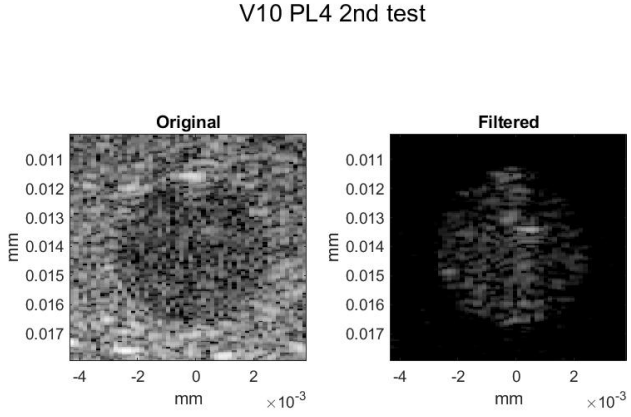

(b) V=10V PL=4 SVD 2nd test

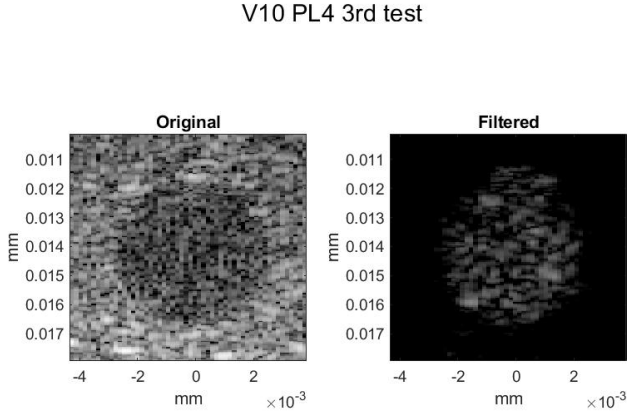

(c) V=10V PL=4 SVD 3rd test

Descriptio 4.13: SVD filtering results for V=10V and PL=4.

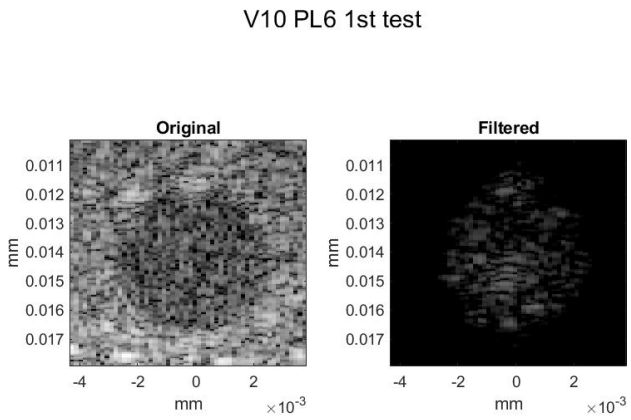

(a) V=10V PL=6 SVD 1st test

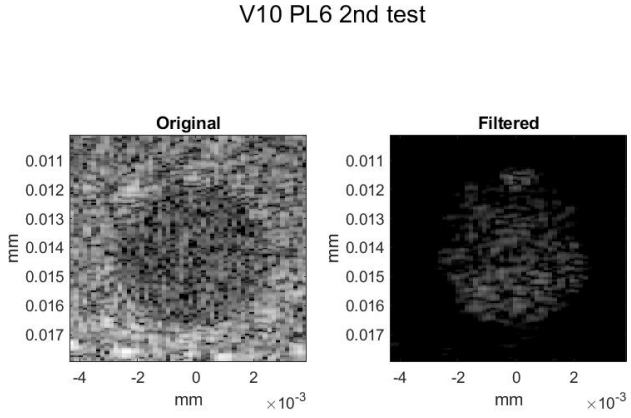

(b) V=10V PL=6 SVD 2nd test

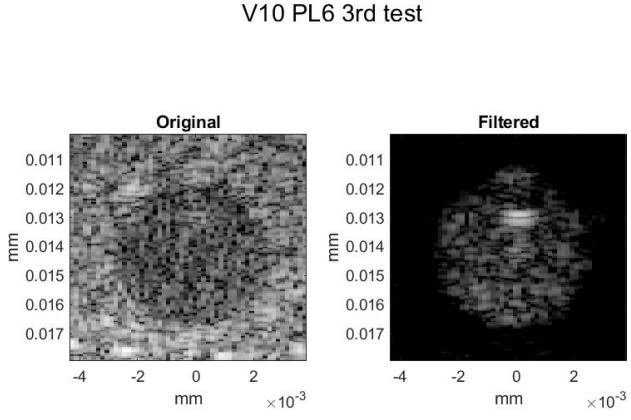

(c) V=10V PL=6 SVD 3rd test

Descriptio 4.14: SVD filtering results for V=10V and PL=6.

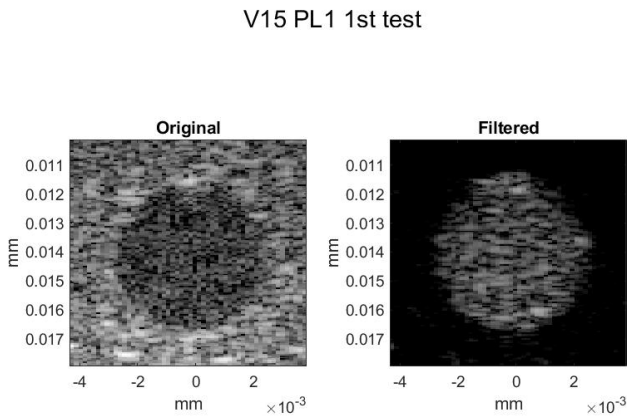

(a) V=15V PL=1 SVD 1st test

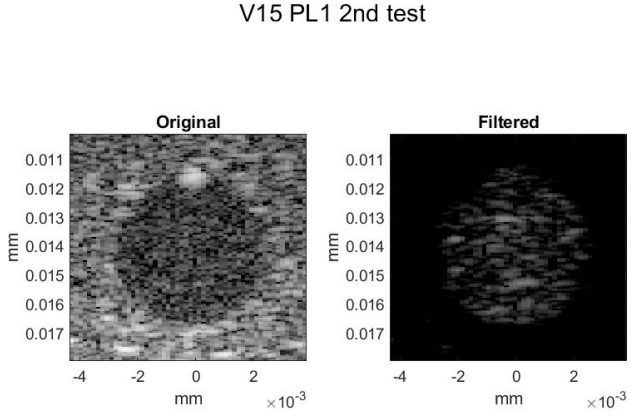

(b) V=15V PL=1 SVD 2nd test

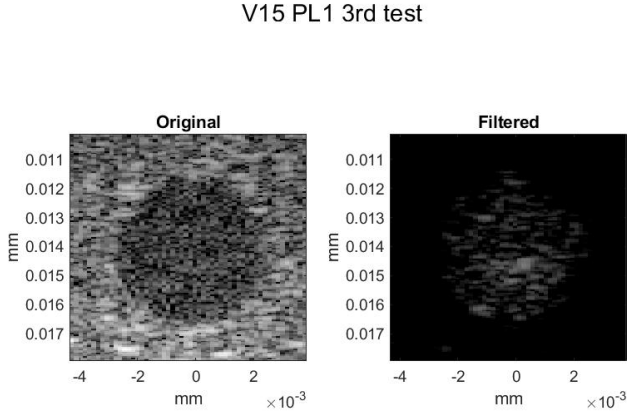

(c) V=15V PL=1 SVD 3rd test

Descriptio 4.15: SVD filtering results for V=15V and PL=1.

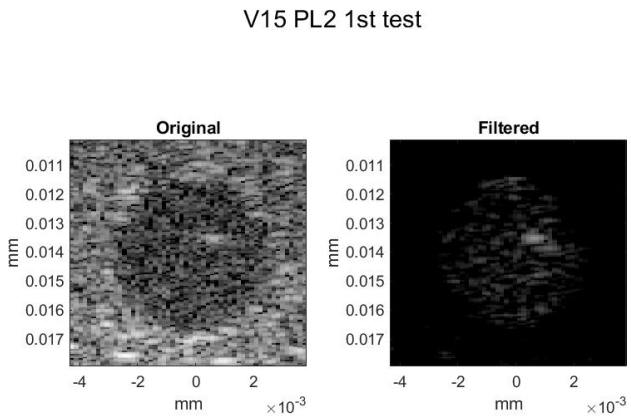

(a) V=15V PL=2 SVD 1st test

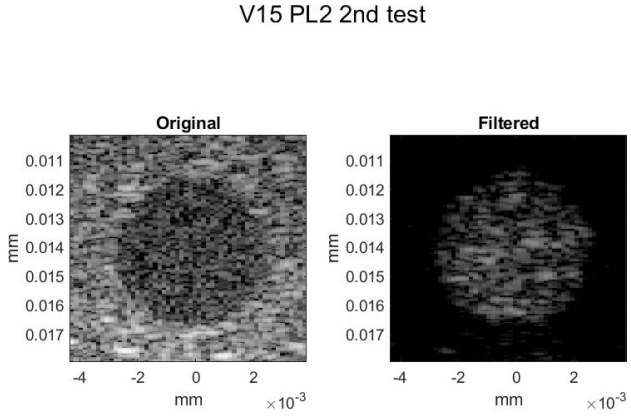

(b) V=15V PL=2 SVD 2nd test

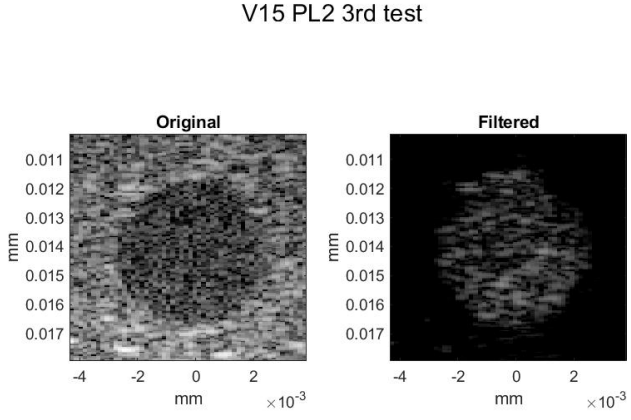

(c) V=15V PL=2 SVD 3rd test

Descriptio 4.16: SVD filtering results for V=15V and PL=12.

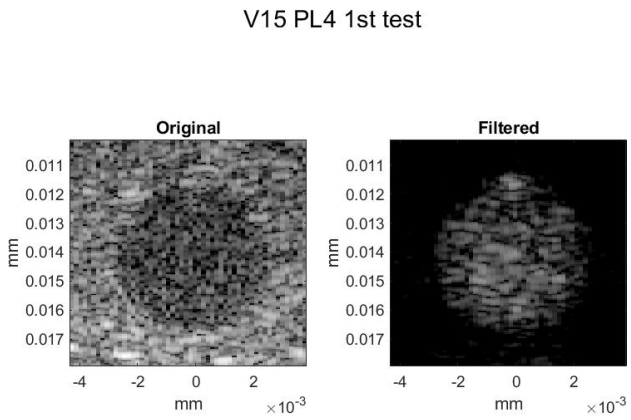

(a) V=15V PL=4 SVD 1st test

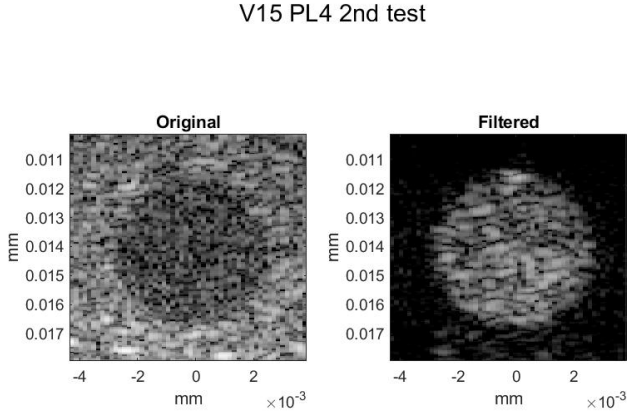

(b) V=15V PL=4 SVD 2nd test

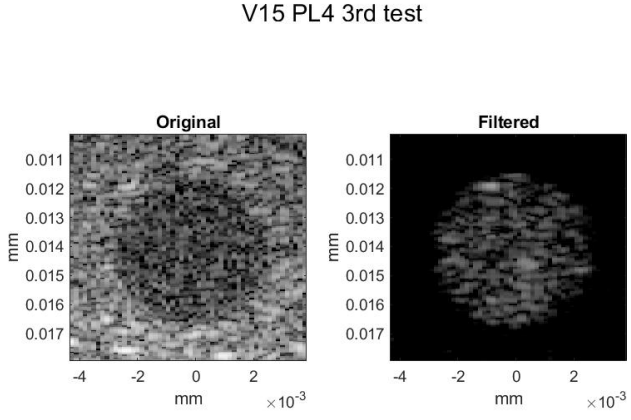

(c) V=15V PL=4 SVD 3rd test

Descriptio 4.17: SVD filtering results for V=15V and PL=4.

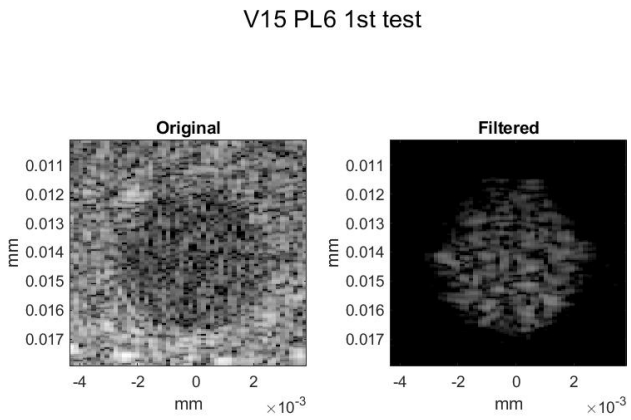

(a) V=15V PL=6 SVD 1st test

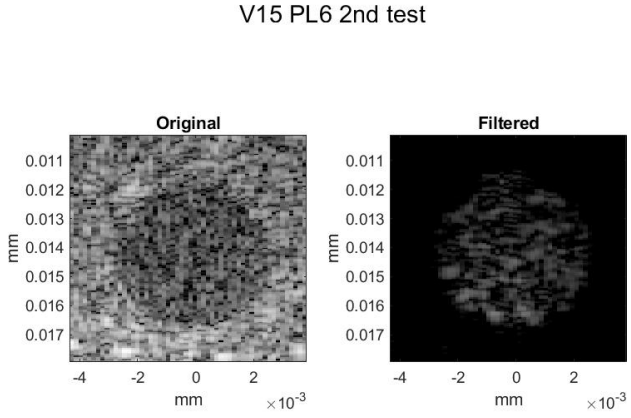

(b) V=15V PL=6 SVD 2nd test

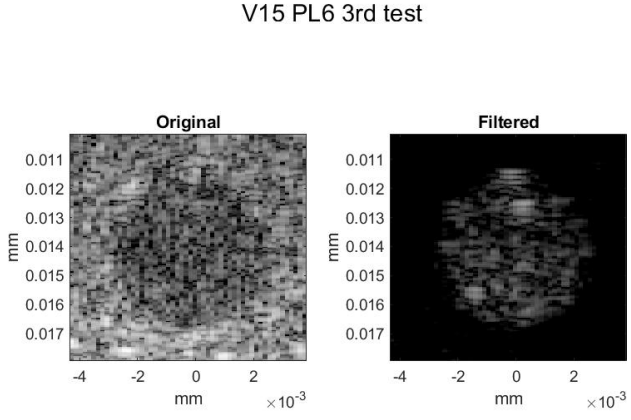

(c) V=15V PL=6 SVD 3rd test

Descriptio 4.18: SVD filtering results for V=15V and PL=6.

4.4.2 Speckle Decorrelation Method

In this section all the results achieved by applying the speckle decorrelation method to the filtered data will be presented. Each figure represents the out-of-plane mean velocity. It is important to highlight that during the acquisition, the pulsatile pump was set at 80 strokes/min. For this reason, each dataset has been acquired for two seconds, in order to obtain a complete velocity profile.

As one can notice, the trend of the out-of-plane mean velocity is generally the same for each combination of parameters and for each trial. Fig. 4.21b) represents an outlier, since its velocity profile do not match well with the others. This outlier probably comes from pump failure or operator's inattention during the data acquisition.

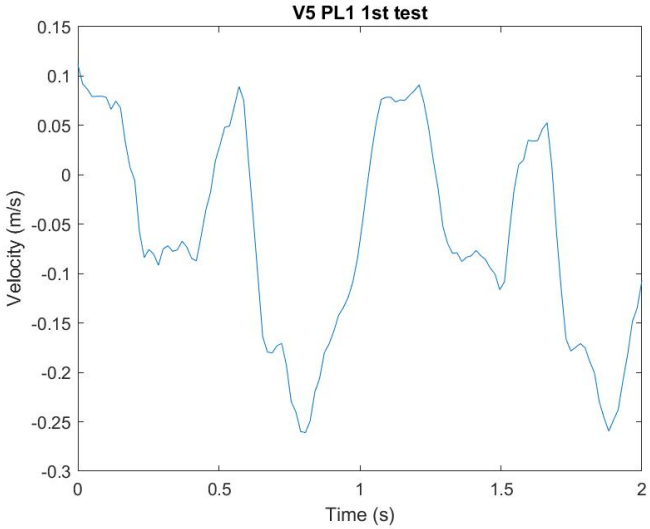

(a) V=5V PL=1 SDC 1st test

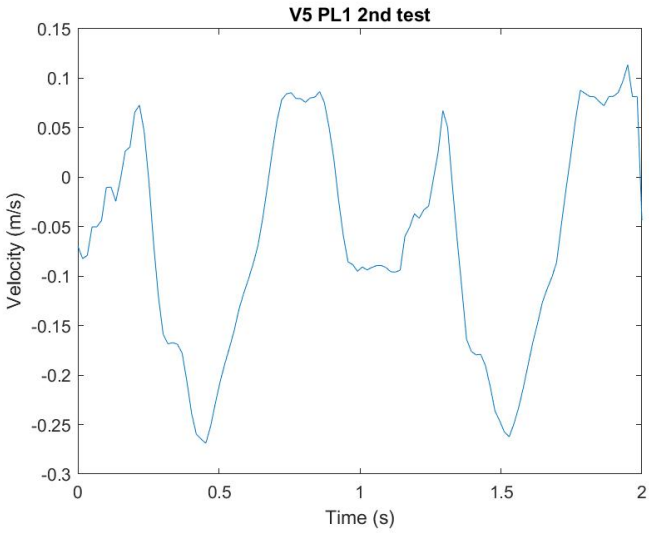

(b) V=5V PL=1 SDC 2nd test

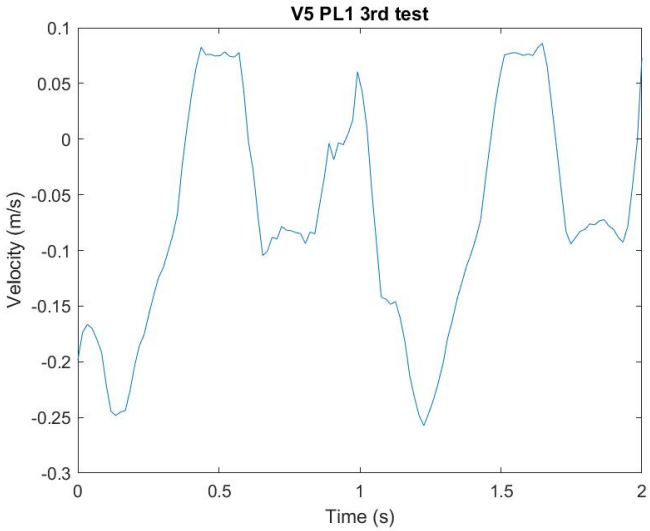

(c) V=5V PL=1 SDC 3rd test

Descriptio 4.19: SDC results for V=5V and PL=1.

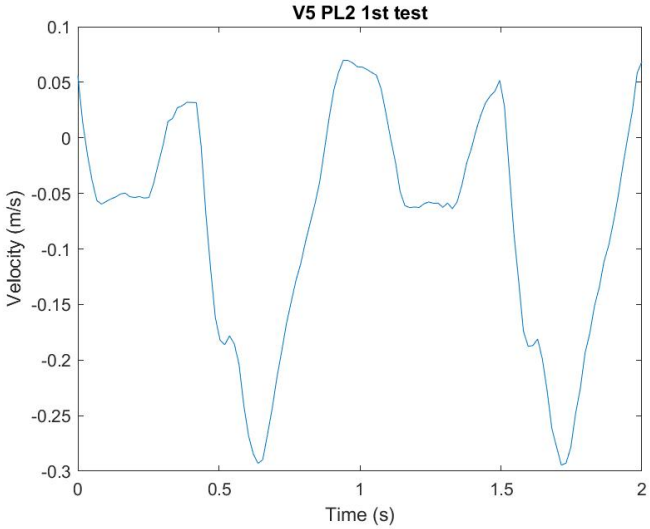

(a) V=5V PL=2 SDC 1st test

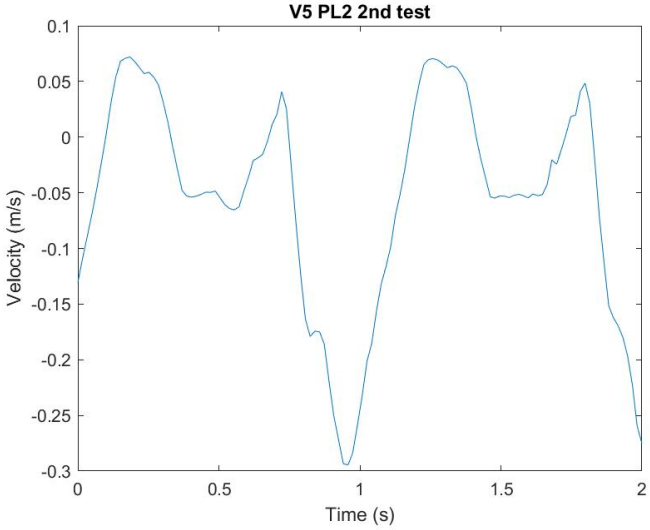

(b) V=5V PL=2 SDC 2nd test

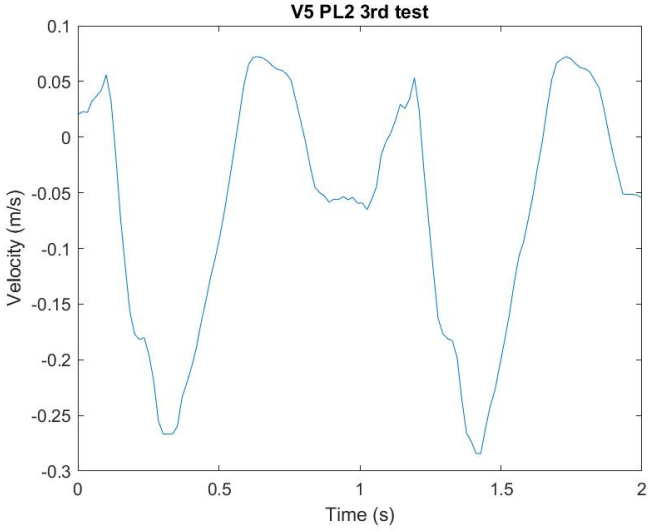

(c) V=5V PL=2 SDC 3rd test

Descriptio 4.20: SDC results for V=5V and PL=2.

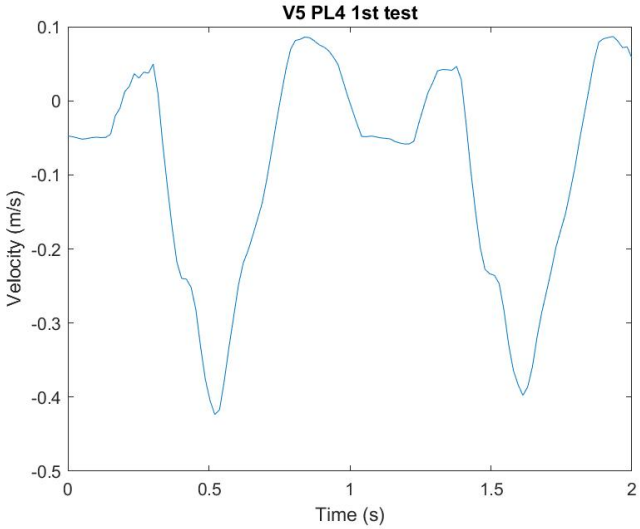

(a) V=5V PL=4 SDC 1st test

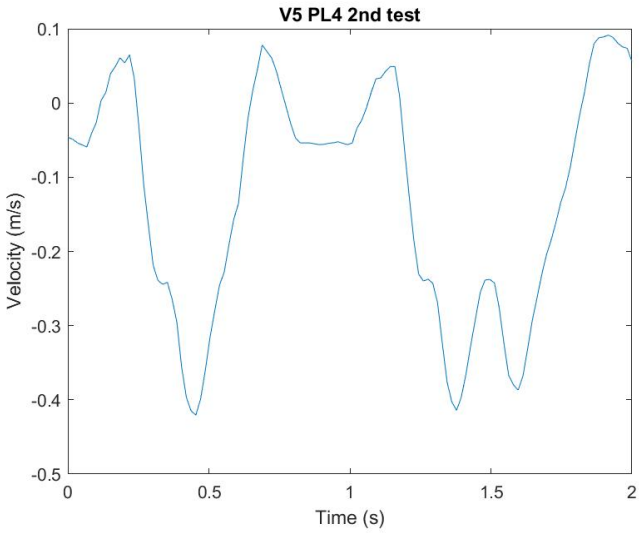

(b) V=5V PL=4 SDC 2nd test

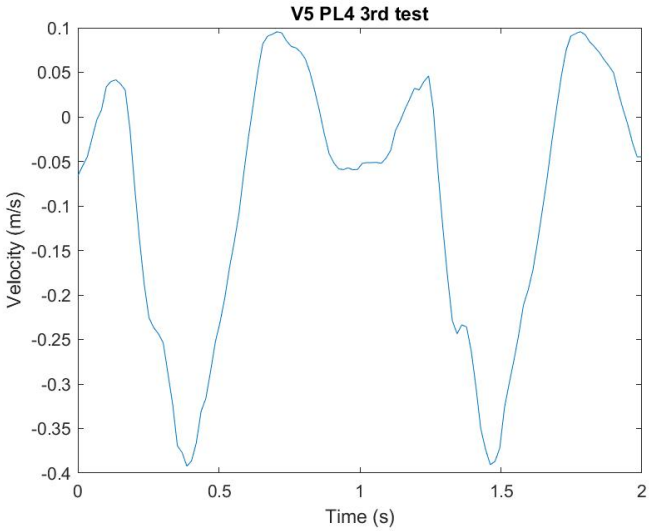

(c) V=5V PL=4 SDC 3rd test

Descriptio 4.21: SDC results for V=5V and PL=4.

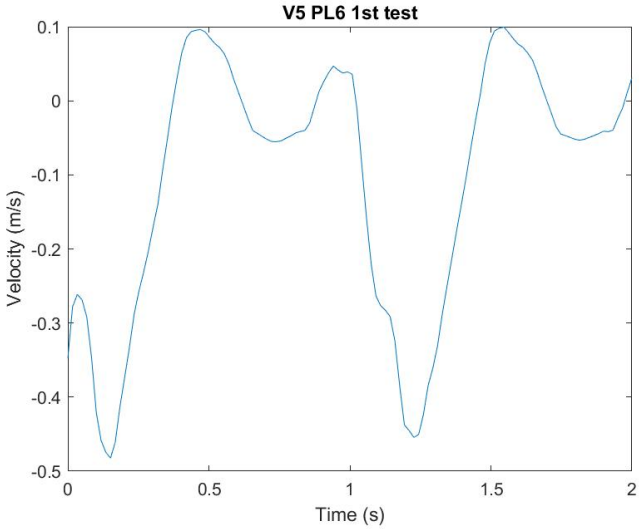

(a) V=5V PL=6 SDC 1st test

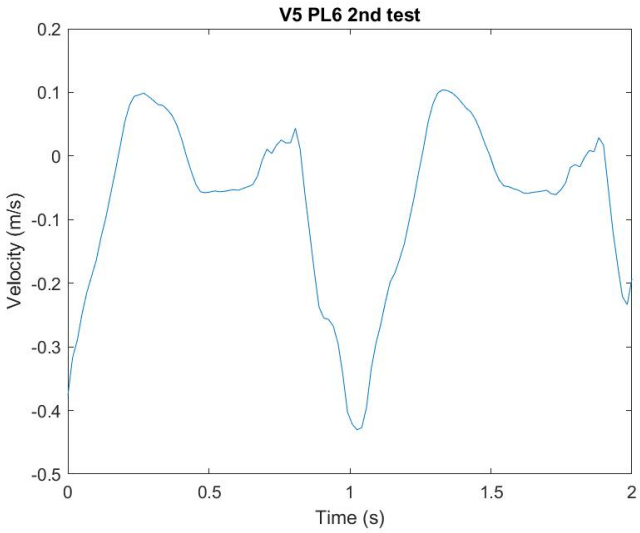

(b) V=5V PL=6 SDC 2nd test

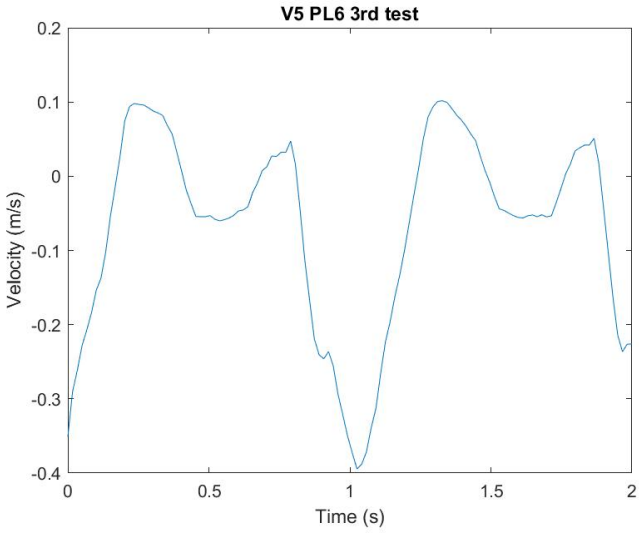

(c) V=5V PL=6 SDC 3rd test

Descriptio 4.22: SDC results for V=5V and PL=6.

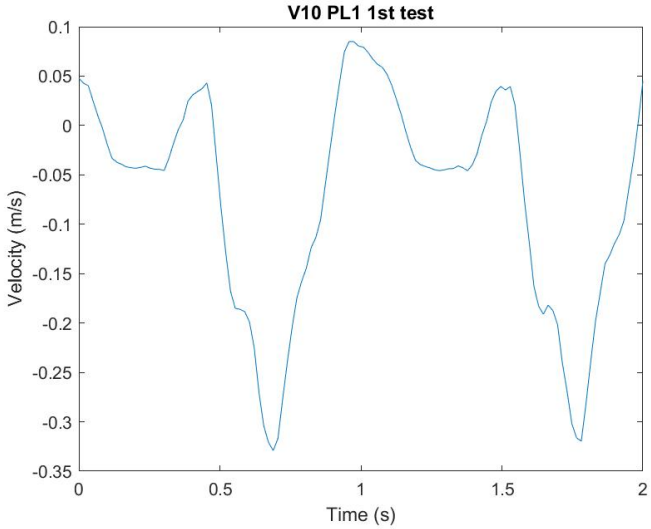

(a) V=10V PL=1 SDC 1st test

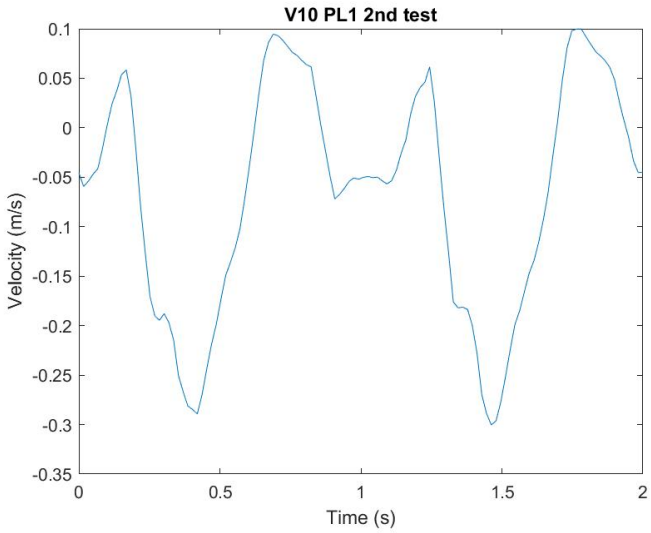

(b) V=10V PL=1 SDC 2nd test

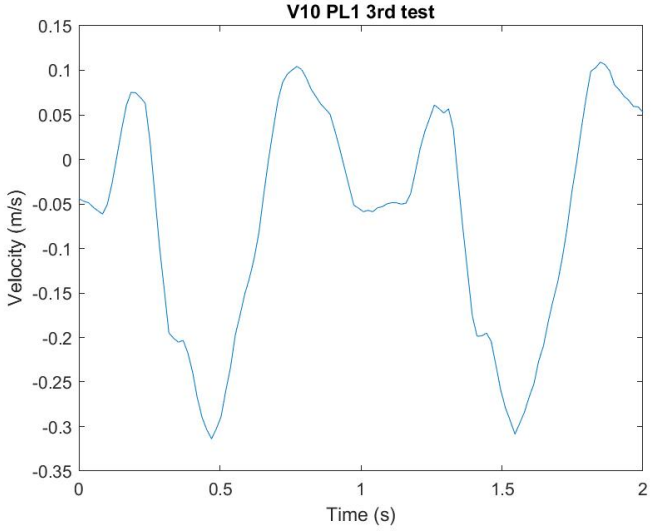

(c) V=10V PL=1 SDC 3rd test

Descriptio 4.23: SDC results for V=10V and PL=1.

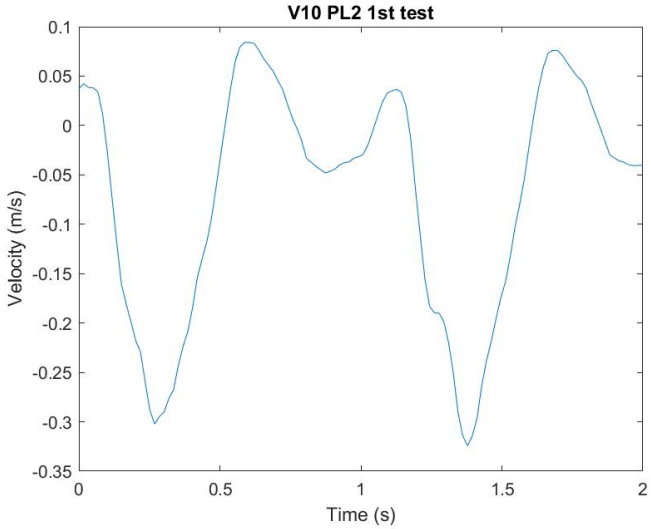

(a) V=10V PL=2 SDC 1st test

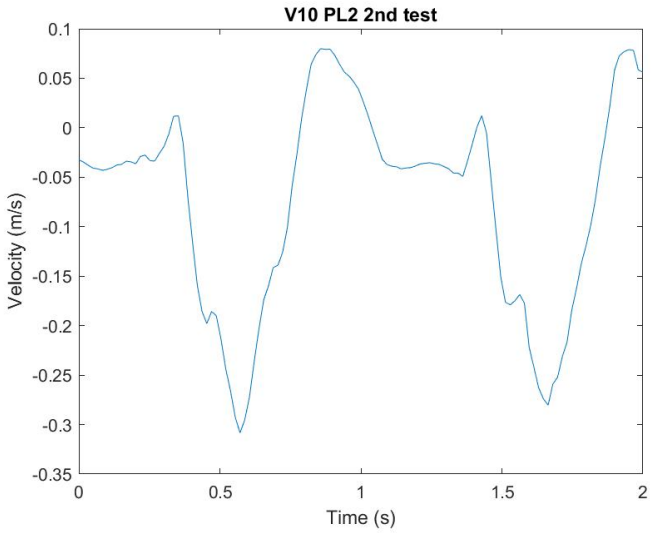

(b) V=10V PL=2 SDC 2nd test

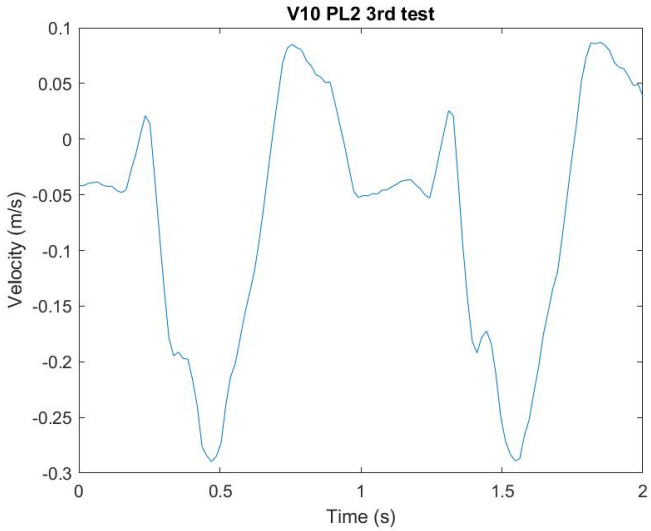

(c) V=10V PL=2 SDC 3rd test

Descriptio 4.24: SDC results for V=10V and PL=2.

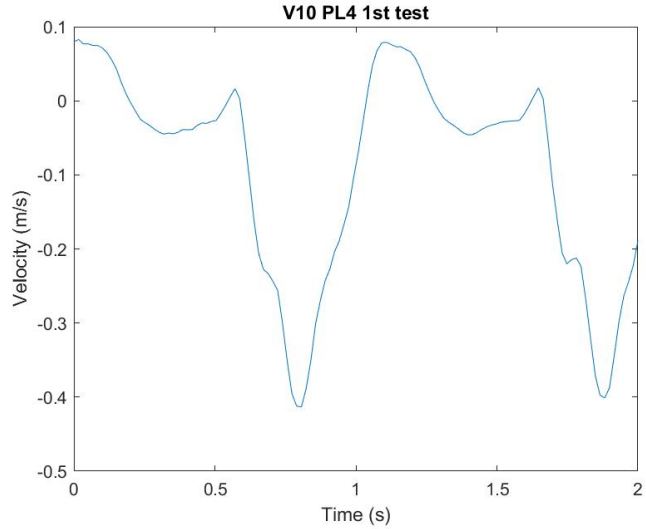

(a) V=10V PL=4 SDC 1st test

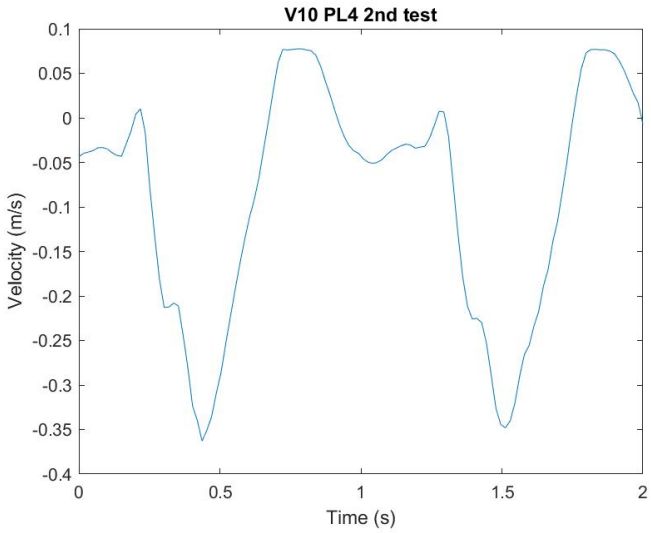

(b) V=10V PL=4 SDC 2nd test

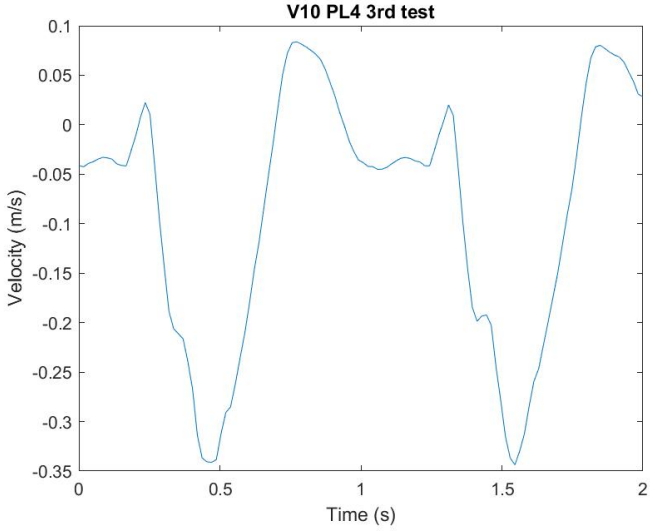

(c) V=10V PL=4 SDC 3rd test

Descriptio 4.25: SDC results for V=10V and PL=4.

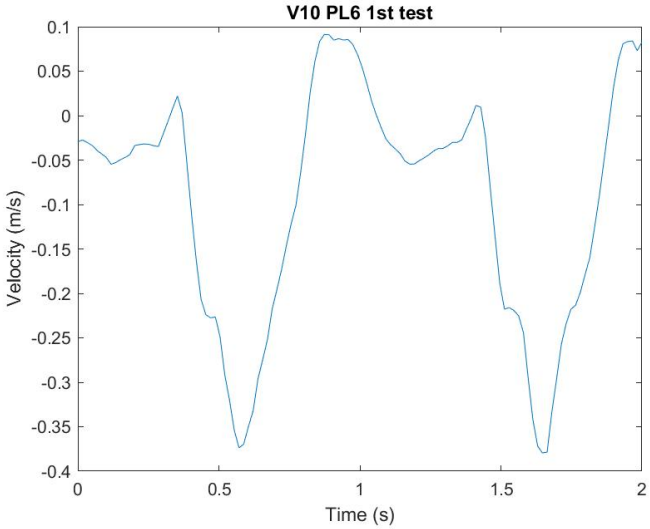

(a) V=10V PL=6 SDC 1st test

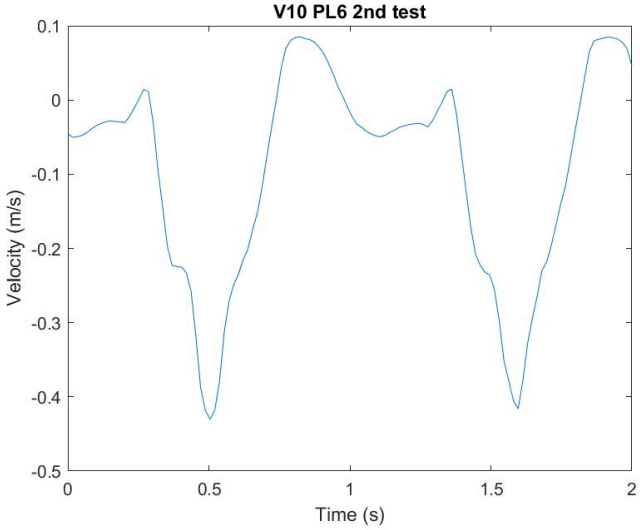

(b) V=10V PL=6 SDC 2nd test

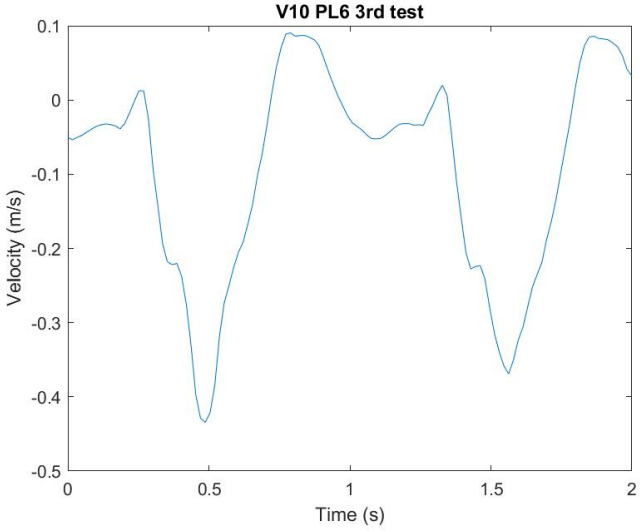

(c) V=10V PL=6 SDC 3rd test

Descriptio 4.26: SDC results for V=10V and PL=6.

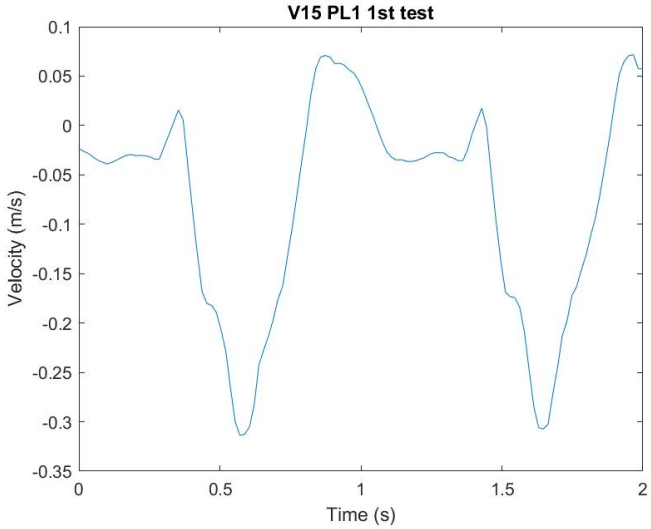

(a) V=15V PL=1 SDC 1st test

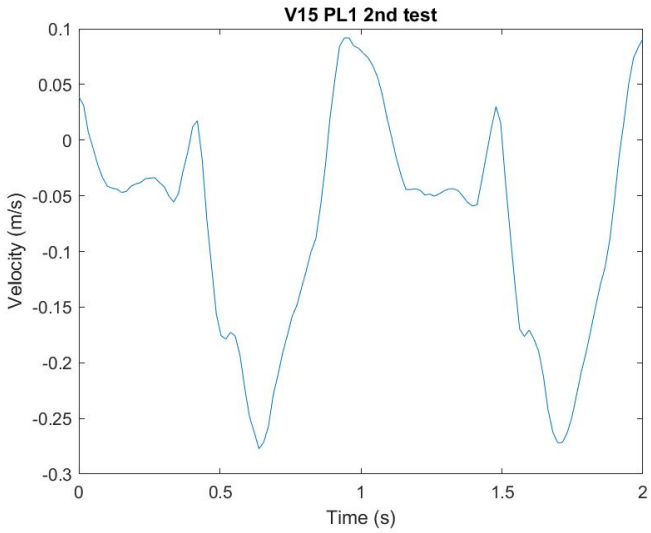

(b) V=15V PL=1 SDC 2nd test

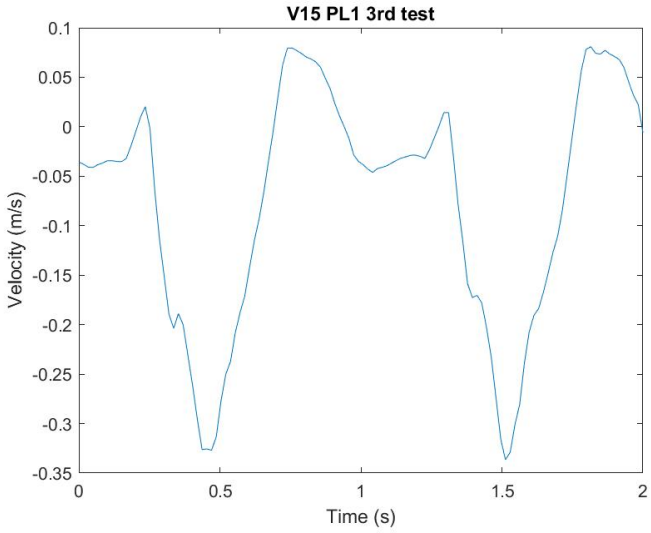

(c) V=15V PL=1 SVD 3rd test

Descriptio 4.27: SDC results for V=15V and PL=1.

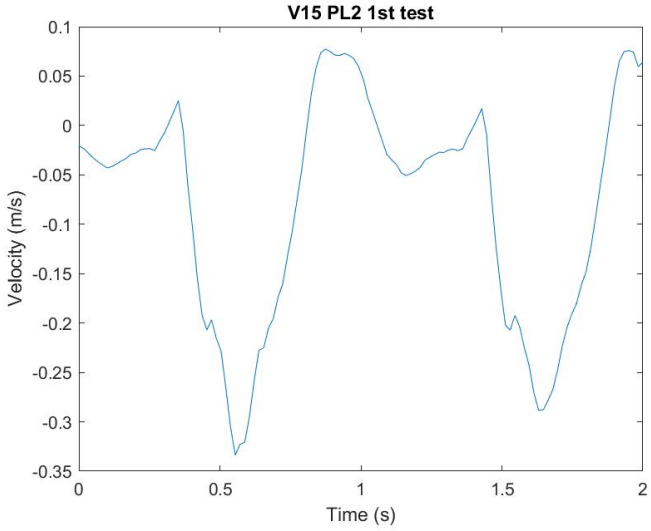

(a) V=15V PL=2 SDC 1st test

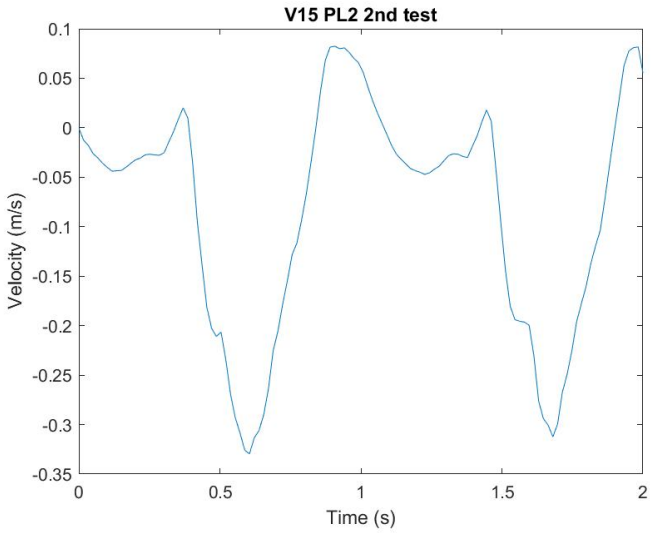

(b) V=15V PL=2 SDC 2nd test

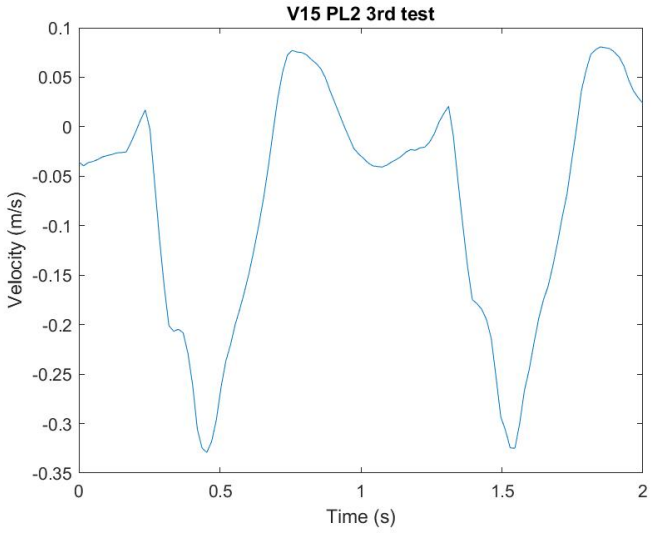

(c) V=15V PL=2 SDC 3rd test

Descriptio 4.28: SDC results for V=15V and PL=12.

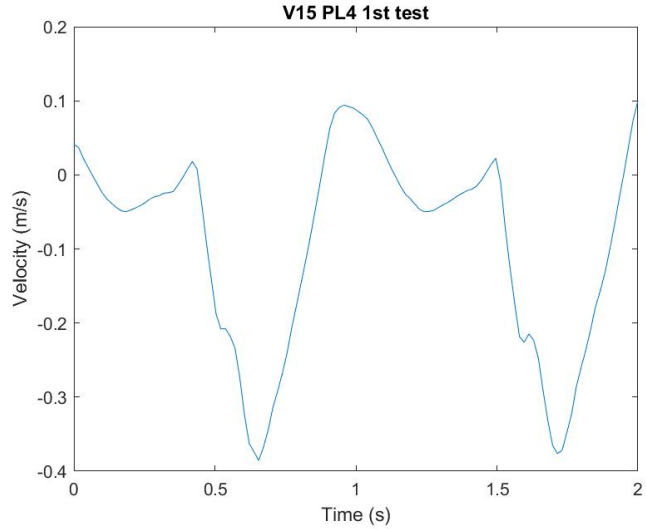

(a) V=15V PL=4 SDC 1st test

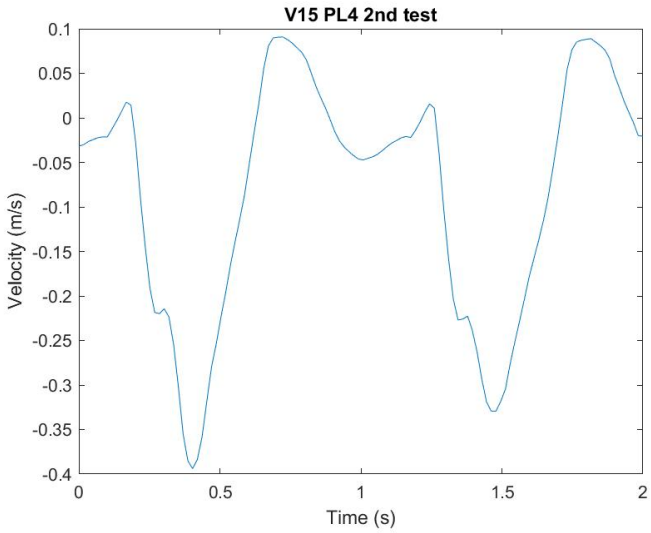

(b) V=15V PL=4 SDC 2nd test

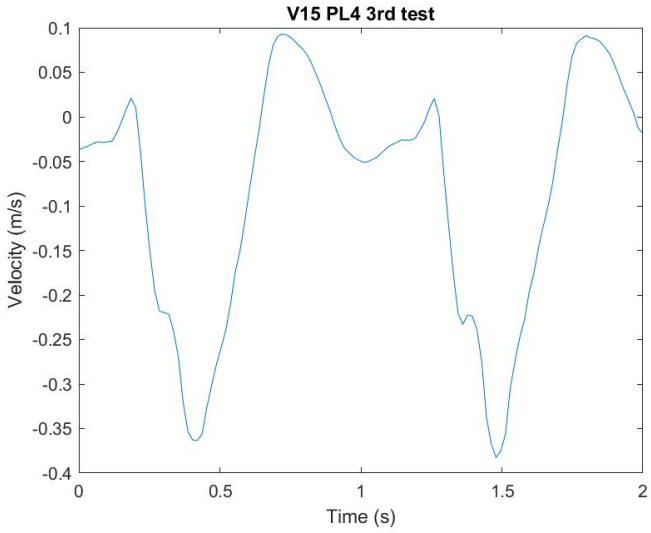

(c) V=15V PL=4 SDC 3rd test

Descriptio 4.29: SDC results for V=15V and PL=4.

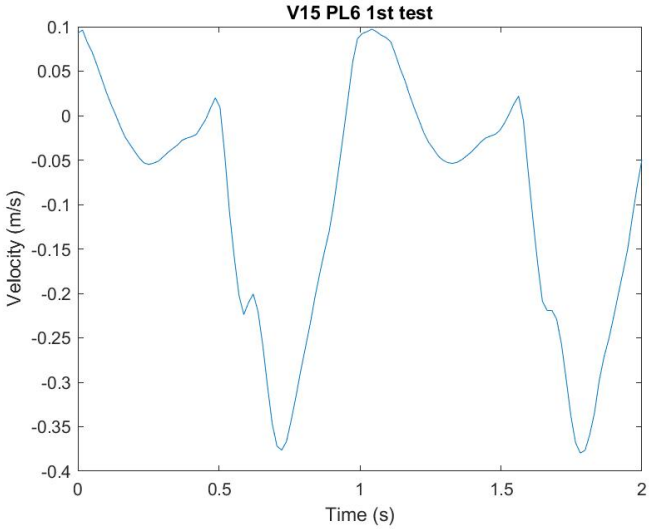

(a) V=15V PL=6 SDC 1st test

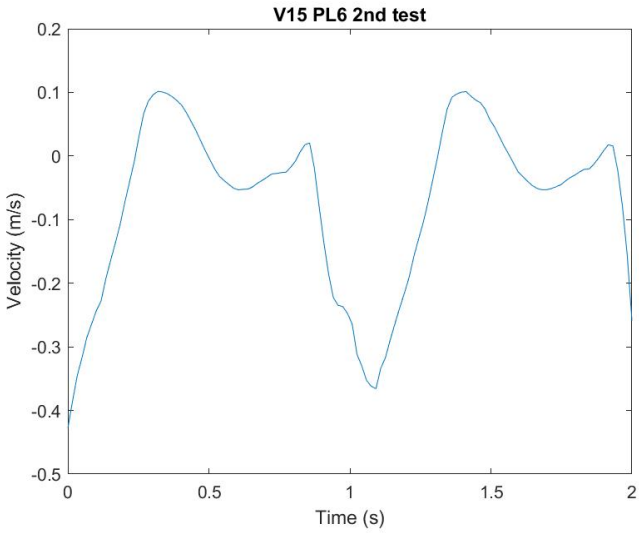

(b) V=15V PL=6 SDC 2nd test

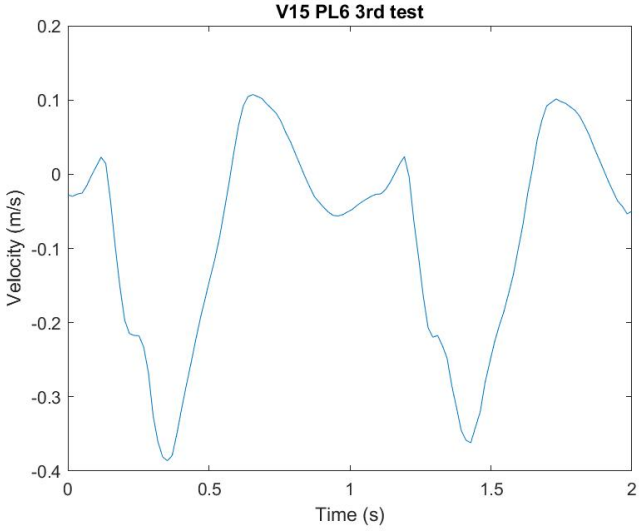

(c) V=15V PL=6 SDC 3rd test

Descriptio 4.30: SDC results for V=15V and PL=6.

4.4.3 Statistics

From the velocity profile obtained by applying the speckle decorrelation to the filtered data it is possible to measure the mean of velocity for each trial. Since for each couple of parameters the acquisitions were performed three times, the mean values and the standard deviations of the mean velocity obtained through the speckle decorrelation can be estimated. These results are then compared to the ground-truth in order to estimate the average error. The ground-truth has been estimated by measuring the volume flow of the BMF throughout the speckle phantom. After the estimation of the volume flow, the mean of velocity was calculated by dividing the volume flow by the section of the vessel. In this project the flow phantom was constant in section and its inner diameter was of 5 mm, so the mean volume can be obtained, as follows:

$$v_r = \frac{V}{A} = \frac{V}{\pi d^2/4} = 0.0701 ms^{-1} \tag{4.2}$$

where v_r is velocity mean, V is the volume flow and A is the area. The measured volume flow was 1.7365 mLs^{-1}. Therefore, the velocity mean of BMF was 0.0701 ms^{-1}.

Once applied the SDC and measured the out-of-plane mean velocity for each couple of parameters and each trial, the averaged error is obtained, as follows:

$$\varepsilon_{i,j} = \frac{|v_r - v_{i,j}|}{v_r} \tag{4.3}$$

Where $\varepsilon_{i,j}$ is the averaged error for each combination of the different values of voltage and pulse lengths, $v_{i,j}$ is the out-of-plane mean velocity for each combination of the different values of voltage and pulse lengths and v_r is the ground-truth.

The table 4.1 provides all the results achieved by applying the SDC to the filtered datasets. The errors for each evaluation have been calculated, as well.

Tabula 4.1: Estimated out-of-plane velocities components and errors for each couple of parameters and each trials.

	1^{st} v $[ms^{-1}]$	1^{st} ε (%)	2^{nd} v $[ms^{-1}]$	2^{nd} ε (%)	3^{rd} v $[ms^{-1}]$	3^{rd} ε (%)
V = 5V PL = 1	0.0690	1.630	0.0700	0.204	0.0673	4.054
V = 5V PL = 2	0.0684	2.458	0.0672	4.196	0.0678	3.341
V = 5V PL = 4	0.0793	13.054	0.0992	41.424	0.0816	16.333
V = 5V PL = 6	0.0901	28.451	0.0797	13.624	0.0817	16.475
V = 10V PL = 1	0.0692	1.345	0.0672	4.196	0.0673	4.054
V = 10V PL = 2	0.0668	4.767	0.0667	4.909	0.0664	5.337
V = 10V PL = 4	0.0787	12.198	0.0781	11.343	0.0739	5.355
V = 10V PL = 6	0.0771	9.917	0.0791	12.769	0.0817	16.475
V = 15V PL = 1	0.0649	7.475	0.0654	6.762	0.0684	2.486
V = 15V PL = 2	0.0664	5.337	0.0699	0.0347	0.0687	2.058
V = 15V PL = 4	0.0807	15.050	0.0803	14.479	0.0789	12.484
V = 15V PL = 6	0.0794	13.196	0.0803	14.479	0.0849	21.035

The table 4.2 provides the means and standard deviations of all the results shown in table 4.1

Tabula 4.2: Means and standard deviations of the out-of-plane velocities components and errors.

	v_{mean} $[ms^{-1}]$	v_{std} $[ms^{-1}]$	ε_{mean} (%)	ε_{std} (%)
V = 5V PL = 1	0.0688	0.000978	1.963	01.946
V = 5V PL = 2	0.0678	0.0004	3.341	0.855
V = 5V PL = 4	0.0867	0.00833	23.604	15.520
V = 5V PL = 6	0.0838	0.00420	19.520	7.867
V = 10V PL = 1	0.0679	0.002	3.199	1.607
V = 10V PL = 2	0.0667	0.0011	5.004	0.297
V = 10V PL = 4	0.0769	0.002	9.632	3.728
V = 10V PL = 6	0.0793	0.016	13.054	3.288
V = 15V PL = 1	0.0662	0.0014	5.574	2.700
V = 15V PL = 2	0.0687	0.0015	2.580	2.534
V = 15V PL = 4	0.0800	0.0007	14.004	1.347
V = 15V PL = 6	0.0815	0.0022	16.238	4.206

The results provided in table 4.2 are displayed in figures 4.31 and 4.32, in order to have a better view of the measured velocities with respect to the ground-truth and of the percentage errors. As one can notice by looking at figure 4.31, the values of the estimated velocity are strictly dependent on the values of pulse length. In particular, it has been demonstrated that for low values of pulse length, i.e. PL=1 and PL=2, the measured velocities are underestimated with respect to the ground-truth. On the other side, for high values of pulse length, i.e. PL=4 and PL=6, the measured velocities are overestimated with respect to the ground-truth. The impact of different values of pulse length in SDC will reflect also on the estimation of percentage errors. As one can clearly see in figure 4.32, lower values of PL coincide with lower values of averaged error. Vice versa, the higher values of PL coincide with higher values of averaged error. In other words, the speckle decorrelation method performs better in presence of low pulse lengths. The reason why this trend occurs is still unclear. A possible explanation to these results could be that in some way a higher pulse length worsens the autocorrelation of the tissue signal. Nevertheless, it remains an open question, therefore further research will be conducted to find a proper answer. In addition to this, the 2^{nd} trials of the dataset acquired with V=5V and PL=4 represents an outlier, so the results achieved for this couple of parameters are not representative of the real results.

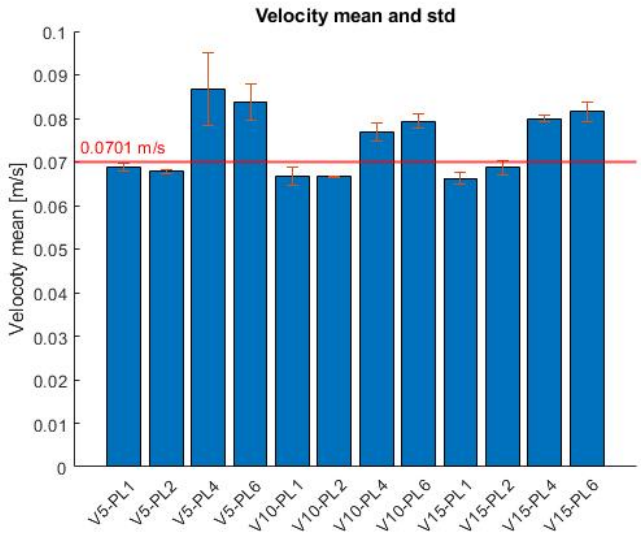

Descriptio 4.31: Mean and std of the estimated velocities with respect to the ground-truth.

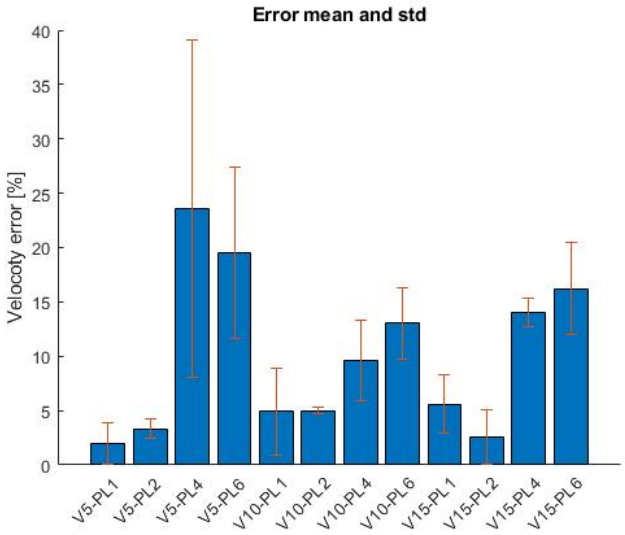

Descriptio 4.32: Mean and std of the errors committed in the estimation of the out-of-plane velocities.

Caput 5

Conclusions and Future Prospects

The *speckle decorrelation method* represents an innovative method, capable to estimate the out-of-plane velocity components of the volume flow from the cross-sectional point of view. Previous researches have demonstrated the worth of the SDC method by estimating the blood volume flow both in vivo and in vitro experiments. Nevertheless, these studies required the employment of micro-bubble contrast agents to enhance blood signal. In this master thesis project, the feasibility of applying the SDC method in absence of micro-bubble contrast agents has been tested in vitro. Therefore, the *singular value decomposition filtering* has been used to enhance the signal of blood. The combination of SVD filtering and SDC method has led to compelling results in terms of the estimation of the out-of-plane component of the velocity. In particular, it has been proved that the estimated mean velocity matches well with the ground-truth for low values of pulse length. These outcomes suggest a new possible way to correctly detect the blood volume flow and could give important contribution in next future clinical applications.

Nowadays, the proposed method represents the only effective solution for 3-D volume flow imaging. In addition to this, the application of the SVD filtering allows to avoid the presence of micro-bubble contrast agents, which is a feature to prefer, especially in vivo experiments. On the other side, the use of singular value decomposition filtering involves the suppression of the tissue echoes and of the noise in relation to the established double threshold. Since there is no existing current method to find the optimal thresholds, the filtered images could be partially warped. Despite this problem, the SVD has proved to be a valid method to filter the acquired data. The use of SDC method has led to interesting results in terms of estimation of the out-of-plane velocity. Nevertheless only in vitro experiments have been conducted during this master thesis project. To further analyse the validity of the proposed approach, additional in vivo experiments need to be kept. Furthermore, it is important to high-line that the in vivo experiments have been handled in non-optimal conditions, since all the data were acquired in few hours and the speckle phantom created did not generate a good echo and presented a leakage. Although these complications, the SDC has proved to be a good and strong method capable to correctly detect the out-of-plane velocity through the scanning plane.

In order to have a better statistical relevance, more acquisitions need to be done. In this project only three acquisition for each couple of parameters were performed. The reason why not further acquisitions were performed lies in the huge amount of data and

in the storage limits. Each dataset, in fact, needs more than 7 G-Byte to be saved. The only solution to overcome this limit is to use a more capacious hard-disk.

Finally, it has been proved that *speckle decorrelation* performs well in presence of low values of pulse length, e.g. PL=1 and PL=2, while the results worsen when the values of pulse length increase, e.g. PL=2 and PL=4. A possible answer to this behaviour could be that the higher pulse length involves a reduction of the autocorrelation of tissue signal. Anyway, no current research has been conducted in this filed, thus this still remains an open question.

Despite all the complications rediscovered during this master thesis project and the limitations of the *speckle decorrelation method*, the proposed approach results to be promising in terms of evaluating the 3-D volume flow in future clinical application. For this reason, additional researches will be carried both to demonstrate its feasibility in vivo and to have a more statistical relevance.

Conspectus librorum

[1] Larry B Goldstein. Potential effects of common drugs on stroke recovery. *Archives of Neurology*, 55(4):454–456, 1998.

[2] Justin C Choi, Faisal G Bakaeen, Lorraine D Cornwell, Tam K Dao, Joseph S Coselli, Scott A LeMaire, and Danny Chu. Morbid obesity is associated with increased resource utilization in coronary artery bypass grafting. *The Annals of thoracic surgery*, 94(1):23–28, 2012.

[3] SE Wolowacz, M Samuel, VK Brennan, J-G Jasso-Mosqueda, and IC Van Gelder. The cost of illness of atrial fibrillation: a systematic review of the recent literature. *Europace*, 13(10):1375–1385, 2011.

[4] Véronique L Roger, Alan S Go, Donald M Lloyd-Jones, Robert J Adams, Jarett D Berry, Todd M Brown, Mercedes R Carnethon, Shifan Dai, Giovanni De Simone, Earl S Ford, et al. Heart disease and stroke statistics—2011 update: a report from the american heart association. *Circulation*, 123(4):e18–e209, 2011.

[5] IA Hein and William D O'Brien. Current time-domain methods for assessing tissue motion by analysis from reflected ultrasound echoes-a review. *IEEE transactions on ultrasonics, ferroelectrics, and frequency control*, 40(2):84–102, 1993.

[6] Peter D Gatehouse, Jennifer Keegan, Lindsey A Crowe, Sharmeen Masood, Raad H Mohiaddin, Karl-Friedrich Kreitner, and David N Firmin. Applications of phase-contrast flow and velocity imaging in cardiovascular mri. *European radiology*, 15(10):2172–2184, 2005.

[7] Robert W Gill. Measurement of blood flow by ultrasound: accuracy and sources of error. *Ultrasound in Medicine and Biology*, 11(4):625–641, 1985.

[8] Peter R Hoskins, Kevin Martin, and Abigail Thrush. *Diagnostic ultrasound: physics and equipment*. Cambridge University Press, 2010.

[9] M Voiculescu, A Pop, and I Romoşan. Conventional spectral doppler and color doppler ultrasound imaging. principles, limitations, artifacts and clinical indications in hepatology. *Romanian journal of internal medicine= Revue roumaine de medecine interne*, 30(3):139–155, 1992.

[10] Jørgen Arendt Jensen and Peter Munk. A new method for estimation of velocity vectors. *IEEE transactions on ultrasonics, ferroelectrics, and frequency control*, 45(3):837–851, 1998.

[11] Billy YS Yiu and Alfred CH Yu. Least-squares multi-angle doppler estimators for plane-wave vector flow imaging. *IEEE Trans. Ultrason., Ferroelectr., Freq. Control*, 63(11):1733–1744, 2016.

[12] Chee Hau Leow, Eleni Bazigou, Robert J Eckersley, CH Alfred, Peter D Weinberg, and Meng-Xing Tang. Flow velocity mapping using contrast enhanced high-frame-rate plane wave ultrasound and image tracking: Methods and initial in vitro and in vivo evaluation. *Ultrasound in medicine & biology*, 41(11):2913–2925, 2015.

[13] D Ww Rickey, PA Picot, DA Christopher, and A Fenster. A wall-less vessel phantom for doppler ultrasound studies. *Ultrasound in Medicine and Biology*, 21(9):1163–1176, 1995.

[14] X. Zhou, C. H. Leow, E. Rowland, K. Riemer, J. M. Rubin, P. D. Weinberg, and M. Tang. 3-d velocity and volume flow measurement *in vivo* using speckle decorrelation and 2-d high-frame-rate contrast-enhanced ultrasound. *IEEE Transactions on Ultrasonics, Ferroelectrics, and Frequency Control*, 65(12):2233–2244, 2018.

[15] Simon Holbek, Matthias Bo Stuart, et al. Volumetric 3-d vector flow measurements using a 62+ 62 row-column addressed array. In *2017 IEEE International Ultrasonics Symposium (IUS)*, pages 1–4. IEEE, 2017.

[16] Jørgen Arendt Jensen, Svetoslav Ivanov Nikolov, Alfred CH Yu, and Damien Garcia. Ultrasound vector flow imaging—part ii: Parallel systems. *IEEE Trans. Ultrason., Ferroelectr., Freq. Control*, 63(11):1722–1732, 2016.

[17] Jonathan M Rubin, Theresa A Tuthill, and J Brian Fowlkes. Volume flow measurement using doppler and grey-scale decorrelation. *Ultrasound in medicine & biology*, 27(1):101–109, 2001.

[18] Dae Woo Park, Grant H Kruger, Jonathan M Rubin, James Hamilton, Paul Gottschalk, Robert E Dodde, Albert J Shih, and William F Weitzel. Quantification of ultrasound correlation-based flow velocity mapping and edge velocity gradient measurement. *Journal of Ultrasound in Medicine*, 32(10):1815–1830, 2013.

[19] Xinhuan Zhou, Virginie Papadopoulou, Chee Hau Leow, Peter Vincent, and Meng-Xing Tang. 3-d flow reconstruction using divergence-free interpolation of multiple 2-d contrast-enhanced ultrasound particle imaging velocimetry measurements. *Ultrasound in medicine & biology*, 45(3):795–810, 2019.

[20] Theresa A Tuthill, Jonathan M Rubin, and J Brian Fowlkes. Three-dimensional flow vectors from rf ultrasound signals. In *Medical Imaging 2002: Ultrasonic Imaging and Signal Processing*, volume 4687, pages 210–217. International Society for Optics and Photonics, 2002.

[21] R James Housden, Andrew H Gee, Graham M Treece, and Richard W Prager. Sensorless reconstruction of unconstrained freehand 3d ultrasound data. *Ultrasound in medicine & biology*, 33(3):408–419, 2007.

[22] Jørgen Arendt Jensen. *Estimation of blood velocities using ultrasound: a signal processing approach*. Cambridge University Press, 1996.

[23] GR Lockwood, LK Ryan, JW Hunt, and FS Foster. Measurement of the ultrasonic properties of vascular tissues and blood from 35–65 mhz. *Ultrasound in medicine & biology*, 17(7):653–666, 1991.

[24] Christian R Falyar. Sound principles.

[25] Liang Zhai, John Madden, Wen-Chi Foo, Vladimir Mouraviev, Thomas Polascik, Mark Palmeri, and Kathryn Nightingale. Characterizing stiffness of human prostates using acoustic radiation force. *Ultrasonic imaging*, 32:201–13, 10 2010.

[26] David P Hruska, Jose Sanchez, and Michael L Oelze. Improved diagnostics through quantitative ultrasound imaging. In *2009 Annual International Conference of the IEEE Engineering in Medicine and Biology Society*, pages 1956–1959. IEEE, 2009.

[27] Martin E Anderson and Gregg E Trahey. A seminar on k-space applied to medical ultrasound. *Department of Biomedical Engineering, Duke University*, 2000.

[28] Johannes F De Boer, Barry Cense, B Hyle Park, Mark C Pierce, Guillermo J Tearney, and Brett E Bouma. Improved signal-to-noise ratio in spectral-domain compared with time-domain optical coherence tomography. *Optics letters*, 28(21):2067–2069, 2003.

[29] F García, E Moreno, J Solano, M Barragán, A Sotomayor, and M Fuentes. Bidirectional doppler system for blood flow measurement based on an open architecture. *Revista Mexicana de Ingeniería Biomédica*, 24(2):135–143, 2003.

[30] K Kirk Shung. Diagnostic ultrasound. 2006.

[31] Conti Fiorenzo, PIERO PAOLO BATTAGLINI, N Belluardo, B Fabrizio, B Fabio, B Roberto, C Roberto, C Carlo, C Giovanni, C Enrico, et al. Fisiologia medica. 2005.

[32] Antonio Amoroso and Filippo Rossi Fanelli. *Semeiotica medica e Metodologia clinica (2^a edizione)*. Antonio Delfino Editore, 2017.

[33] R Davis Manning and Arthur C Guyton. Control of blood volume. In *Reviews of Physiology, Biochemistry and Pharmacology, Volume 93*, pages 69–114. Springer, 1982.

[34] Xiaowei Zhou, David A Kenwright, Shiying Wang, John A Hossack, and Peter R Hoskins. Fabrication of two flow phantoms for doppler ultrasound imaging. *IEEE transactions on ultrasonics, ferroelectrics, and frequency control*, 64(1):53–65, 2016.

[35] Kumar V Ramnarine, Dariush K Nassiri, Peter R Hoskins, and Jaap Lubbers. Validation of a new blood-mimicking fluid for use in doppler flow test objects. *Ultrasound in medicine & biology*, 24(3):451–459, 1998.

[36] Chung Kit Ho, Adrian JY Chee, Billy YS Yiu, Anderson CO Tsang, Kwok Wing Chow, and CH Alfred. Wall-less flow phantoms with tortuous vascular geometries: Design principles and a patient-specific model fabrication example. *IEEE transactions on ultrasonics, ferroelectrics, and frequency control*, 64(1):25–38, 2016.

[37] AC Lamont, HS Hall, JR Thompson, and DH Evans. Doppler ultrasound studies in renal arteries of normal newborn babies. *The British journal of radiology*, 64(761):413–416, 1991.

[38] Donald W Baker and William G Yates. Technique for studying the sample volume of ultrasonic doppler devices. *Medical and biological engineering*, 11(6):766–770, 1973.

[39] Chihiro Kasai, Koroku Namekawa, Akira Koyano, and Ryozo Omoto. Real-time two-dimensional blood flow imaging using an autocorrelation technique. *IEEE Transactions on sonics and ultrasonics*, 32(3):458–464, 1985.

[40] Robert F Wagner. Statistics of speckle in ultrasound b-scans. *IEEE Trans. Sonics & Ultrason.*, 30(3):156–163, 1983.

[41] Joo Ha Hwang, Andrew A Brayman, Michael A Reidy, Thomas J Matula, Michael B Kimmey, and Lawrence A Crum. Vascular effects induced by combined 1-mhz ultrasound and microbubble contrast agent treatments in vivo. *Ultrasound in medicine & biology*, 31(4):553–564, 2005.

[42] Charlie Demené, Thomas Deffieux, Mathieu Pernot, Bruno-Félix Osmanski, Valérie Biran, Jean-Luc Gennisson, Lim-Anna Sieu, Antoine Bergel, Stephanie Franqui, Jean-Michel Correas, et al. Spatiotemporal clutter filtering of ultrafast ultrasound data highly increases doppler and fultrasound sensitivity. *IEEE transactions on medical imaging*, 34(11):2271–2285, 2015.

[43] JC Willemetz, A Nowicki, JJ Meister, F De Palma, and G Pante. Bias and variance in the estimate of the doppler frequency induced by a wall motion filter. *Ultrasonic Imaging*, 11(3):215–225, 1989.

[44] Colin Tysoe and David H Evans. Bias in mean frequency estimation of doppler signals due to wall clutter filters. *Ultrasound in medicine & biology*, 21(5):671–677, 1995.

[45] Léon AF Ledoux, Peter J Brands, and Arnold PG Hoeks. Reduction of the clutter component in doppler ultrasound signals based on singular value decomposition: A simulation study. *Ultrasonic imaging*, 19(1):1–18, 1997.

[46] CH Alfred and Lasse Lovstakken. Eigen-based clutter filter design for ultrasound color flow imaging: A review. *IEEE transactions on ultrasonics, ferroelectrics, and frequency control*, 57(5):1096–1111, 2010.

[47] Dustin E Kruse and Katherine W Ferrara. A new high resolution color flow system using an eigendecomposition-based adaptive filter for clutter rejection. *IEEE transactions on ultrasonics, ferroelectrics, and frequency control*, 49(10):1384–1399, 2002.

[48] Mickael Tanter and Mathias Fink. Ultrafast imaging in biomedical ultrasound. *IEEE transactions on ultrasonics, ferroelectrics, and frequency control*, 61(1):102–119, 2014.

[49] Mickaël Tanter, Jeremy Bercoff, Laurent Sandrin, and Mathias Fink. Ultrafast compound imaging for 2-d motion vector estimation: Application to transient elastography. *IEEE transactions on ultrasonics, ferroelectrics, and frequency control*, 49(10):1363–1374, 2002.

[50] Jeremy Bercoff, Gabriel Montaldo, Thanasis Loupas, David Savery, Fabien Mézière, Mathias Fink, and Mickael Tanter. Ultrafast compound doppler imaging: Providing full blood flow characterization. *IEEE transactions on ultrasonics, ferroelectrics, and frequency control*, 58(1):134–147, 2011.

[51] E Ignacio Céspedes, Chris L de Korte, and Antonius FW van der Steen. Echo decorrelation from displacement gradients in elasticity and velocity estimation. *IEEE transactions on ultrasonics, ferroelectrics, and frequency control*, 46(4):791–801, 1999.

[52] Jian-Feng Chen, J Brian Fowlkes, Paul L Carson, and Jonathan M Rubin. Determination of scan-plane motion using speckle decorrelation: Theoretical considerations and initial test. *International Journal of Imaging Systems and Technology*, 8(1):38–44, 1997.

[53] Richard W Prager, Andrew H Gee, Graham M Treece, Charlotte JC Cash, and Laurence H Berman. Sensorless freehand 3-d ultrasound using regression of the echo intensity. *Ultrasound in medicine & biology*, 29(3):437–446, 2003.

[54] Jonathan M Rubin, J Brian Fowlkes, Theresa A Tuthill, Aaron P Moskalik, Richard T Rhee, Ronald S Adler, Sahira N Kazanjian, and Paul L Carson. Speckle decorrelation flow measurement with b-mode us of contrast agent flow in a phantom and in rabbit kidney. *Radiology*, 213(2):429–437, 1999.

[55] Robert F Wagner, Michael F Insana, and David G Brown. Statistical properties of radio-frequency and envelope-detected signals with applications to medical ultrasound. *JOSA A*, 4(5):910–922, 1987.

[56] Theresa A Tuthill, JF Krücker, J Brian Fowlkes, and Paul L Carson. Automated three-dimensional us frame positioning computed from elevational speckle decorrelation. *Radiology*, 209(2):575–582, 1998.

[57] Xiaowei Zhou, Chee Hau Leow, Ethan Rowland, Kai Riemer, Jonathan M Rubin, Peter D Weinberg, and Meng-Xing Tang. 3-d velocity and volume flow measurement *invivo* using speckle decorrelation and 2-d high-frame-rate contrast-enhanced ultrasound. *IEEE transactions on ultrasonics, ferroelectrics, and frequency control*, 65(12):2233–2244, 2018.

[58] Gabriel Montaldo, Mickaël Tanter, Jérémy Bercoff, Nicolas Benech, and Mathias Fink. Coherent plane-wave compounding for very high frame rate ultrasonography and transient elastography. *IEEE transactions on ultrasonics, ferroelectrics, and frequency control*, 56(3):489–506, 2009.

[59] Damon C Sutton, Roman Kluger, Shihab U Ahmed, Sharon C Reimold, and Jonathan B Mark. Flow reversal in the descending aorta: a guide to intraoperative assessment of aortic regurgitation with transesophageal echocardiography. *The Journal of thoracic and cardiovascular surgery*, 108(3):576–582, 1994.

[60] Frederich Bukachi, Anders Waldenström, Stellan Mörner, Per Lindqvist, MY Henein, and Elsadig Kazzam. Pulmonary venous flow reversal and its relationship to atrial mechanical function in normal subjects–umeå general population heart study. *European Journal of Echocardiography*, 6(2):107–116, 2005.

[61] Xiaowei Zhou, Xinhuan Zhou, Chee Hau Leow, and Meng-Xing Tang. Measurement of flow volume in the presence of reverse flow with ultrasound speckle decorrelation. *Ultrasound in medicine & biology*, 45(11):3056–3066, 2019.